Distribution Agreement

In presenting this thesis or dissertation as a partial fulfillment of the requirements for an advanced degree from Emory University, I hereby grant to Emory University and its agents the non-exclusive license to archive, make accessible, and display my thesis or dissertation in whole or in part in all forms of media, now or hereafter known, including display on the world wide web. I understand that I may select some access restrictions as part of the online submission of this thesis or dissertation. I retain all ownership rights to the copyright of the thesis or dissertation. I also retain the right to use in future works (such as articles or books) all or part of this thesis or dissertation.

Signature:

James Ross _____ _____

Date

PDGFB is a Potent Inflammatory Driver in Pediatric High-Grade Glioma

By

James L. Ross
Doctor of Philosophy

Cancer Biology

_____ [Advisor's signature]
Dolores Hambardzumyan, Ph.D., M.B.A.
Advisor

_____ [Member's signature]
Cheng-Kui Qu, M.D., Ph.D.
Committee Member

_____ [Member's signature]
Tobey MacDonald, M.D.
Committee Member

_____ [Member's signature]
Gregory Lesinski, Ph.D., M.P.H.
Committee Member

_____ [Member's signature]
Renee Read, Ph.D.
Committee Member

Accepted:

_____
Lisa A. Tedesco, Ph.D.
Dean of the James T. Laney School of Graduate Studies

_____
Date

PDGFB is a Potent Inflammatory Driver in Pediatric High-Grade Glioma

By

James L. Ross
B.S., Berry College, 2015

Advisor: Dolores Hambardzumyan, Ph.D., M.B.A.

An abstract of
A dissertation submitted to the Faculty of the
James T. Laney School of Graduate Studies of Emory University
in partial fulfillment of the requirements for the degree of
Doctor of Philosophy
in Cancer Biology
2019

Abstract

PDGFB is a Potent Inflammatory Driver in Pediatric High-Grade Glioma

By James L. Ross

Pediatric high-grade gliomas (pHGG) account for the most cancer-related deaths in children. Despite aggressive therapeutic strategies, tumor recurrence is inevitable and the median survival is just 12-15 months. One promising avenue of research is the development of novel therapies targeting the properties of non-neoplastic cell-types within the tumor such as tumor associated macrophages (TAMs). Much is known about TAMs in adult high-grade gliomas (aHGG), however very little is known about them in the pediatric setting. TAMs can make up 30-40% of the total tumor cell mass in aHGG, promoting tumor growth and immune evasion. This raises the question of whether pHGGs possess a distinct constituency of TAMs due to their unique genetic and epigenetic landscapes. To uncover the composition and behavior of TAMs in pHGG we utilize RCAS/tva, a somatic cell-type specific gene transfer system which allows us to recapitulate all major subtypes of pHGG in newborn immunocompetent mice, including histone wild-type and histone-mutant tumors. These tumors are induced in *Nestin*-positive cells by overexpression of PDGFA or PDGFB along with other driver mutations, each in their respective locations found in the human population. Tumors driven by PDGFB have a significantly lower median survival compared to PDGFA-driven tumors and have increased infiltration of lymphocytes and TAMs, specifically inflammatory monocytes. NanoString analysis indicates PDGFB-driven tumors have a highly inflammatory microenvironment, and this data is supported by a large qPCR panel for immune markers and chemokines. *In vitro* bone marrow derived monocyte and microglial cultures demonstrate the BMDM population is most responsible for the production of inflammatory chemokines and angiogenic factors in the tumor microenvironment. Using human pHGG tissue samples, we demonstrate PDGFB and PDGFRβ strongly correlate with TAM infiltration. We also show pHGGs are relatively barren for $CD3^+$ and $CD8^+$ T-cells. Further, using NanoString we show brainstem pHGGs are more inflammatory compared to hemispheric pHGGs. Lastly, through chemokine knockout mice, we demonstrate the feasibility of reducing TAM infiltration and prolonging survival in both PDGFA and PDGFB-driven tumors. Together, these studies provide strong evidence for the potent inflammatory effects PDGFB has in pHGGs and lays the foundation needed for the development of novel therapeutics targeting these tumors.

PDGFB is a Potent Inflammatory Driver in Pediatric High-Grade Glioma

By

James L. Ross
B.S., Berry College, 2015

Advisor: Dolores Hambardzumyan, Ph.D., M.B.A.

A dissertation submitted to the Faculty of the
James T. Laney School of Graduate Studies of Emory University
in partial fulfillment of the requirements for the degree of
Doctor of Philosophy
in Cancer Biology
2019

Acknowledgements

I would like to extend my gratitude to the following individuals and organizations for their support and assistance throughout my training.

My wife Megan and our son Isaac whom I love and appreciate dearly

Dolores Hambardzumyan, Ph.D., M.B.A.

Zhihong Chen, Ph.D.

Cameron Herting, B.S.

Daniel Brat, M.D., Ph.D.

Tobey MacDonald, M.D.

Cheng-Kui Qu, M.D., Ph.D.

Gregory Lesinski, Ph.D., M.P.H.

Renee Read, Ph.D.

Oren Becher, M.D.

Matthew Schniederjan, M.D.

Frank Szulzewsky, Ph.D.

Sabina Islam, M.D.

Dave Schumick

National Institutes of Health grants 1F31CA232531, R21NS106554 and R01NS100864

Emory University Cancer Biology Graduate Program

Emory University Graduate Division of Biological and Biomedical Sciences

Emory University Laney Graduate School

Emory University Core Facilities

Emory University Department of Pediatrics

Emory University Winship Cancer Institute

Table of Contents

Table of Contents

Table of Figures

Tables

Abbreviations

Chapter 1

Epidemiology

In the pediatric population, gliomas account for approximately 53% of all tumors found in the CNS (1). Two-thirds of pediatric gliomas are low-grade (WHO grades I and II) while the remaining are high-grade (WHO grades III and IV) tumors (2, 3). Tumors considered in the latter category include anaplastic astrocytoma, anaplastic oligodendroglioma, oligoastrocytoma, gliosarcoma, glioblastoma, and diffuse intrinsic pontine glioma (DIPG) (1). Although infrequent, pediatric high-grade gliomas (pHGG) are responsible for the most cancer related deaths in children and possess a dismal median survival of 12-15 months, even after aggressive therapeutic intervention (1, 4). There are few established causative factors underlying the development of these tumors. Ionizing radiation exposure and predisposing genetic syndromes including Neurofibromatosis Type 1, Turcot syndrome, and Li-Fraumeni syndrome have been implicated in the development of HGGs (5-7).

Genetic Alterations in pHGG

pHGGs most commonly present as primary tumors, arising either in the brainstem (~50%) or cortical hemispheres (~50%). These tumors share the same defining histologic features of adult high-grade gliomas (aHGG) including microvascular hyperplasia, brisk mitotic activity, pseudopalisading necrosis, and infiltrative tumor margins (8). pHGGs possess their own defining genetic aberrations and anatomical presentations that distinguish them from their adult counterparts. Both pHGG and aHGGs possess numerous molecular alterations including *PDGFRA* amplifications and mutations, however they are more frequent in pHGGs (up to 80%), constituting the most common genetic alteration in these tumors (9-12). Common in aHGGs are *EGFR* and *PTEN* alterations, which together characterize a major subtype of these tumors (13-15). However, alterations in *EGFR* and *PTEN* are infrequent in pHGG despite demonstrated

activation of the PI3-kinase pathway in these tumors (6, 12, 16). Approximately 86% of adult glioblastomas possess *TERT* promoter mutations, yet these mutations are only present in 2% of DIPGs and 3% of hemispheric pHGGs (17). Chromosomal alterations are also much more frequent in aHGGs compared to pHGGs (12, 18).

A strikingly exclusive feature of pHGGs is the presence of histone mutations which have been found to occur in approximately 50% of cases (10). 91% of DIPGs, 70% of midline HGGs, and 48% of hemispheric HGGs possess mutations in *H3F3A or HIST1H3B* (17, 19). These histone mutations have only recently been characterized and occur in specific anatomic locations within the brain. In 2012 Wu et al. discovered through whole genome sequencing that DIPG patients exclusively possessed heterozygous somatic mutations encoding K27M alterations in *H3F3A* and less frequently in *HIST1H3B*. They also found somatic mutations encoding G34R/V only in hemispheric pHGGs (17). Almost all G34R/V tumors also possess *ATRX-DAXX* mutations (20). Interestingly, in H3.1K27M tumors, activating mutations in *ACVR1* are frequently found and less commonly found in H3.3K27M tumors (17). Meta-analysis of over 1,000 pHGGs identified unique survival statistics for these three histone mutant subgroups. H3.1 and H3.3K27M mutations occur in younger patients and have the worst survival, while H3.3G34R mutations occur in slightly older patients and have an extended survival over K27M and histone-wild type tumors (10)(**Figure 1**). Despite possessing similar co-mutations with IDH1 mutant tumors, none of these histone mutant tumors have *IDH1* mutations (21). Even in cases where histopathology indicates the presence of a low-grade glioma (LGG), K27M mutant midline tumors are considered grade IV due to their aggressive nature and poor survival (22).

pHGGs also contain tumor suppressor gene alterations including *CDKN2A* deletion and *TP53* mutations. Homozygous deletions of *CDKN2A* are found in approximately 25% of

hemispheric pHGGs and are less commonly found in pHGGs arising in the midline and brainstem (23). Conversely, *TP53* mutations are more commonly found in DIPGs (40-50%) while only 35% of hemispheric pHGGs contain these mutations (6, 24, 25). These mutations are frequently found co-occurring in tumors with *PDGFRA* alterations, a phenomenon also observed in aHGG (13). Other mutations are also found in pHGGs but at very low frequencies, including RB pathway alterations and *BRAF-V600E* mutations (6, 23).

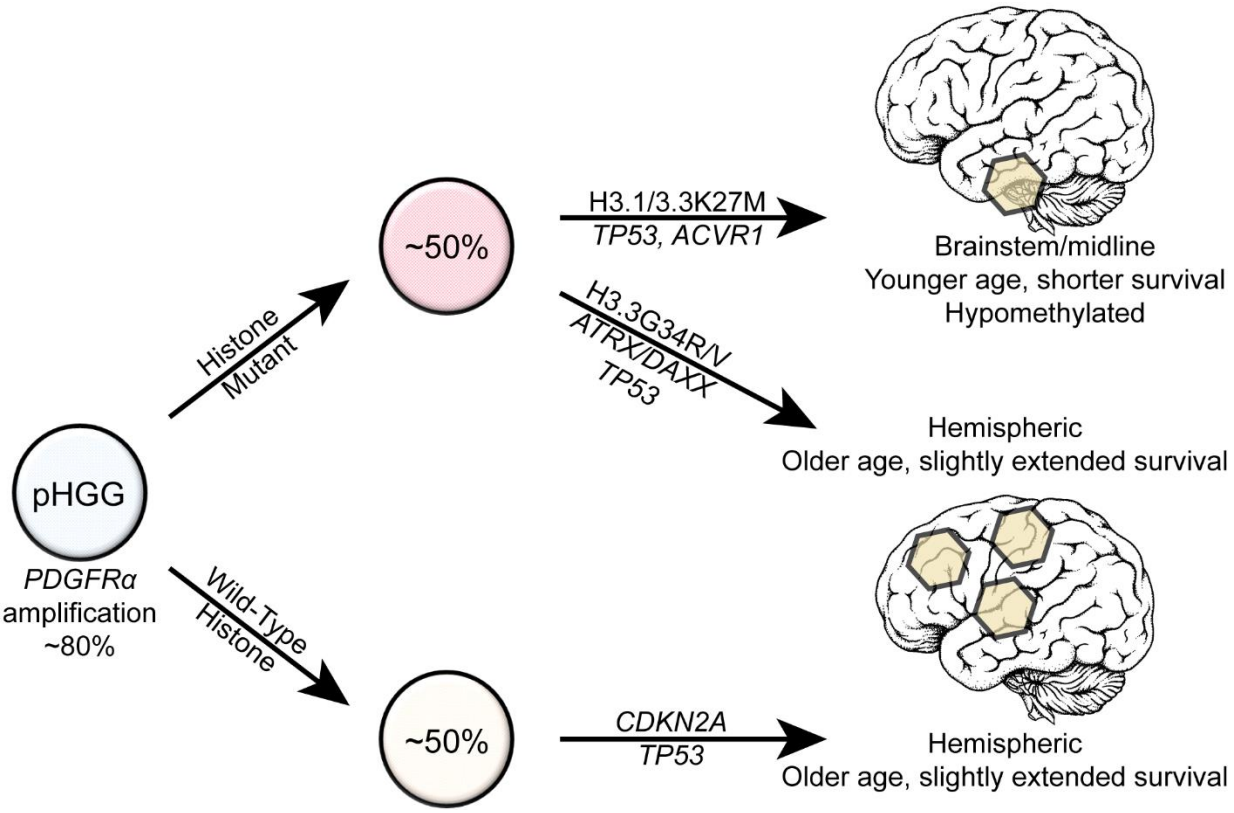

Figure 1: Molecular Profile of Human Pediatric High-Grade Gliomas. Schematic of the most common genetic alterations in pediatric high-grade gliomas.

Therapeutic Strategies

Unlike aHGGs such as GBM, pHGGs do not respond well to chemotherapy. Temozolomide, the only chemotherapy to prolong patient survival in adult GBM, does not demonstrate efficacy in the pediatric setting, likely due to the underlying biological differences between the two entities (26, 27). Due to the delicate nature of the developing brain, radiotherapy regimens are modified to reduce the amount of radiation induced necrosis, intracerebral swelling, and refractory illnesses in children (28). Radiation induced neurocognitive defects and endocrine disruption are common following radiotherapy in children, therefore strategies are designed to minimize these effects (6). Children three years of age or older typically receive 50-60 Gy of radiation dispersed throughout 1.8-2.0 Gy fractions (3, 6). In DIPG, radiotherapy remains the primary method of treatment as these tumors exist in surgically challenging regions of the brainstem. However, because of their location, a delicate balance exists between choosing radiotherapy dosing and frequency of administration. It is also difficult to adequately deliver drugs to these tumors, rendering them one of the most challenging tumors to treat in pediatric neuro-oncology (23, 29).

Since chemotherapy is ineffective and radiotherapy only provides transitory benefits, the most prognostically significant method of treatment for pHGGs is maximum surgical resection followed by focal radiotherapy (30). It has been reported that the five-year progression free survival (PFS) for children who undergo gross total resection doubles as a result (31). In cases where over 90% of the tumor is resected, five-year PFS is significantly greater than those tumors with less resection (32). Because surgical resection is a key prognostic factor, hemispheric pHGGs are not surprisingly more treatable tumors compared to their midline and brainstem counterparts.

With any combination of chemotherapy, radiotherapy, and surgical resection the average median survival is only 12-15 months. Due to the ineffectiveness of standard therapeutic strategies, patients with pHGGs are frequently enrolled in clinical trials, and often enrolled in multiple trials as their tumors recur (26, 27, 33). These clinical trials have historically been designed from studies in aHGGs, which may owe to their ineffectiveness in the pediatric setting (9, 26, 34, 35). Studies also suggest there are multiple tumor cell subclones within the tumor microenvironment (TME) which may account for therapeutic resistance. As our understanding of the molecular alterations driving pHGGs increases, targeted therapies against molecular alterations and immune processes are becoming more popular (36-42). However, therapies designed to target non-neoplastic infiltrating cell types are lacking, and may be worth developing as these cell types constitute a large majority of cells within the total tumor cell mass, as demonstrated in the following pages of this document. The remainder of this dissertation will focus on these non-neoplastic cell types, specifically tumor associated macrophages (TAMs) and their role in the pHGG tumor microenvironment. Once we have a stronger foundational understanding of these cell types we can then design more effective targeted therapies to treat pHGGs.

PDGF Signaling in Pediatric Glioma

The platelet derived growth factor family is comprised of four ligands: PDGF-A, -B, -C, and -D, and two receptors: PDGFRα and PDGFRβ. Ligands can homo and hetero-dimerize to bind and activate their respective receptors. Each PDGF receptor has five extracellular domains, where ligand binding occurs at immunoglobulin-like domains 2 and 3, leading to receptor dimerization, stabilization between intracellular domains 4 and 5, and autophosphorylation between the two receptors (43-45). Phosphorylation of the ligand-receptor complex then leads to

conformational changes exposing catalytic sites for kinase activity and downstream signaling to occur. After the ligand-receptor complex has formed, it is then trafficked into endosomes via clathrin coated pits where signaling activity remains present until pH mediated dissociation of the ligand-receptor complex takes place, leading to monomerization and dephosphorylation (46). The phosphorylation sites of the PDGF receptors serve as activation sites for a variety of signaling molecules including but not limited to PI3K, PLC-gamma, Src, Grb2, RAS, and Shc (47-50). Additionally, the receptors can bind and activate members of the STAT family leading to downstream transcription factor activity (43). Together, the PDGF family is responsible for promoting cellular proliferation, division, survival, migration, and angiogenesis in a variety of developmental and tumor specific processes.

The most well studied members of the PDGF family are PDGFA and PDGFB. Both ligands consist of similar PDGF/VEGF core domains and N-terminal pro-peptide regions which require intracellular removal before extracellular secretion (51, 52). PDGF-BB and -AB induces the most potent responses upon receptor binding, as they can bind and activate PDGFR-αα, PDGFR-αβ, and PDGFR-ββ while PDGF-AA can only bind and activate PDGFR-αα and PDGFR-αβ (**Figure 2**) (49). Although these ligands initiate similar signaling pathways, there are distinct events and processes unique to each.

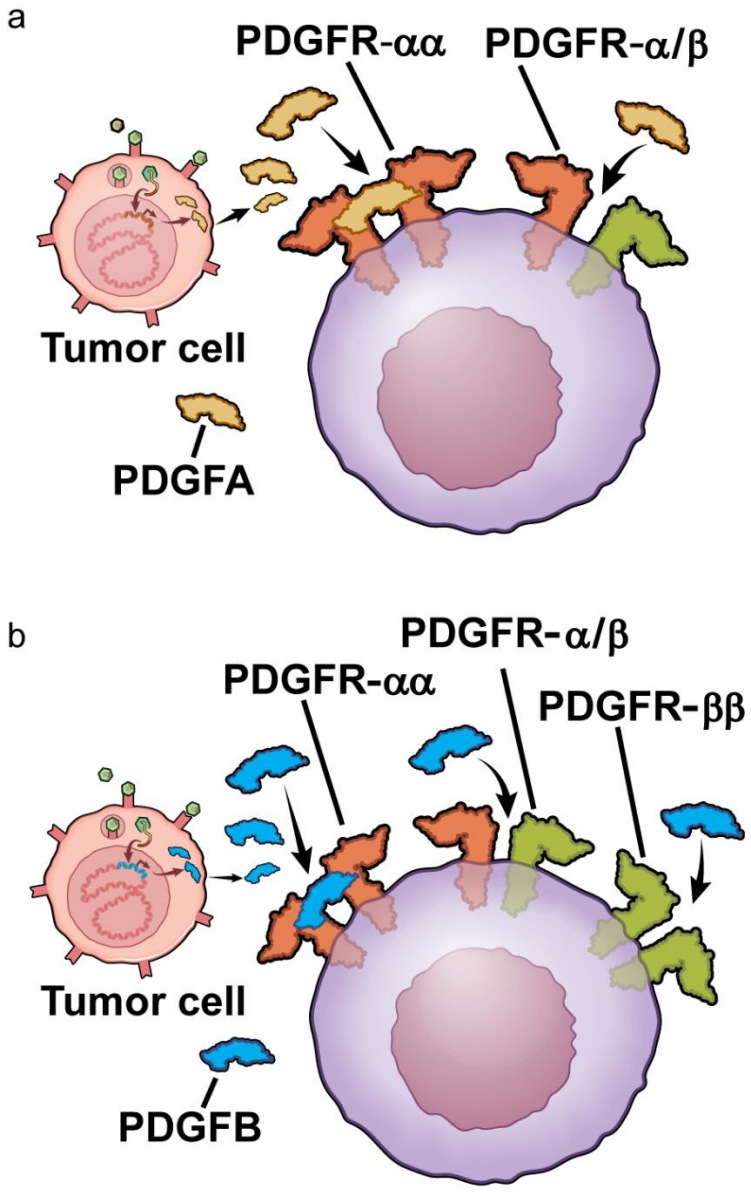

Figure 2: PDGF Pathway Ligand-Receptor Interactions. Schematic of the ligand and receptor binding interactions for PDGFA and PDGFB. PDGFA binds and activates PDGFRα only while PDGFB binds and activates both PDGFRα and PDGFRβ.

PDGFRα is widely expressed during embryonic development and is partially responsible for glial and neural progenitor cell proliferation and the development of oligodendrocytes (53, 54). It has also been found highly expressed in cells of mesenchymal origin including progenitor cells in the lungs, skin, intestine, as well as neural crest cells (50, 55, 56). PDGF-AA is expressed by neurons and astrocytes and can stimulate receptor activity in a paracrine fashion (53, 57-59). Embryos deficient in either PDGF-AA or PDGFRα are characterized by reduced numbers of oligodendrocyte progenitor cells and rarely survive postnatally. Those that do survive are known to have drastically reduced CNS myelination (60-62). On the contrary, overexpression of PDGFRα in developing embryos leads to increased growth of smooth muscle tissue and stromal fibroblasts, and defects in lung development. Further, adult mice experience tissue fibrosis in a variety of organs including the skin, heart, and intestines. These symptoms are enhanced when PDGFRα overexpression is combined with tumor suppressor loss *Ink4a/Arf-/-*, which also results in fibrosarcoma formation (63). Amplification of *PDGFRA*, present in both pHGG (~80%) and aHGG (5-10%), leads to high levels of the receptor on tumor cell surfaces (14). As a result, cells become sensitive to very low concentrations of PDGFA, leading to dysregulated PDGF signaling both *in vivo* and *in vitro* (64). In pHGG, *PDGFRA* amplification is commonly found with co-occurring mutations and deletions including *TP53* and *CDKN2A*. Tumor cells express PDGFRα, PDGFA, and PDGFB, often leading to autocrine and paracrine activation of the receptor and stimulating glioma progression.

Expressed in later stages of development, the most prominent role of the PDGFB/PDGFRβ pathway is in the development of blood vessels (49, 65). PDGF-BB secreted by endothelial cells and neurons binds to PDGFRβ on pericytes and vascular smooth muscle cells to induce proliferation and migration to newly forming vessels (51, 66-70). *In vivo*

experiments demonstrate PDGFB/PDGFRβ null embryos lack adequate smooth muscle cells and pericytes, leading to vascular defects including weakened vessel walls, hemorrhage, leakiness, enlarged vessel diameter, and edema (43, 71-74). The reduced numbers of pericytes leads to a dysfunctional BBB causing an influx of circulating molecules, proteins, and cells into the parenchyma that were previously prohibited from doing so (73, 75). Additionally, *PDGFB*$^{-/-}$ embryos display reduced mean hemoglobin concentrations, erythroblast counts, and platelet counts (76). In response to forced expression of PDGFB, multipotent neural progenitor cells switch their production of mixed glial and neuronal lineages towards the production of oligodendrocyte progenitor cells (77, 78).

While PDGFRα and its ligand are expressed in both low and high-grade gliomas, PDGFB is only found highly expressed in high-grade tumors (49, 79). Although PDGFRβ expression is absent from the majority of glioma cells, it is highly expressed in the stromal population and infiltrating macrophages who contribute to malignant tumor growth (52, 80-82). Tumor cells do however produce PDGFB and promote increased inflammation driven by cytokine production such as VEGF, EGF, TGFβ1, FGF, and IL-8 (83, 84). Once activated, PDGFRβ can then stimulate the activity of signaling molecules such as PI3K, MAPK, MEK, and NF-κB among others (85, 86). This signaling activity leads to hyperplastic stromal growth and lymphatic metastasis (87). As in breast, prostate, lung, and other epithelial tumors, PDGFRβ expression strongly correlates with poor patient prognosis in high-grade brain tumors (88-93). Overexpression of PDGFB *in vivo* leads to the generation of low-grade brain tumors, and when combined with additional genetic insults such as tumor suppressor deletions, high-grade tumors are formed (43). Tumors driven by PDGFB overexpression tend to be oligodendroglioma or mixed astrocytoma-oligodendrogliomas. When PDGFB is silenced by siRNA, glioma stemness

and tumor development is significantly inhibited (94). Much is known about PDGF signaling in the context of aHGG but little is known about its role and prognostic factors in the pediatric setting.

Chapter 2

Tumor Microenvironments and Cell Types Involved in pHGG

High grade gliomas are aggressive and infiltrative tumors, possessing distinct TMEs including tumor bulk, necrosis, and a leading edge which intermingles with normal brain parenchyma as the tumor expands (**Figure 3**). I have previously demonstrated in human adult GBM samples that protein expression levels vary among these regions, with pro-survival signaling elevated at the tumor margins and pro-thrombotic signaling elevated in the perinecrotic areas (8). Among these TMEs are distinct cell types which reside in unique niches. These cell types include; proliferating glioma tumor cells found throughout the entirety of the tumor, self-renewing glioma stem cells found in the perivascular niche, brain-resident microglia found in the peritumoral regions, infiltrating bone-marrow derived monocytes (BMDM) and other immune cells which are found throughout the tumor, especially around blood vessels and perinecrotic regions (95-97). My work is particularly focused on microglia and BMDMs, which collectively are referred to as TAMs.

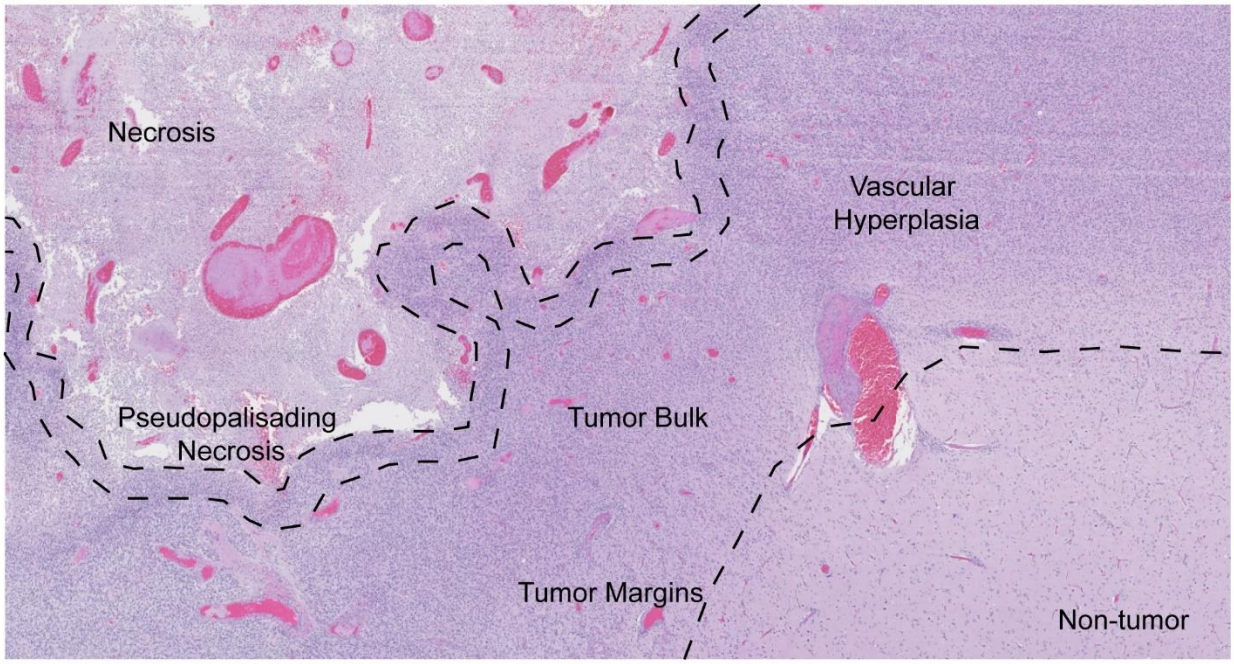

Figure 3: Tumor Microenvironments in High-Grade Gliomas. H&E staining of a human pHGG sample displaying the histological hallmarks of a high-grade glioma. These features include a dense tumor bulk with microvascular hyperplasia, infiltrating tumor margins, multiple necrotic cores, and pseudopalisading necrosis.

Tumor Associated Macrophages in HGG

The following is adapted from the manuscript: ***Chen, Z.*, ***Ross, J.*, *Hambardzumyan, D. (2019). Two Photon Imaging Reveals Distinct Morphology and Infiltrative Properties of Glioblastoma-Associated Macrophages and Microglia. Proceedings of the National Academy of Sciences.* ***These authors contributed equally.*

TAMs symbiotically interact with tumor cells by the secretion of growth factors, matrix metalloproteinases, and other factors that promote tumor cell invasion and progression (97, 98). We have previously demonstrated TAMs constitute up to 40% of the total tumor mass both in human and mouse GBM (97, 99). Further, we demonstrated in a PDGFB-driven genetically engineered mouse model (GEMM) of GBM that over 80% of these cells were BMDMs that had infiltrated from the vasculature (95). A recent elegant study using single-cell profiling of human GBM confirmed our data and showed monocytes significantly infiltrate pre-treatment human gliomas to a degree that varies by glioma subtype and tumor compartment (100). BMDMs do not universally conform to the phenotype of microglia, but preferentially express immunosuppressive cytokines and show an altered metabolism. These findings, together with ours, argue against traditional therapeutic strategies that target TAMs indiscriminately and instead favor strategies that specifically target immunosuppressive BMDMs.

Monocytes develop from hematopoietic stem cell progenitors and remain in the intact vasculature of the brain, with their infiltration into surrounding tissue hindered by the BBB (97) (**Figure 4a,e**). However, during GBM tumor progression, increased expression of monocyte chemoattractant proteins (MCPs) (101) in combination with the disruption in BBB integrity results in inflammatory monocyte infiltration into the perivascular niche (102) (**Figure 4b,e**). Once inside the tissue, infiltrating monocytes can then differentiate into macrophages and exert pro-tumor

effects (103). We have previously demonstrated genetic decrease of the CCL2/CCR2 axis in adult GBM reduced monocyte infiltration but was not sufficient to completely ablate it, suggesting other mechanisms are also responsible for the recruitment of these cells (95).

Unlike BMDMs, microglia are always present in the central nervous system and are homogeneously dispersed throughout the brain (**Figure 4c**). These long-lived cells develop from embryonic yolk sac progenitor cells during embryogenesis, and are responsible for the clearing of pathogens and maintenance of synaptic processes (104, 105). In their activated state, microglia produce pro-inflammatory cytokines and reactive oxygen species, assume an amoeboid morphology, and have historically become histologically indistinguishable from infiltrating BMDMs (106, 107). In contrast to BMDMs which are found in tumor bulk and infiltrating tumor margins, microglia are found sparsely distributed throughout the tumor bulk and accumulate at the periphery (102) (**Figure 4d,e**). When freshly dissociated patient GBM samples were analyzed for BMDMs and resident microglia, there was a significant infiltration of BMDMs across the GBM subtypes. Only the mesenchymal subtype of adult GBM showed increased microglia infiltration compared to BMDMs (108).

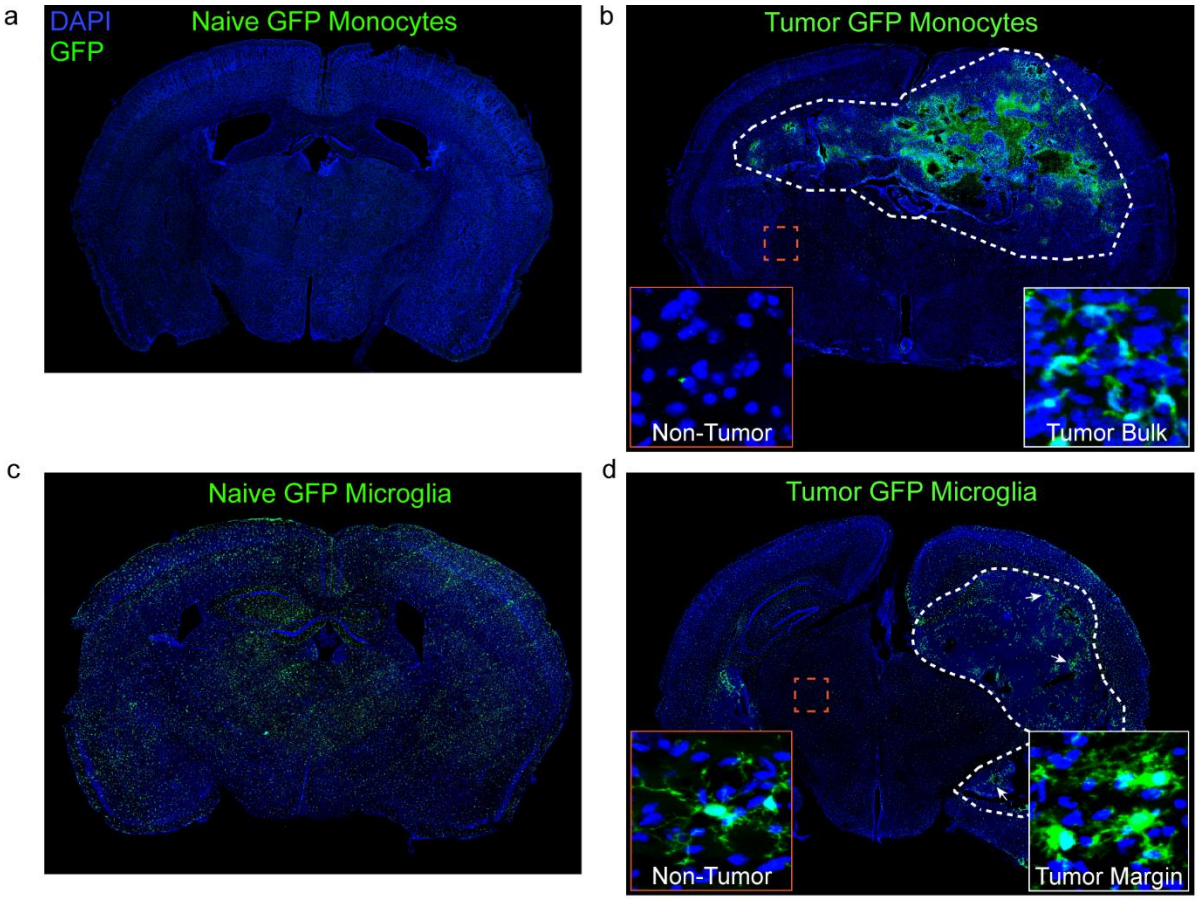
a
DAPI
GFP
Naive GFP Monocytes
b
Tumor GFP Monocytes
Non-Tumor
Tumor Bulk
c
Naive GFP Microglia
d
Tumor GFP Microglia
Non-Tumor
Tumor Margin

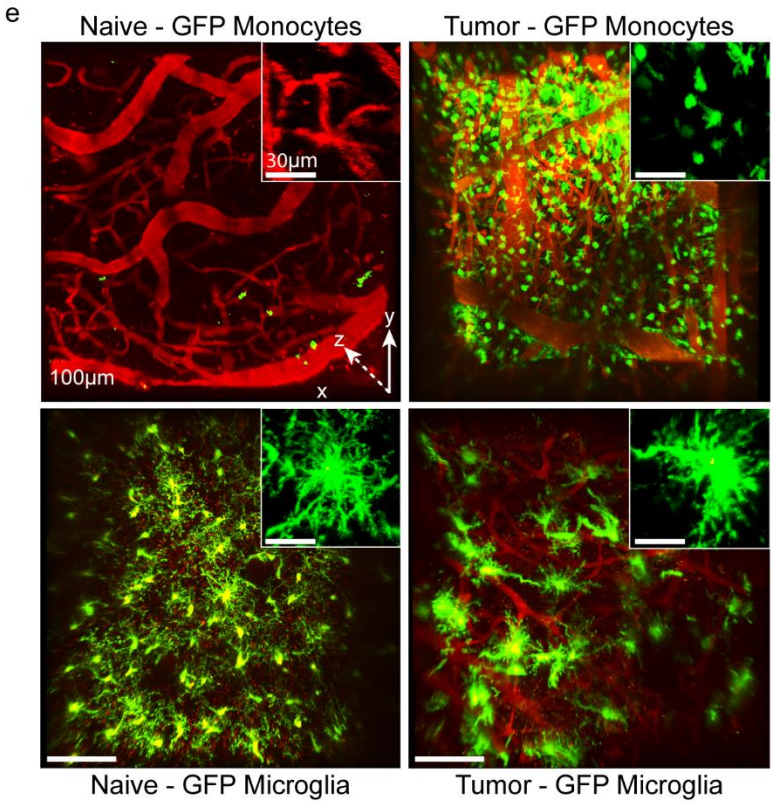
e
Naive - GFP Monocytes
Tumor - GFP Monocytes
30µm
100µm
y
z
x
Naive - GFP Microglia
Tumor - GFP Microglia

Figure 4: Tumor Associated Macrophage Infiltration in Glioblastoma. (a) 10x Z-stitch immunofluorescence image of a naïve *Cx3cr1*$^{GFP/WT}$ →*Cx3cr1*$^{WT/WT}$ chimeric (GFP-monocytes) mouse. **(b)** 10x Z-stitch immunofluorescence image of a tumor bearing *Cx3cr1*$^{GFP/WT}$→*Cx3cr1*$^{WT/WT}$ chimeric mouse. Note the presence of GFP signal only in tumor tissue. GFP=monocytes, DAPI=nuclei. **(c)** 10x Z-stitch immunofluorescence image of a naïve *Cx3cr*$^{WT/WT}$→*Cx3cr1*$^{GFP/WT}$ chimeric (GFP-microglia) mouse. Microglia are found distributed throughout the entirety of the brain. **(d)** 10x Z-stitch immunofluorescence image of a tumor bearing *Cx3cr1*$^{WT/WT}$→*Cx3cr1*$^{GFP/WT}$ mouse. Microglia are unevenly distributed in the tumor bulk and accumulate at the tumor margins in distinct clusters (white arrows). **(e)** Raw z-stack images acquired from two-photon imaging of naïve and tumor bearing mice with GFP-BMDMs (top row) and GFP-microglia (bottom row). Scale bar=100μm, magnified inset scale=30μm.

Two-photon microscopy has previously been employed for the longitudinal analysis of adult GBM growth kinetics, vascular dynamics, and immune cell infiltration (109-112). However, the contributions of individual TAM populations have largely been ignored as microglia and circulating monocytes are typically grouped together and treated as one collective entity. Although we have a firm understanding of TAMs in the context of tumor growth promotion and immune suppression, the majority of histopathological studies are limited to static snapshots of the disease over time. If we seek to identify therapeutic points of intervention we must understand how these cell types interact with their microenvironment in real time. Further, the development of cell-type specific targeted therapies will be made possible if we study not only the TAM population as a whole, but also by identifying biological differences between the two aforementioned subtypes. In this study we performed live *in vivo* two-photon microscopy in an immunocompetent GEMM of adult GBM together with myeloid cell specific reporter mice to lineage trace microglia and BMDMs. By taking advantage of reciprocal bone marrow chimeras between *Cx3cr1*$^{GFP/WT}$ and wild type mice, we demonstrated the feasibility of using an open skull window for the imaging of TAM subpopulations in tumor tissue (**Figure 5a-d**). We observed tumor microglia and infiltrating BMDMs are morphologically distinct cell populations that possess differential migratory capacities. We further showed anti-VEGFA treatment significantly decreases infiltration and induces a morphological switch in BMDMs, resembling differentiated macrophages. This study also demonstrates BBB integrity is not the sole driver of monocyte infiltration and provides rationale for combining anti-angiogenic therapies with anti-chemotaxis (targeting members of MCP family) therapies to block monocyte infiltration.

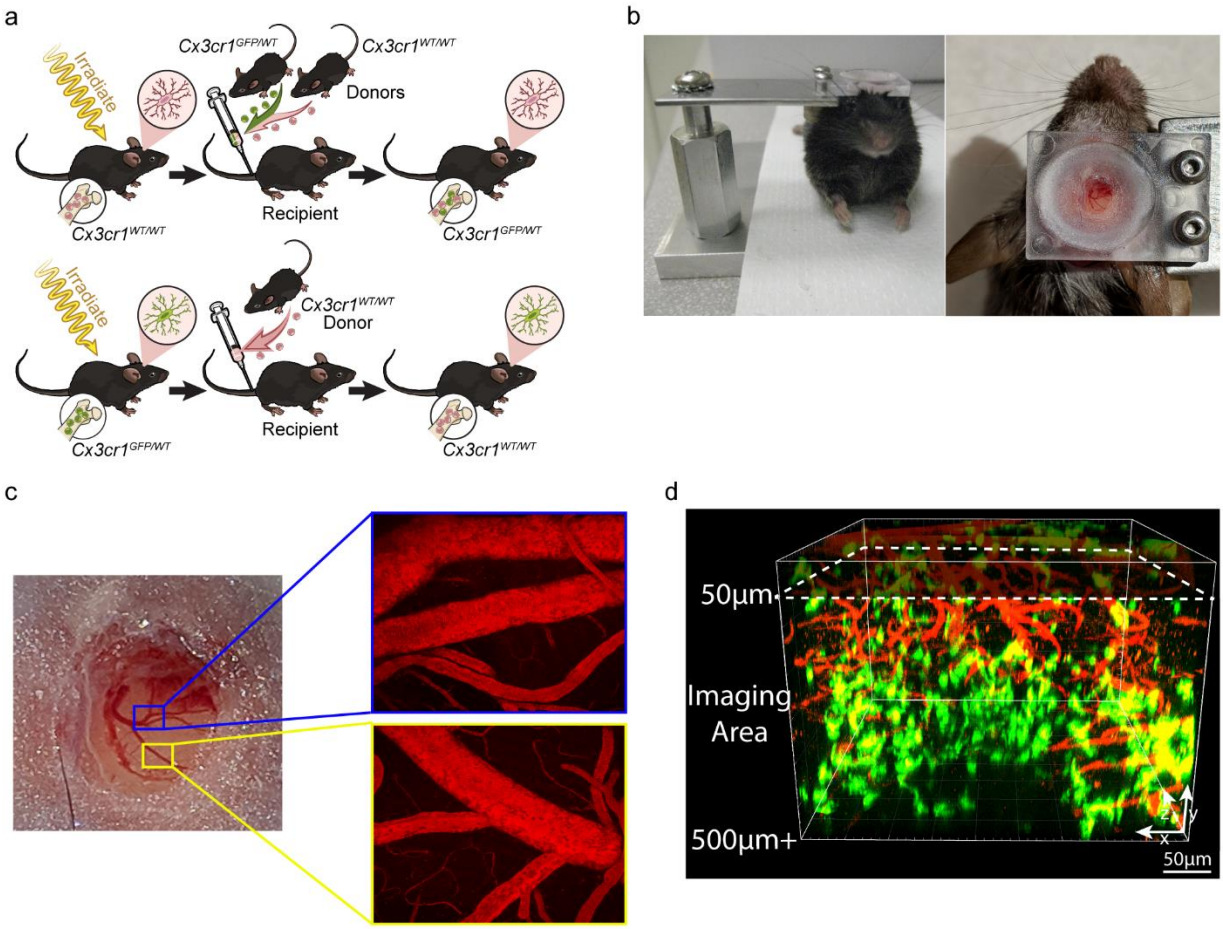

Figure 5: Two-Photon Imaging in Live, Tumor Bearing Mice. (a) Bone marrow chimera schematic depicting the generation of mice with GFP-labeled BMDMs or GFP-labeled microglia. **(b)** A custom acrylic adapter attaches the mouse to a steel stage to stabilize the imaging plane and reduce movement artifacts. **(c)** Superficial tumors and vascular landmarks can be observed by eye and low magnification. **(d)** High resolution z-stacks were imported into Imaris where image processing and analysis occurred. TRITC=vessels, GFP=TAMs. All image analysis was performed at a depth of >50µm below the pial surface and down to ~500µm deep.

Our findings from this study demonstrate microglia are large, branched cells, with highly active processes that extend and retract in a sensing manner in both naïve and tumor contexts (**Figure 6a-e**).These results confirm our previous understanding that even in the absence of a stimulus microglia are constantly surveying their microenvironment through the continuous extension and retraction of ramified projections (113, 114). We did not observe any instances of microglial cell body migration, in line with previous findings that the movement of microglial soma is limited (**Figure 6f**)(115). Conversely, we observed infiltrating BMDMs are minimally branched and highly migratory. We observed as cells upregulate their expression of CX3CR1 as indicated by GFP intensity, their migration capacity decreases (**Figure 6a-i**). These results imply BMDM cell migration is a function of the state of differentiation or morphological phenotype.

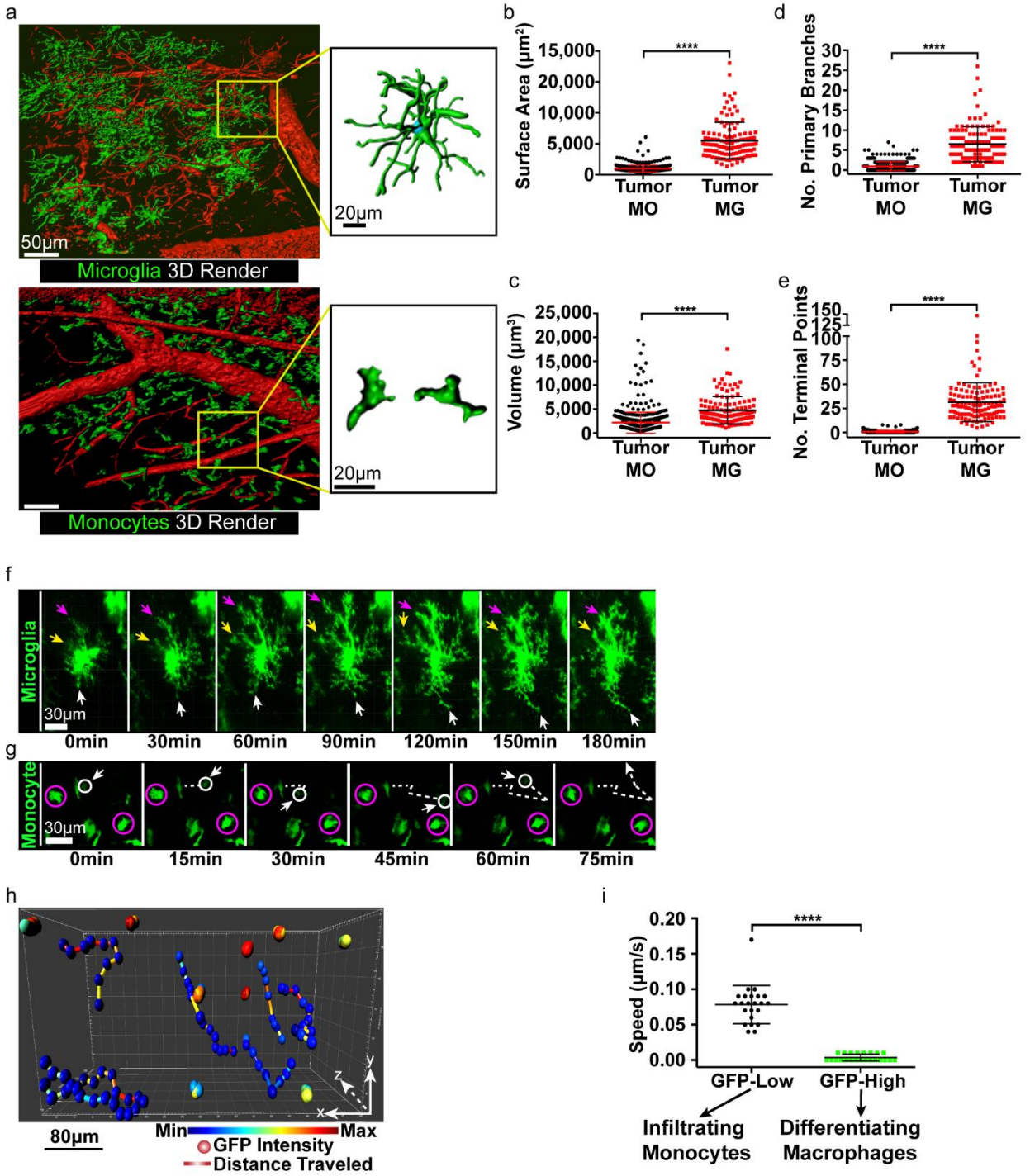
a
50μm
20μm
Microglia 3D Render
Monocytes 3D Render
b
Surface Area (μm²)
15,000
20,000
10,000
5,000
0
****
Tumor MO
Tumor MG
c
Volume (μm³)
25,000
20,000
15,000
10,000
5,000
0
****
Tumor MO
Tumor MG
d
No. Primary Branches
30
25
20
15
10
5
0
****
Tumor MO
Tumor MG
e
No. Terminal Points
150
125
100
75
50
25
0
****
Tumor MO
Tumor MG
f
Microglia
30μm
0min
30min
60min
90min
120min
150min
180min
g
Monocyte
30μm
0min
15min
30min
45min
60min
75min
h
80μm
Min
Max
GFP Intensity
Distance Traveled
i
Speed (μm/s)
0.20
0.15
0.10
0.05
0.00
****
GFP-Low
GFP-High
Infiltrating Monocytes
Differentiating Macrophages

Figure 6: Morphologic Features of Tumor Associated BMDMs and Microglia. (a) 3D renderings of GFP-microglia ("MG", top row) and GFP-BMDM ("MO", bottom row) image stacks using Imaris. Scale bar=50μm, magnified inset scale=20μm. **(b)** Single cell morphology statistics for surface area. Two-tailed *t*-test, ****p<0.0001. **(c)** Cell volume. Two-tailed *t*-test, p<0.0001. **(d)** Number of primary branches for each cell. Mann-Whitney *U* test, p<0.0001. **(e)** Terminal points per cell. Mann-Whitney *U* test, p<0.0001. Tumor MO n=543 cells from n=7 mice, Tumor MG n=123 cells from n=4 mice. **(f)** Time lapse imaging of a stationary tumor microglia over 180 minutes. Arrows indicate extension and retraction of individual cell processes. Scale bar=30μm. **(g)** Individual cell tracking of a Low-GFP expressing monocyte (white circle) compared to High-GFP expressing cells (purple circles). Dashed line indicates path of cell over 75 minutes. Scale bar=30μm. **(h)** Cell tracking using Imaris spots function. Spheres indicate individual cell position at each time point and are colored according to GFP intensity. Movement tracks are colored by distance traveled by each cell. **(i)** Speed of individual cells with low (n=22 cells from n=7 mice) and high (n=22 cells from n=3 mice) GFP intensity. Two-tailed *t*-test, ****p<0.0001.

Recent studies have demonstrated anti-VEGFA therapy causes an increased infiltration of monocytic macrophages into the tumor in recurrent GBM using a xenograft mouse model (116). Evidence also suggests in response to anti-VEGFA blockade, infiltrating myeloid cell populations initially decrease but then rapidly increase as the tumor progresses (117). Although we observed a decrease in this population via two-photon imaging, our model captures the biology of primary tumors, not recurrent tumors, and is performed in immunocompetent mice which may explain discrepancies from our findings and others. Vascular normalization has been attributed to anti-VEGFA therapy, which may explain the early decrease in myeloid cell populations (118-120). However, over time as the tumor grows, hypoxia increases, providing infiltrating cells with the chemokines and stimulating factors necessary for their recruitment (121-123). In our studies, we observed a decrease in the $CX3CR1^{+}$ myeloid population after B20-4.1.1 (Anti-VEGF) treatment and an extension in survival (**Figure 7a-c**). Additionally, in response to treatment, monocytes assumed a more branched phenotype suggesting VEGFA sequestration promotes differentiation of these cells (**Figure 7d-l**). As TAMs have been shown to promote tumor vascularization, one scenario remains in question: are BMDMs that are present during anti-VEGFA therapy becoming trapped in the tumor and promoting vascularization over time (124, 125)? Although not performed in this study, longitudinal imaging over the course of anti-VEGFA treatment could answer this question and may determine mechanisms of resistance that would otherwise go unobserved using other methods.

In conjunction with our previous study demonstrating genetic loss of CCL2/CCR2 partially decreases monocyte infiltration in adult GBM, our findings that B20-4.1.1 also partially reduces this population demonstrate monocyte infiltration is not due solely to a compromised BBB or chemokine gradients (95). Together, this data provides a clear rationale for combining

anti-VEGF therapy with chemotaxis blockade, such as anti-CCL2/CCR2, to block BMDM infiltration into GBM. The findings of these studies have far reaching implications beyond their applications in GBM. Open skull window two-photon imaging techniques coupled with chimeric mouse models could be applied for the study of stroke and other neurological disorders in which microglia and bone marrow derived monocytes have been known to play differential roles (126-129). Additionally, deciphering mechanisms of macrophage recruitment to pathogenic sites will lead to improved targeted therapies for the treatment of these diseases.

Although informative, all of the aforementioned studies performed on TAMs have been performed in adult HGGs and the knowledge extrapolated to pHGGs. Since pHGGs are genetically and anatomically distinct from their adult counterparts, we need to develop a deeper understanding of TAMs and the roles they play in the pHGG TME. We hypothesize the general infiltrative mechanisms of BMDMs are similar between the two entities, yet pHGGs may possess their own unique inflammatory profiles differentiating them from aHGGs. The remainder of this dissertation will focus on characterizing the inflammatory microenvironment of human and murine pHGGs to gain insights into their infiltrative mechanisms and malignant capabilities. We utilize formalin fixed paraffin embedded (FFPE) human pHGG tissue samples and complement these studies with immunocompetent GEMMs driven by PDGFA or PDGFB signaling.

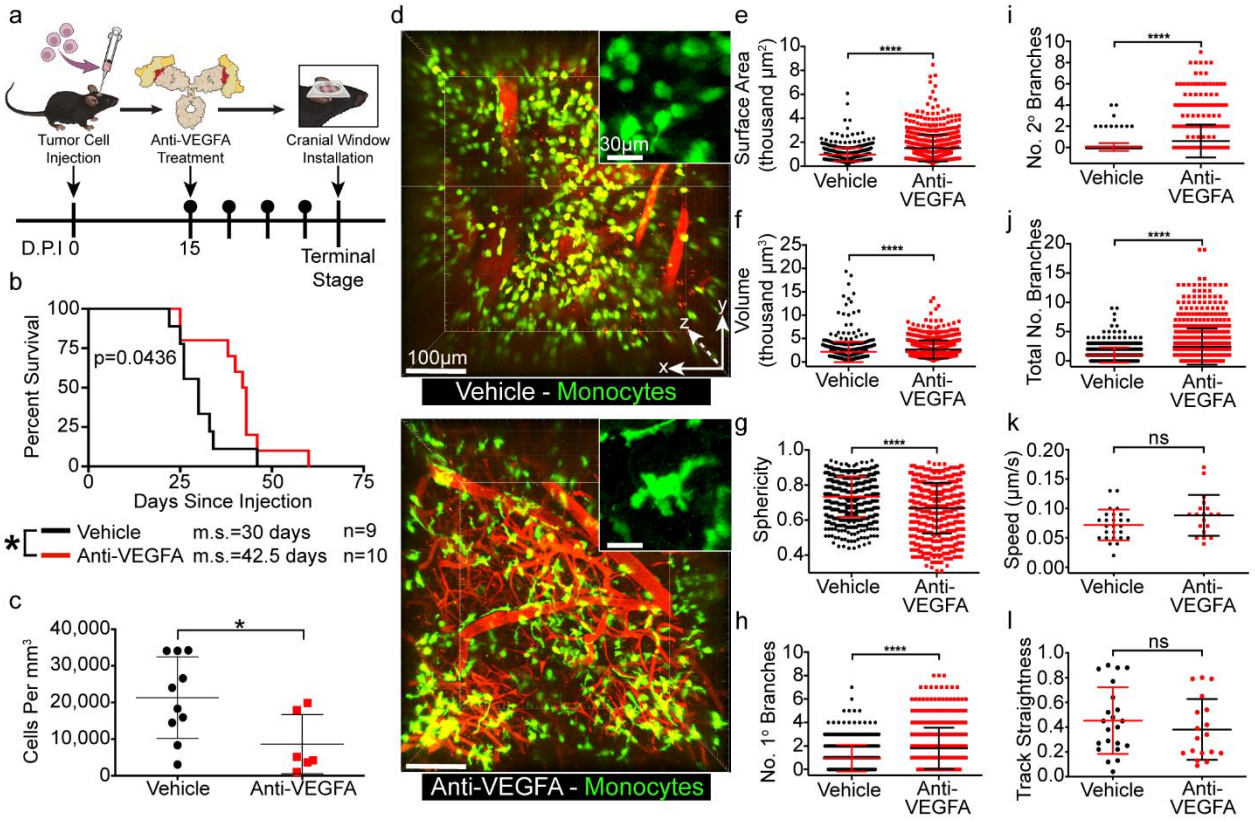

Figure 7: Anti-VEGFA Treatment Reduces TAM Infiltration and Induces a Morphological Response. (a) Timeline of treatment schedule and imaging of anti-VEGFA treated mice. D.P.I.=days post injection. **(b)** Kaplan-Meier survival curves for vehicle treated mice (n=9, m.s.=30 days) and anti-VEGFA treated mice (n=10, m.s.=42.5 days). p=0.0436. m.s.=median survival. **(c)** Quantification of cell populations acquired from individual imaging volumes. **(d)** Representative image stacks acquired during two-photon imaging of mice with GFP labeled BMDMs for vehicle treated and anti-VEGFA treated animals. Scale bar=100μm, magnified inset scale=30μm. **(e)** Single cell morphology statistics for surface area. Two-tailed *t*-test, ****p<0.0001. **(f)** Cell volume. Two-tailed *t*-test, p<0.0001. **(g)** Sphericity (1.0=perfect sphere, 0=not spherical). Two-tailed *t*-test, p<0.0001. **(h)** Number of primary branches for each cell. Mann-Whitney *U* test, p<0.0001. **(i)** Number of secondary branches for each cell. Mann-Whitney

U test, p<0.0001. **(j)** Total number of branches for each cell. Mann-Whitney *U* test, p<0.0001. Vehicle MO n=543 cells from n=7 mice, Anti-VEGFA MO n=717 cells from n=7 mice. **(k)** Speed of individual cells. Two-tailed *t*-test. **(l)** Cell migration track straightness (1.0=straight line). Two-tailed *t*-test. Vehicle=26 cells from n=5 mice, Anti-VEGFA=19 cells from n=5 mice.

Methods

Mice

Animals were housed in Emory University Division of Animal Resources. Adult mice of either gender were kept on a 12h-12h light/dark cycle with access to food and water ad libitum. We used age and sex as criteria to equally distribute mice from different genotypes for all the experiments. All experimental procedures were approved by the Institutional Animal Care and Use Committee of Emory University.

Bone Marrow Chimera

To ablate recipient mice hematopoietic systems, four to five-week-old B6 *Cx3cr1*$^{WT/WT}$ or *Cx3cr1*$^{GFP/WT}$ mice were whole-body irradiated in a Shepherd Mark 137^{Cs} irradiator in two doses at 600 rads each with a four-hour interval. Bone marrow cells were harvested from femurs and tibias of donor mice and suspended at a concentration of $1x10^8$ cells/mL in sterile HBSS. $1x10^7$ cells were then retro-orbitally injected in each recipient mouse following the last irradiation dose. Recipient mice received 1.2 mg/mL gentamicin for ten days through sterile drinking water. To determine reconstitution efficiency of the procedure, 50 uL of blood was collected via tail vein incision from recipient mice eight to ten weeks after transplant. Erythrocyte lysing buffer (BioLegend, 420301) was used to lyse red blood cells, leukocytes were then analyzed for Ly6C and GFP expression using a BD LSR II flow cytometer (6) (**Figure 8a**).

RCAS-Tva System Mediated Tumor Induction

DF1 cells (ATCC) were grown at 39^{o}C, expanded to passage 4 and transfected with RCAS-PDGFB-HA using a Fugene 6 Transfection kit (Roche, no. 11814443001). Cells were cultured with DMEM media (Gibco, 11995-065) supplemented with 1% L-glutamine, 1% penicillin/streptomycin, and 10% FBS (ATCC). DF1 cells were injected as equal mixtures of

$4x10^4$ cells per µL, 1 µL per mouse, in adult *Nestin-tv-a; Ink4a-Arf*$^{-/-}$*; Pten*$^{fl/fl}$ donor mice using a 30-gauge needle attached to a Hamilton syringe. For a detailed review of the RCAS-Tva system, please see the following cited articles (130-132).

Orthotopic Cell Injections

We use the RCAS-Tva system to generate *de novo* primary murine GBM as previously described (95, 133). Once tumors were formed in donor transgenic mice, tumor cells were freshly dissociated and $2.5x10^4$ cells were superficially injected into the right frontal striatum of recipient mice eight to ten weeks after bone marrow transplant using the following coordinates: bregma AP (anterior/posterior) 0.2 mm, ML (medial/lateral) 1.0 mm, over which a bur hole was made with a sterile 19007-7 drill bit (Diameter=0.7 mm, Fine Science Tools). A Hamilton syringe affixed to a stereotactic apparatus was then lowered to 1.0 mm depth, and a total of 1 µl cell suspension was injected through a 30-gauge needle. (**Figure 8b**)

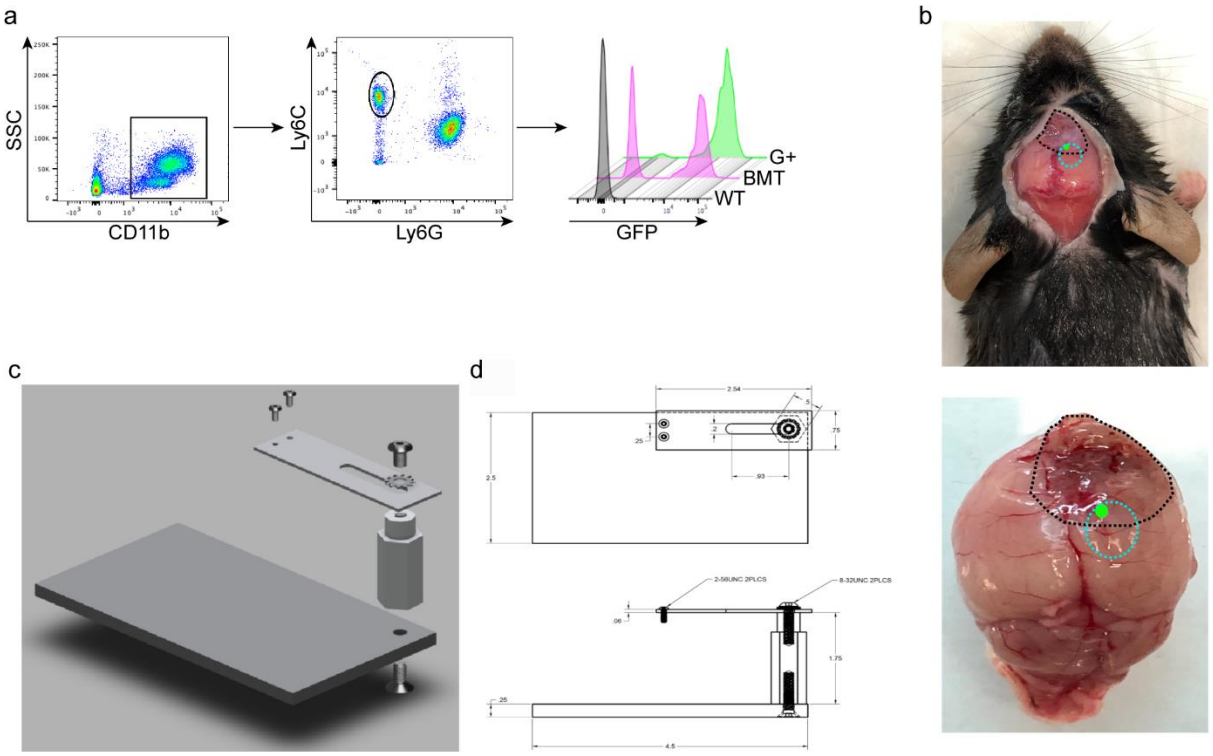

Figure 8: Model Validation for TAM Imaging in Adult Murine GBM. (a) Circulating myeloid cells are gated by their CD11b positivity. Inflammatory monocytes are further identified by their high expression of Ly6C and devoid of Ly6G. CX3CR1-GFP expression in these gated inflammatory monocytes are compared between the wild-type (WT), bone-marrow chimera (BMT), and $Cx3cr1^{GFP/WT}$ (G+) mice. **(b)** (Top) View of mouse skull and a superficial tumor before performing craniotomy for skull window placement. The location of craniotomy for cell injections is demarcated by the green circle. The skull windows were placed above the tumors so as to include both tumor margin and tumor bulk in the imaging plane (blue dashed circle). The tumor is outlined in black. (Bottom) View of mouse tumor after removing the skull. The tumor is easily visualized by eye. **(c)** An aluminum stage was made at the Emory University Machine Shop as depicted above. During 2-photon imaging sessions, an adapter which is fixed to the mouse skull is attached to the aluminum stage by the two small screws on top of the plate. The

stage eliminates oscillatory imaging artifacts produced by breathing movements of the animals. At the end of each imaging session mice are released from the stage. **(d)** Dimensions used to create the aluminum stage. Scale is in inches.

Open Skull Window and Two Photon Imaging

About 3 weeks following tumor transplantation, mice began to show neurological signs of brain tumor. At this point they were anesthetized with a cocktail of Ketamine/Xylazine (100 mg/kg; 10 mg/kg, ip) and placed in prone position in a stereotactic apparatus. A skin incision was made on the dorsal midline of the skull along the rostro-caudal axis, exposing the bregma. While leaving the underlying dura mater intact, a ~3.0mm diameter craniotomy over the right cortex was made with a micro-drill in a way that the frontal edge of the craniotomy merged with the bur hole where tumor cells were injected. The exposed dura mater was covered with a sterile circular coverslip 5mm in diameter (Electron Microscopy Sciences) which was carefully placed to facilitate visual access to tumor bulk and tumor margin. The coverslip was attached to the skull first by cyanoacrylate adhesive, followed by methyl methacrylate resin cement. At the time of imaging, TRITC-Dextran (2.5 mg/ml, Sigma) was injected intravenously to outline the blood vessels. Mice were fixed to a custom-built stage to minimize breathing artifacts during image acquisition (**Figure 8c-d**). A quarter dose of Ketamine/Xylazine was administered every hour throughout the procedure to maintain sedation. Images were acquired with a 25X water immersion objective (Leica, NA 0.95) on a Leica SP8 confocal microscope equipped with a tunable pulsed chameleon infrared multiphoton laser (Coherent). Two high-sensitivity hybrid-PMT (HyD) detectors (Leica) were used with two band-pass filters (525/50 and 585/40) placed in front of the detectors for GFP and TRITC detection, respectively. To eliminate imaging in necrotic regions, only areas where single cells and intact vasculature could be observed were chosen for analysis. High-resolution xyz-stack images (1024x1024 pixels per z step) were taken with a step size of 2.5 μm, and XYZT stacks were taken every 2.5 minutes for about 3 h on average. Acquired images were then imported into Imaris (Bitplane, Belfast UK) for further

analysis. At the end of each imaging session, the mice were euthanized and their brains were processed for confocal imaging as previously described (95).

Immunofluorescent Staining

After Intravital imaging, mice were perfused with 4% paraformaldehyde and brains were transferred to 30% sucrose the following day. Samples were then embedded in OCT (Sakura Finetek) and stored at -20ºC. 30 μm frozen sections were cut on a Leica CM1860 cryostat. Tissues were stained with DAPI (1:1000) and images were acquired on an Olympus FV1000 confocal microscope to confirm the presence of tumor.

Data Analysis in Imaris

High-resolution image stacks were imported into Imaris version 9.0.2 (Bitplane, Belfast UK). For quantification of total cell numbers within each xyz stack, the spots function was used. GFP+ microglia were identified by selecting for spots with an estimated XY diameter of 12 μm or greater. GFP+ monocytes were identified by selecting for cells with an estimated XY diameter 8.0 μm or greater. Values were then converted to the number of cells per mm^3 according to the size of the imaging volume.

For morphology analysis of BMDMs, the default Imaris Surfaces function was used and cell branching was manually quantified. For morphology analysis of microglia, the Imaris Filaments function was used. Microglia were considered to be “filaments” and microglia branches were considered as “dendrites.” Settings for data acquisition were: autopath no loops, starting point largest diameter=21.6 μm, seed points thinnest diameter=1.30 μm, diameter of sphere region=40.0 μm. After conversion to filaments, single cells were individually and manually analyzed to ensure data integrity (**Figure 9a-f**). For quantification of cell velocity, the Imaris spots function was used.

Cells were manually selected and their paths of migration were traced. Cells that were in frame for more than 3 continuous time points were included.

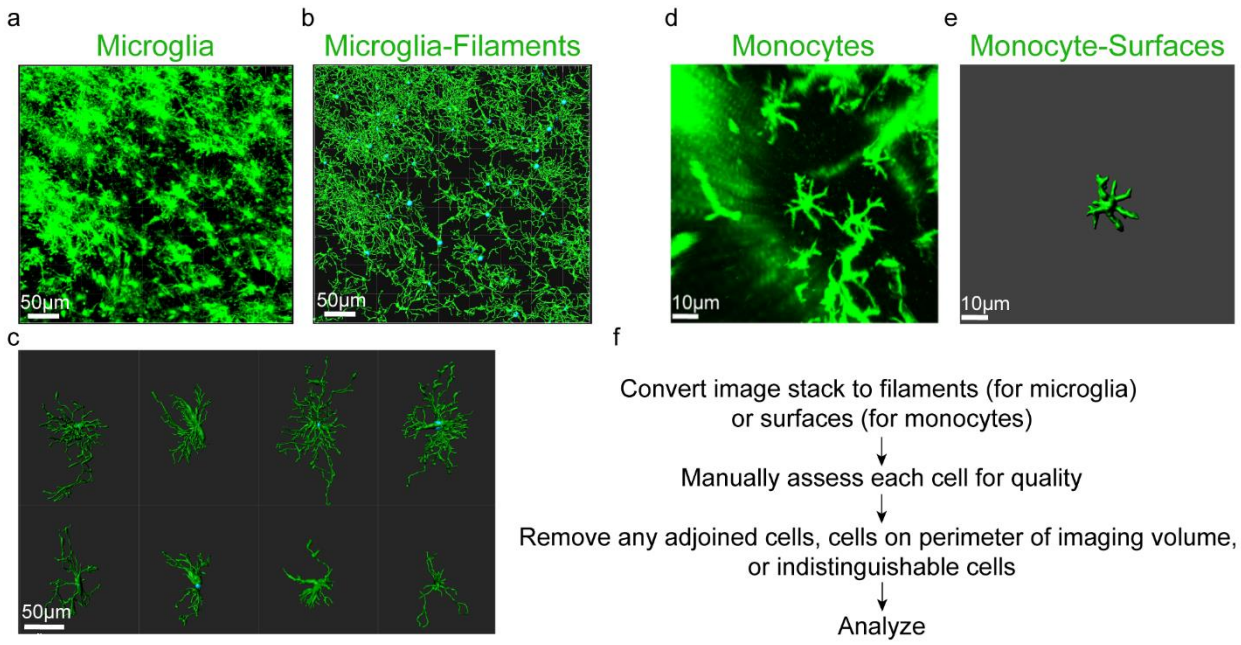

Figure 9: Approach To Analyzing TAM Morphology. (a) Raw XYZ stack of GFP expressing microglia acquired during in vivo two-photon imaging. **(b)** XYZ stacks are imported into Imaris and converted to filaments using the filaments function. **(c)** Individual cells can then be reviewed for quality control and morphology analysis by using established Imaris algorithms. **(d-e)** Raw XYZ stack of GFP-expressing monocytes acquired during in vivo two-photon imaging. **(f)** XYZ stacks are imported into Imaris and converted to surfaces using the surfaces function. Each cell can then be individually analyzed for quality control and morphology analysis.

Chapter 3

Inflammatory Microenvironment of Human pHGGs

Little is known concerning the inflammatory microenvironment of pHGGs, and due to the lack of sufficient studies and limited sample sizes there are mixed findings throughout. It has been reported human pediatric high-grade gliomas have low numbers of myeloid and lymphoid cells (134-136). However, in pediatric pilocytic astrocytoma, ependymoma, and GBM there is a significantly higher amount of infiltrating $CD45^+CD11b^+$ myeloid cells compared to normal brain (135). Additionally, IBA1 staining in DIPG samples demonstrated an increase in infiltrating TAMs when compared to non-tumor brain tissue (137). When comparing DIPG to adult GBM samples, Lin et al. also found a significant increase in the $CD45^+CD11b^+$ infiltrate and minimal $CD3^+$ T-cells in the DIPG cohort (137).

Interestingly, when comparing pLGGs to pHGGs, Lieberman et al. found pLGGs have greater chemokine expression compared to pHGGs, as shown by NanoString for *CCL2, CCL3,* and *CCL4* (134). Another study by Plant et al. found greater infiltration of $CD45^+$ immune cells and $CD8^+$ T-cells in the pLGG cohort as shown by immunohistochemical staining (136). However, when flow cytometry was performed on these samples, no differences were found among the $CD4^+$ and $CD8^+$ T-cells, NK cells, or myeloid populations. Only one lymphocyte population was found to be enriched in the pHGG samples which was the $CD45^+CD19^+$ and $CD45^+CD38^+IgD^+$ B-cells (136). It has previously been demonstrated pHGGs with higher mutational burdens have elevated levels of neo-antigens, however these studies were limited to only four cases (38). It is thought that the increased antigenic load increases the amount of MHC-1 presentation and therefore encouraging cytotoxic activity, yet more studies are required to substantiate these claims (9, 38, 136, 138).

Studies on DIPG tumor samples are extremely limited due to their sensitive location within the brain which renders them unlikely candidates for tumor biopsy or tumor resection. With this in mind, H3K27M DIPG tumors present a unique opportunity for targeted immunotherapies due to their exclusive expression of the mutated histone only in tumor cells. Unfortunately, it has been demonstrated these tumors are immune cold due to a lack of infiltrating T-lymphocytes (9, 137). Considering these limited findings, therapeutic strategies may need to focus on improving T-lymphocyte trafficking into the tumor itself, and then amplifying the cytotoxic response. Macrophage directed therapies may prove to be more beneficial for pHGGs as this is the one immunological cell population found consistently in all tumor locations.

NanoString Analysis of Human pHGGs

Within the limited studies previously discussed, there has been little to no comparison of hemispheric pHGGs to brainstem pHGGs/DIPGs in terms of their inflammatory microenvironments and infiltrating immune cells. To characterize these tumors, we obtained FFPE tissue blocks of 20 pHGGs and performed NanoString analysis (**Figure 10a**). Among these samples were 13 hemispheric pHGGs, 3 of which were also G34R mutant, and 7 brainstem pHGGs, 4 of which were known to have the H3K27M mutation while 3 others were unknown. When comparing the differentially expressed (DE) genes between the two subgroups, DIPG samples had higher expression of leukocyte-attracting chemokines such as *CXCL2*, *CXCL5*, and *CXCL6*. *IL8*, a neutrophil chemotactic factor which strongly induces *CXCR2* activity and expression was also highly expressed in these samples (139). Most significantly differentially expressed between the two subgroups was *CXCL1* (high in DIPG), which is also a neutrophil chemoattractant molecule and potent promoter of inflammation **(Figure 10b**). CXCL1 has been

shown to be produced by mast cells and macrophages, and plays a critical role in the recruitment and migration of immune cells to sites of inflammation (140). Further, in a model of pancreatic adenocarcinoma, high *CXCL1* expression correlated with low T-cell infiltration, and deletion of *CXCL1* rendered immunotherapy resistant tumors susceptible to CTLA-4 and PD1 blockade (141). All of these gene products signal through the CXCR2 receptor, indicating a possible role for this signaling pathway in DIPGs. DIPGs also had higher expression of the lymphocyte homing and activation factor, *CD44*. When comparing the pathways represented by the expressed genes in these samples, unsupervised hierarchical clustering displayed moderate separation between the two subgroups of pHGG. 5/7 DIPG samples clustered together while the hemispheric samples mainly clustered together **(Figure 10c**). Interestingly, DIPGs had greater expression of genes involved in pathways including chemokine and cytokine signaling, leukocyte functions, B and T-cell functions, and macrophage functions, among others. These results suggest DIPGs have a greater inflammatory microenvironment when compared to hemispheric pHGGs. This is intriguing since DIPGs are considered more aggressive yet have historically been considered immune cold.

When examining only hemispheric samples, two distinct sub-groups were observed; one with a high inflammatory signature (Group 1) and one with a low inflammatory signature (Group 2)(**Figure 10d-e**). Group 1 samples had high expression of chemokines including CCL2, CCL5, CCL18, CCL21, and CXCL11. Markers of an activated immune response and complement system were also highly expressed including IFNG, IFNA17, IL1A, PRF1 (Perforin), HLA-DRB3 (MHC-II), MSR1, ITGAM (CD11b), C6, and C9. Group 2 samples had unremarkable expression of genes involved in the immune response, especially those associated with chemokines, cytokines, adhesion molecules, Cancer/testis antigens, and macrophage functions.

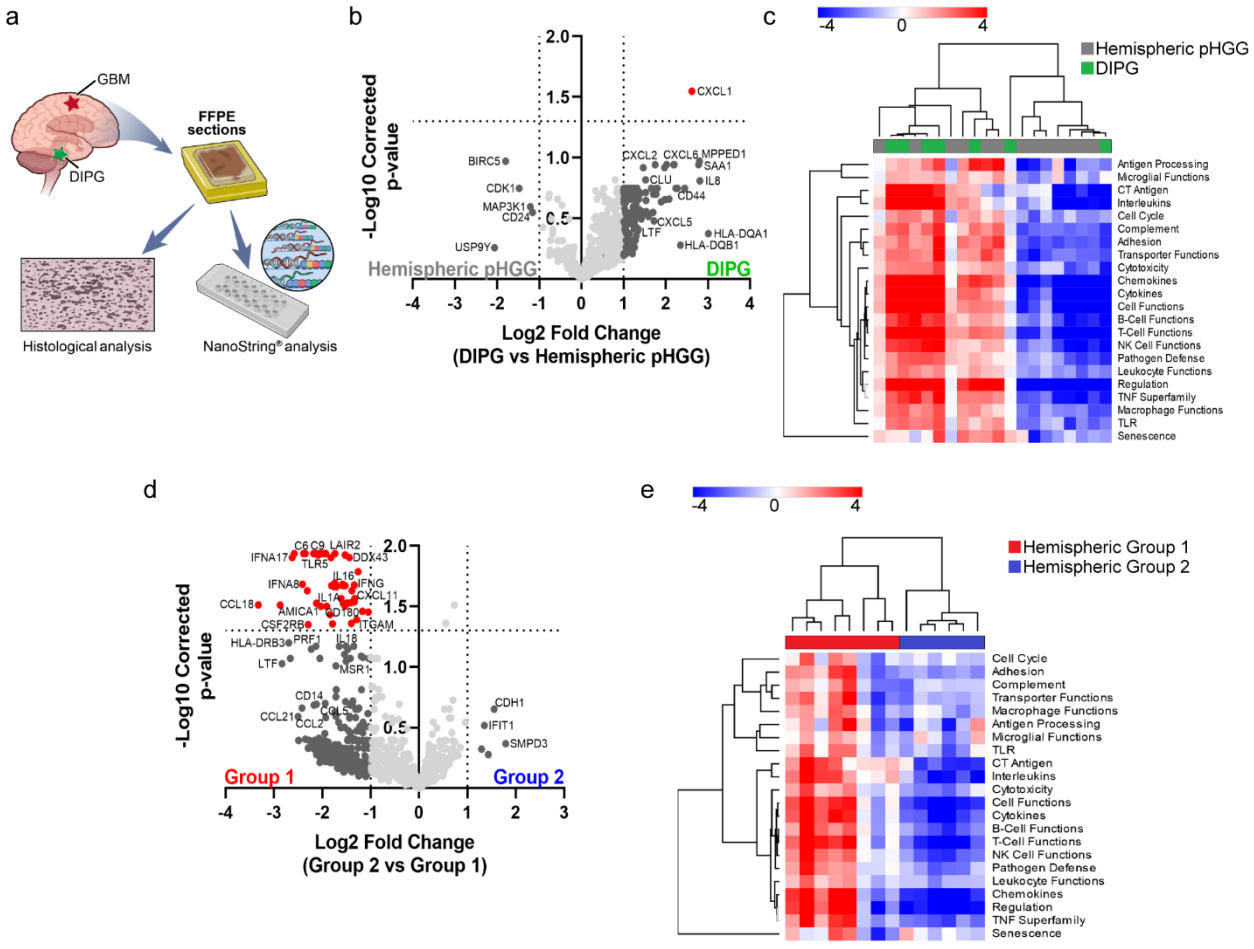

Figure 10: Immune Profiling of Human pHGGs. (a) Formalin fixed paraffin embedded human hemispheric pHGGs or DIPG tumor samples were utilized for NanoString mRNA analysis and histological characterization. **(b)** Volcano plot demonstrating differential gene expression between hemispheric pHGG samples and DIPG samples. Vertical dashed line represents fold change greater than 2. Horizontal dashed line represents Benjamin Hochberg corrected p-value of <0.05. **(c)** Unsupervised hierarchical clustering of human pHGG samples based on their pathway scores obtained from NanoString analysis. n=20 samples. **(d)** Volcano plot demonstrating differential gene expression between hemispheric samples. **(e)** Unsupervised hierarchical clustering of hemispheric samples based on their pathway scores.

Neuropathological Characterization of Human pHGGs

Using a larger cohort of human pHGG tumor samples, we also performed histological analyses of the infiltrating immune cell types to determine their relative presence among these samples. CD3 and CD8 T-cell staining corroborated previous findings of sparse T-cell infiltrates in these tumors **(Figure 11a-b**). There were no differences when comparing hemispheric to brainstem tumors, which may be due to low sample sizes. Because there were limited numbers of infiltrating lymphocytes in these tumors we then stained for infiltrating TAMs using the pan-macrophage marker IBA1. Unlike T-cell staining, there was considerable sample to sample variability with some samples possessing low and others with high $IBA1^+$ TAM infiltration. These TAMs include infiltrating BMDMs and brain-resident microglia, however a distinction between the two cannot be made due to a lack of distinct cell-type specific histological markers. There was no difference when comparing cortical GBM samples to brainstem DIPG samples **(Figure 11c-d**). Staining for CD31, an endothelial cell marker, and PDGFRβ, a stromal cell marker, demonstrates these tumors are highly vascularized with abnormal networks of blood vessels **(Figure 11e-f**). Staining for the PDGFRβ ligand, PDGFB, also demonstrates variable staining from tumor to tumor **(Figure 11g**). Interestingly, CD31, PDGFRβ, and PDGFB all strongly correlate with IBA1 positivity **(Figure 11h-j**). Although there were few CD3+ T-cells in these tumors, there was still a positive correlation between CD3 and CD31 positivity as well as CD3 and PDGFRβ. Unlike staining for PDGFB, the majority of tissue samples did not positively stain for PDGFA (7 out of 33 samples). Taken together, these results indicate a possible role for PDGFRβ/PDGFB pathway involvement in the infiltration of IBA1 positive TAMs and other immune cell types in pHGG.

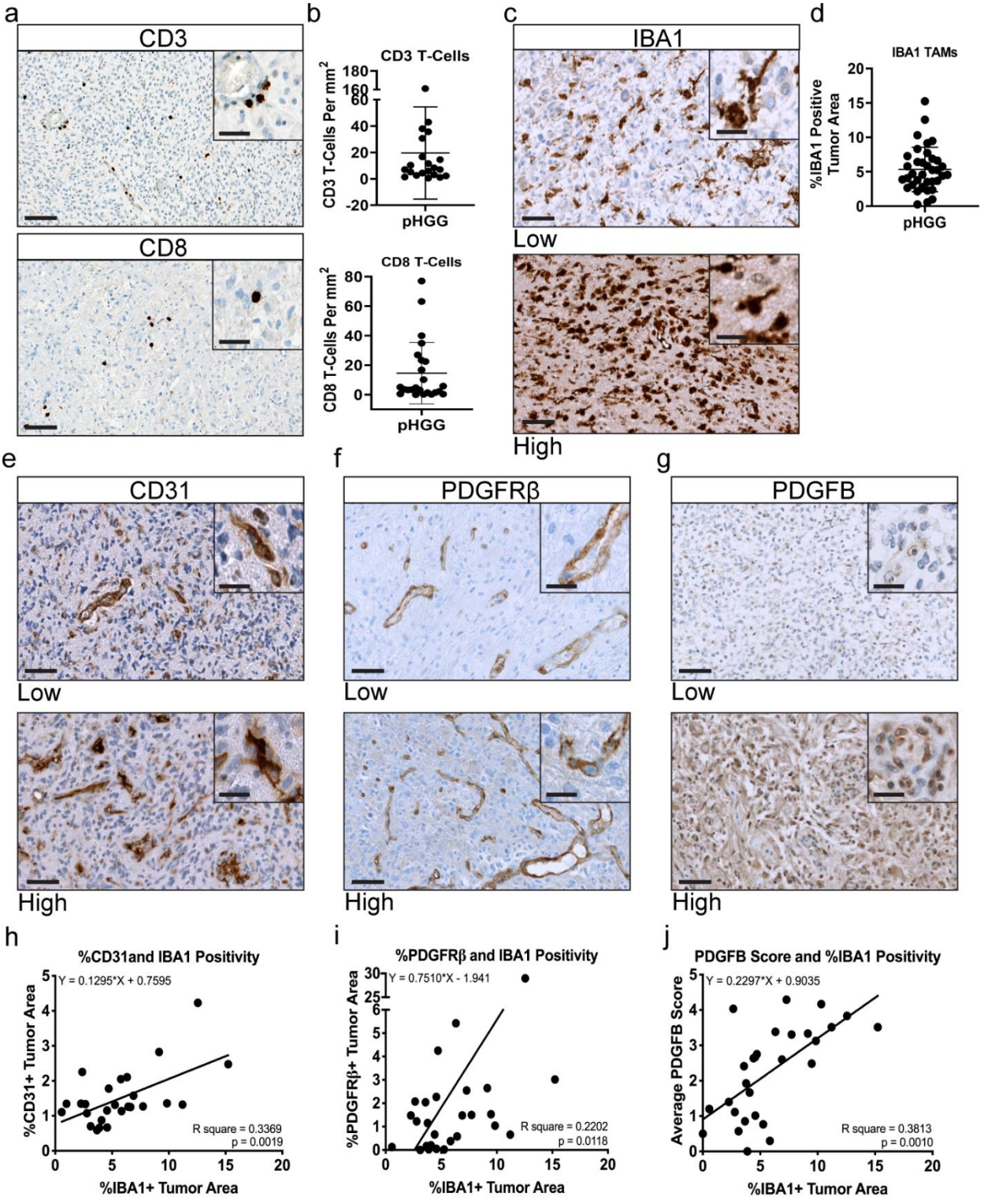
a
CD3
CD8
b
CD3 T-Cells
CD3 T-Cells Per mm2
pHGG
CD8 T-Cells
CD8 T-Cells Per mm2
pHGG
c
IBA1
Low
High
d
IBA1 TAMs
%IBA1 Positive Tumor Area
pHGG
e
CD31
Low
High
f
PDGFRβ
Low
High
g
PDGFB
Low
High
h
%CD31and IBA1 Positivity
Y = 0.1295*X + 0.7595
R square = 0.3369
p = 0.0019
%CD31+ Tumor Area
%IBA1+ Tumor Area
i
%PDGFRβ and IBA1 Positivity
Y = 0.7510*X - 1.941
R square = 0.2202
p = 0.0118
%PDGFRβ+ Tumor Area
%IBA1+ Tumor Area
j
PDGFB Score and %IBA1 Positivity
Y = 0.2297*X + 0.9035
R square = 0.3813
p = 0.0010
Average PDGFB Score
%IBA1+ Tumor Area

Figure 11: Neuropathological Characterization of Human pHGGs. Formalin fixed paraffin embedded human hemispheric pHGGs or DIPG tumor samples were stained for the following. **(a)** CD3 and CD8 T-cells. **(b)** Quantification of CD3 and CD8 positivity. **(c)** IBA1. Representative images for low and high staining samples are displayed. **(d)** Quantification of IBA1 positivity. **(e)** CD31. **(f)** PDGFRβ**. (g)** PDGFB. **(h)** Linear regression correlation of CD31 positive tumor area with IBA1 positive tumor area for matched samples. **(i)** Correlation of PDGFRβ positive tumor area with IBA1 positive tumor area for matched samples. **(j)** Correlation of PDGFB score with IBA1 positive tumor area for matched samples. All images are at 40x magnification with 80x inserts and scale bars are 100μm and 20μm respectively.

Methods

NanoString Analysis

Human FFPE tissue scrolls were cut in 10μm sections for RNA extraction. RNA integrity was confirmed using a bioanalyzer and samples possessing a DV300% greater than 30 were used. 50ng of RNA was used for NanoString analysis with the pan cancer pathways immune panel (NanoString, XT-CSO-HIP1-12). All data analysis was processed and normalized using nSolver Analysis Software version 4.0 and GraphPad Prism 8 (GraphPad Software, San Diego, CA). For more patient information, please see Table 1 on page 97.

Immunohistochemical Staining

All human tissue samples used in this study were Emory University IRB approved and de-identified. Paraffin embedded tissue samples were sectioned at 5μm per slide and mounted. Samples were then stained on a Discovery XT Platform (Ventana Medical Systems, USA) with; IBA1 (Wako 019-19741, 1:500), PDGFA (sc-128, 1:200), PDGFB (sc-127, 1:200), PDGFRα (cs3174, 1:300), PDGFRβ (cs3169, 1:300), CD31 (Dako m0823, 1:50), SMA (Dako M0851, 1:200), CD3 (Dako A0452, 1:100), and CD8 (Dako M7103, 1:100).

Image Analysis

Stained samples were scanned at 20x and converted to digital images using a Nanozoomer 2.0HT whole slide scanner (Hamamatsu Photonic K.K., Hamamatsu, Japan). For each staining and sample, total tumor area was calculated to determine the number of representative images needed to accurately represent intra-tumor heterogeneity. The tumor was then divided into sub-regions and the number of images acquired for analysis was standardized to the relative size of the sub-region in comparison to total tumor. For IBA1, PDGFRα, and PDGFRβ staining, the percentage of positively stained tumor area was calculated. For PDGFB,

three independent reviewers assigned a relative score of 0 (low) – 5 (high) to each image and the average scores were calculated. For phospho-histone 3, the number of positively stained nuclei per mm^2 was quantified. All image analysis was performed using ImageJ Fiji.

Chapter 4

Mouse Modeling of PDGF-Driven HGGs

Among many hindering factors in studying pHGG is the difficulty of obtaining primary untreated tumor samples. This makes it difficult when performing correlative and mechanistic studies as there exists many uncontrollable confounding factors including the type of treatment received, tumor mutational landscape, and quality of resected tissue. In order to study the inflammatory microenvironment of these tumors and the factors promoting macrophage infiltration, we utilized the RCAS-Tva system to induce HGGs in immunocompetent newborn pups. For our studies, we induced cortical HGGs in either *Ntva;Cdkn2a*$^{-/-}$ or *Ntva;Cdkn2a*$^{wt/wt}$ mice aged 0-2 days old. *Ntva;Cdkn2a*$^{-/-}$ mice received a single injection of DF1 cells producing either human *PDGFA* or human *PDGFB. Ntva;Cdkn2a*$^{wt/wt}$ mice received a co-injection of DF1 cells consisting of RCAS-shP53 along with either RCAS-PDGFA or RCAS-PDGFB (**Figure 12a**). Freshly dissociated tumor tissue from these models was verified using qPCR for *PDGFA* and *PDGFB* (**Figure 12b**). PDGFA-driven tumors produced a mix of grade III (32%) and grade IV (68%) tumors, as graded by a neuropathologist. PDGFB-driven tumors were all grade IV (96%) with the exception of one grade III tumor (4%) (**Figure 12c**). These tumors displayed all major histological hallmarks of HGG including microvascular hyperplasia and pseudopalisading necrosis as demonstrated by H&E staining (**Figure 12d**).

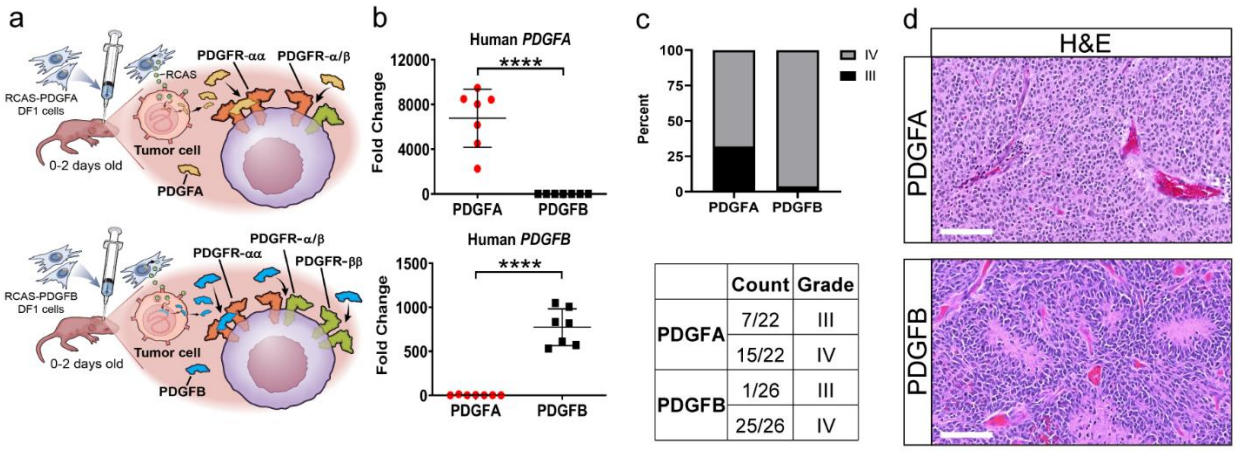

	Count	Grade
PDGFA	7/22	III
	15/22	IV
PDGFB	1/26	III
	25/26	IV

Figure 12: Mouse Modeling of PDGF-Driven HGGs. (a) Schematic depicting the injection of newborn pups with RCAS-PDGFA or RCAS-PDGFB. Ligand-receptor binding interactions for PDGFA and PDGFB are highlighted. **(b)** qPCR validation for human *PDGFA* or *PDGFB* in their respective tumors. **(c)** Tumor grading performed by a neuropathologist on samples generated in *Cdkn2a*$^{-/-}$ mice driven by either PDGFA (n=22) or PDGFB (n=26). **(d)** Representative H&E images of PDGFA and PDGFB-driven tumors depicting the major histological hallmarks of a high-grade glioma. Scale bar=100μm.

Staining for PDGFRα in each tumor type displayed the presence of the receptor on all tumor cells and no differences in expression of this protein was observed between them (**Figure 13a,c**). Conversely, PDGFB-driven tumors had greater tumor area covered by PDGFRβ (**Figure 13b,d**) and the pericyte marker smooth muscle actin (SMA) (**Figure 13e,g**). Similar to our findings in human pHGG samples, PDGFRβ positively correlated with IBA1 staining, suggesting the infiltration of TAMs is in part mediated through PDGF-induced signaling. Staining for CD31 demonstrated no significant difference in the amount of tumor area covered by blood vessels, however, PDGFA-driven tumors had smaller and more numerous blood vessels compared to PDGFB-driven tumors (**Figure 13f,h-i**). Interestingly, PDGFB-driven tumors in *Ntva;Cdkn2a*$^{-/-}$ mice had a significantly decreased survival of 28 days compared to PDGFA-driven tumors whose median survival was 49 days (**Figure 13j**). Taken together, PDGFB-driven tumors are more frequently histologically classified as Grade IV compared to PDGFA-driven tumors which tend to be a mix of Grade III and Grade IV tumors. This difference is likely not due to the expression of PDGFRα as it is homogenously expressed throughout both tumors equally. However, PDGFB-driven tumors have more irregular vasculature as shown by enlarged CD31 positive blood vessels and the increased presence of PDGFRβ positive stromal cells and SMA positive pericytes. These tumors also have a significantly decreased median survival, therefore implicating PDGFB as an important mediator of tumor progression and malignancy.

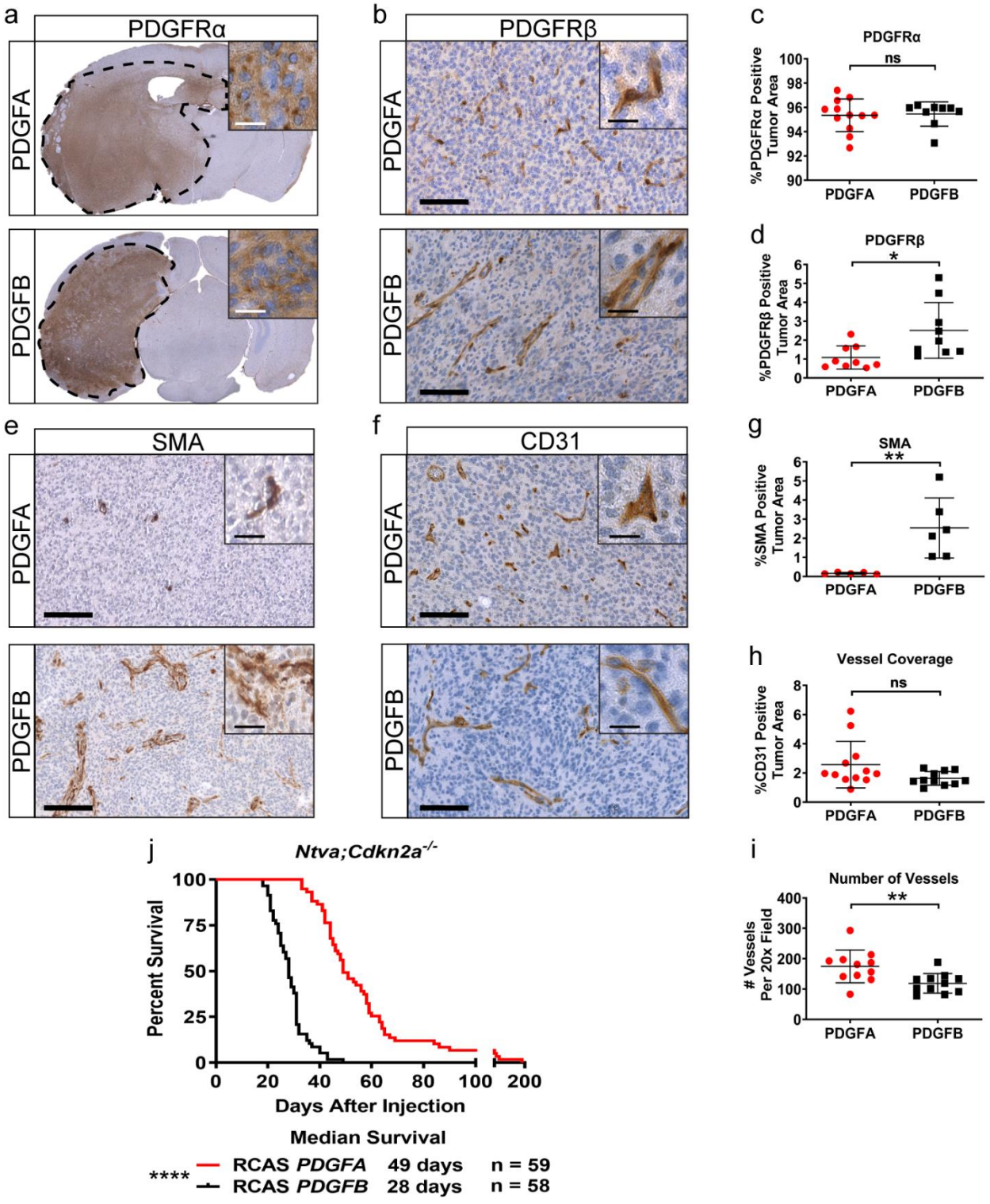
a
PDGFRα
PDGFA
PDGFB
b
PDGFRβ
PDGFA
PDGFB
c
PDGFRα
ns
%PDGFRα Positive Tumor Area
100
98
96
94
92
90
PDGFA
PDGFB
d
PDGFRβ
*
%PDGFRβ Positive Tumor Area
6
5
4
3
2
1
0
PDGFA
PDGFB
e
SMA
PDGFA
PDGFB
f
CD31
PDGFA
PDGFB
g
SMA
**
%SMA Positive Tumor Area
6
5
4
3
2
1
0
PDGFA
PDGFB
h
Vessel Coverage
ns
%CD31 Positive Tumor Area
8
6
4
2
0
PDGFA
PDGFB
i
Number of Vessels
**
Vessels Per 20x Field
400
300
200
100
0
PDGFA
PDGFB
j
Ntva;Cdkn2a-/-
Percent Survival
100
75
50
25
0
0
20
40
60
80
100
200
Days After Injection
Median Survival
**** RCAS PDGFA 49 days n = 59
RCAS PDGFB 28 days n = 58

Figure 13: Murine pHGG Model Characterization. (a) Whole brain PDGFRα staining in *Ntva;Cdkn2a*$^{-/-}$ PDGFA and PDGFB-driven tumors. **(b)** Representative PDGFRβ staining. **(c)** Quantification of PDGFRα staining. **(d)** Quantification of PDGFRβ staining. **(e)** Representative SMA staining. **(f)** Representative CD31 staining. **(g)** Quantification of SMA positive tumor area. **(h)** Quantification of vessel coverage as indicated by CD31 staining. **(f)** Quantification of the number of blood vessels detected by CD31 staining. **(g)** Survival curves of *Ntva;Cdkn2a*$^{-/-}$ mice with tumors driven by RCAS. All representative images (b, e, f) are 20x with 80x magnified insets, scale bar=20μm and 100μm respectively.

Inflammatory Microenvironment of PDGF-Driven Mouse HGGs

To complement our NanoString analysis of human pHGGs, we also performed NanoString on PDGFA and PDGFB-driven tumors generated in *Cdkn2a*$^{-/-}$ mice. Strong separation between the two tumor types was readily observed when unsupervised hierarchical clustering on all 750 genes was performed (**Figure 14a**). There were 40 statistically significant DE genes after p-value correction and top DE genes were validated with qPCR (**Figure 14b-f**). PDGFB tumors possessed high expression of chemokines including *Ccl11, Cxcl13,* and *Ccl12.* PDGFB tumors also had significantly higher expression of inflammatory adhesion molecules *Cd11b, Cd74,* and *Selplg* (CD162), all of which play important roles in promoting and mediating leukocyte and macrophage trafficking. Genes involved in antigen processing and presentation were also highly expressed in PDGFB tumors including *Ly86, Cd180, H2-K1,* and *H2-Eb1* (MHC-II). The high expression of these genes suggests PDGFB promotes an inflammatory environment which encourages macrophage and leukocyte infiltration. Conversely, PDGFA tumors had high expression of *Cfh* (Complement Factor H) which is an inhibitor of inflammation triggered by the complement system (142). These tumors also had high expression of *Cybb*, a component of NADPH oxidase which helps phagocytic cells clear pathogens. Other highly expressed genes in PDGFA-driven tumors include *Ifitm1, Rsad2, Cd36,* and *Il16* which are all important mediators of the innate immune response to foreign pathogens. These results suggest PDGFA-driven tumors still express inflammatory genes, however the genes expressed may represent more functional components of the immune response which help promote extended survival.

Pathway analysis demonstrated exclusive clustering between PDGFA and PDGFB-driven tumors. PDGFB-driven tumors demonstrably had greater representation of genes involved in

inflammatory processes including the complement pathway, leukocyte functions, CD molecules, macrophage functions, innate immune response, chemokines, and cytokines and receptors (**Figure 14g**). Interestingly, at tumor endpoint, cell cycle function and basic cell function pathways were not significantly DE between the two entities. Immunohistochemical staining for phospho-histone 3, qPCR for *Ccnd2*, and *in vitro* cell proliferation assays all confirmed these findings, demonstrating no major differences in proliferation between the two tumor types at the end point of survival (**Figure 14h-j**). These results suggest the differences in tumor malignancy may likely be derived from the TME and not necessarily tumor cell intrinsic factors. Although these PDGF ligands operate through the same pathways, it is clear PDGFB is a much more potent inducer of the inflammatory response, which results in significantly shorter survival time compared to PDGFA-driven tumors.

Next, to validate our NanoString findings, we performed IBA1 staining in FFPE tumor sections from PDGFA and PDGFB-driven tumors in *Ntva;Cdkn2a*$^{-/-}$ mice. There was a dramatic increase in the number of infiltrating TAMs observed in PDGFB tumors as shown by whole brain staining (**Figure 15a-b**). TAMs were found throughout the entirety of both tumor types, however, PDGFB samples had twice as much tumor area covered by the TAMs. Much like our findings in human pHGGs, PDGFB appears to be promoting a pro-inflammatory microenvironment. The identity of the infiltrating TAM subtypes remains unknown, as well as the behavior of these cell types as they interact with the TME.

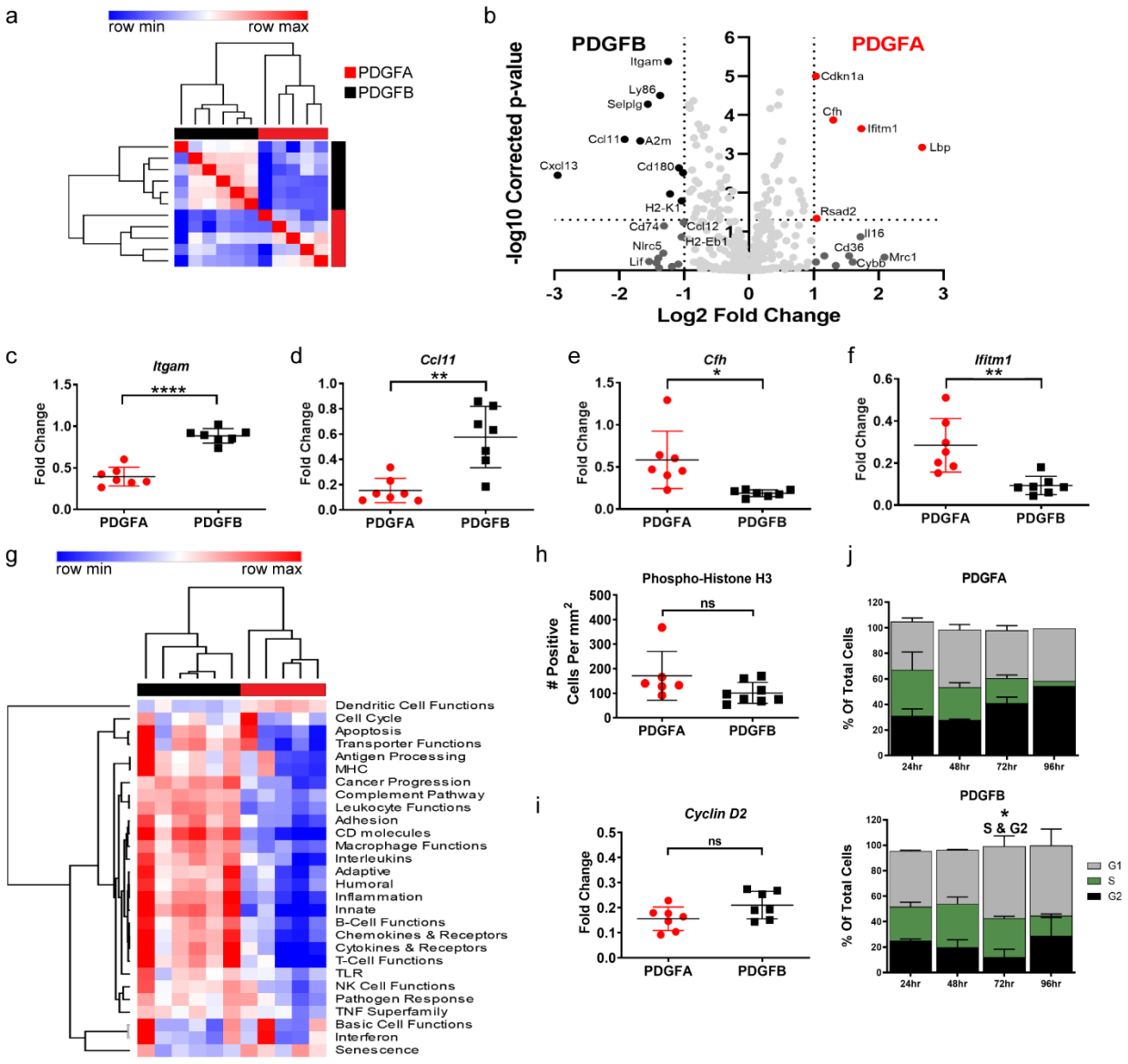

Figure 14: Inflammatory Microenvironment of PDGF-Driven Murine HGGs. (a) Similarity matrix performed on PDGFA (n=5) and PDGFB (n=6) tumor samples based on the expression of 750 genes detected using NanoString. **(b)** Volcano plot of differentially expressed genes detected using NanoString on PDGFA and PDGFB-driven tumors. **(c-f)** qPCR validation of top differentially expressed genes found in NanoString analysis. **(g)** Unsupervised hierarchical clustering of PDGFA and PDGFB tumor samples based on their pathway scores obtained from NanoString. **(h)** Quantification of phospho-histone H3 staining in PDGFA and PDGFB tumor

samples. **(i)** qPCR for *Cyclin D2* in PDGFA and PDGFB tumor samples. **(j)** Edu proliferation assay results for PDGFA primary cell lines (n=3) and PDGB primary cell lines (n=2) at 24hr, 48hr, 72hr, and 96hrs.

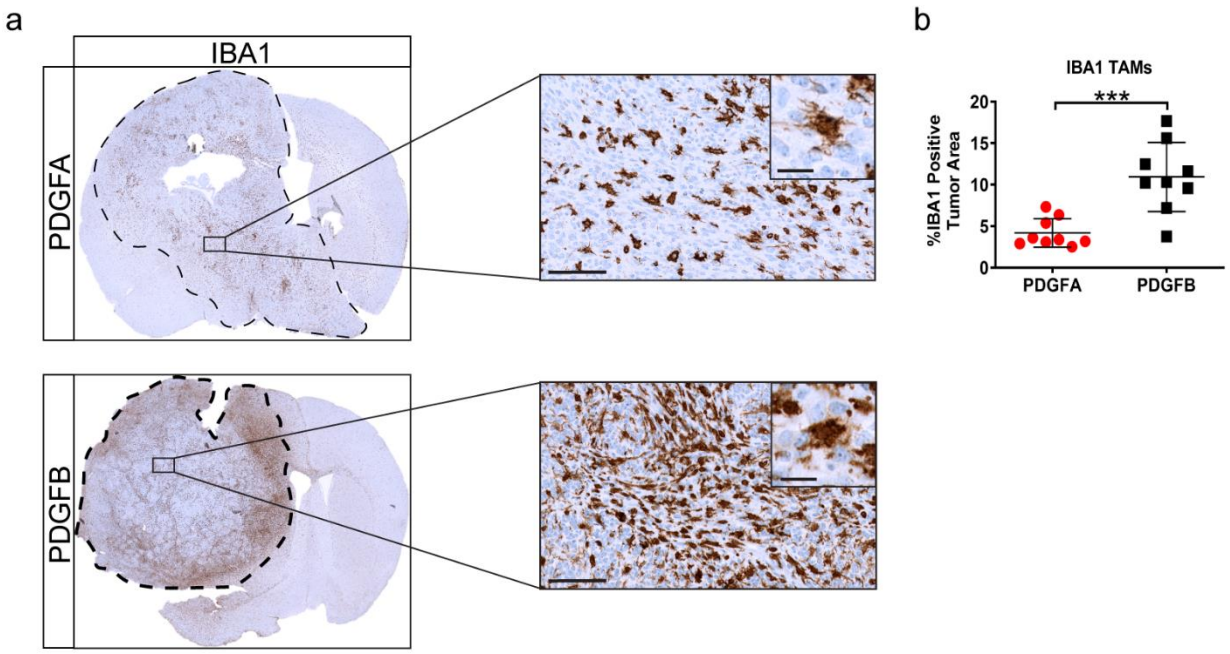

Figure 15. IBA1 TAM Infiltration in PDGF-Driven Murine HGGs. (a) IBA1 staining on PDGFA and PDGFB tumors generated in *Ntva;Cdkn2a*$^{-/-}$ mice. 40x and 80x magnified images, scale bars 100μm and 20μm respectively. Tumors are outlined in black dashed line. **(b)** Quantification of IBA1 staining. PDGFA n=9, PDGFB n=9. Students *t*-test, ***p<0.001.

Flow Cytometry of PDGF-Driven Murine HGGs

Since IBA1 is a pan-macrophage marker staining both peripheral BMDMs and microglia, it is unclear what the identity is of the additional TAMs found in PDGFB-driven tumors. Are these TAMs coming from the blood or from the surrounding brain tissue? To answer this important question, we induced tumors in *Ntva;Cdkn2a*$^{wt/wt}$ mice with a co-injection of RCAS-shp53-RFP along with either RCAS-PDGFA or RCAS-PDGFB. These mice are in a pure CL57BL/6 background and are more suitable for lineage identification as compared to *Ntva;Cdkn2a*$^{-/-}$ mice which are in a mixed background. *Cdkn2a* deletions and *p53* mutations are both frequently found in human pHGGs, therefore these models positively recapitulate the human genetics in a controlled manner. As seen in the *Ntva;Cdkn2a*$^{-/-}$ mice, PDGFB-driven tumors in the *Ntva;Cdkn2a*$^{wt/wt}$ mice had a significantly decreased median survival (35 days) compared to PDGFA-driven tumors (57 days) (**Figure 16a**).

Freshly dissociated tumor tissue stained for CD45, CD11b, Ly6C, and Ly6G demonstrated PDGFB tumors had a significant increase in the lymphocyte population ($CD45^{+}CD11b^{-}$) and in the total TAM population ($CD45^{+}CD11b^{+}$) compared to PDGFA-driven tumors (**Figure 16b-c**). Based on CD45 and CD11b staining intensity, the two TAM populations can be separated into infiltrating BMDMs ($CD45^{hi}CD11b^{hi}$) and microglia ($CD45^{lo}CD11b^{hi}$). The increase in the total TAM population was not due to the number of microglia, but rather due to the infiltrating BMDM population. Further staining for Ly6C and Ly6G demonstrated the increased BMDM population was from the number of inflammatory monocytes ($Ly6C^{hi}Ly6G^{-}$) while there was no difference in neutrophils (**Figure 16d-h**). These results indicate PDGFB promotes the infiltration of circulating monocytes from the blood into the brain. Whether this effect is directly through PDGF ligand chemoattraction, BBB permeability, or through

downstream PDGF-signaling events remains unknown. We believe these effects are likely due to a combination of all three of these factors, however we focused the remainder of our efforts on chemokine signaling as the likely driver of TAM infiltration.

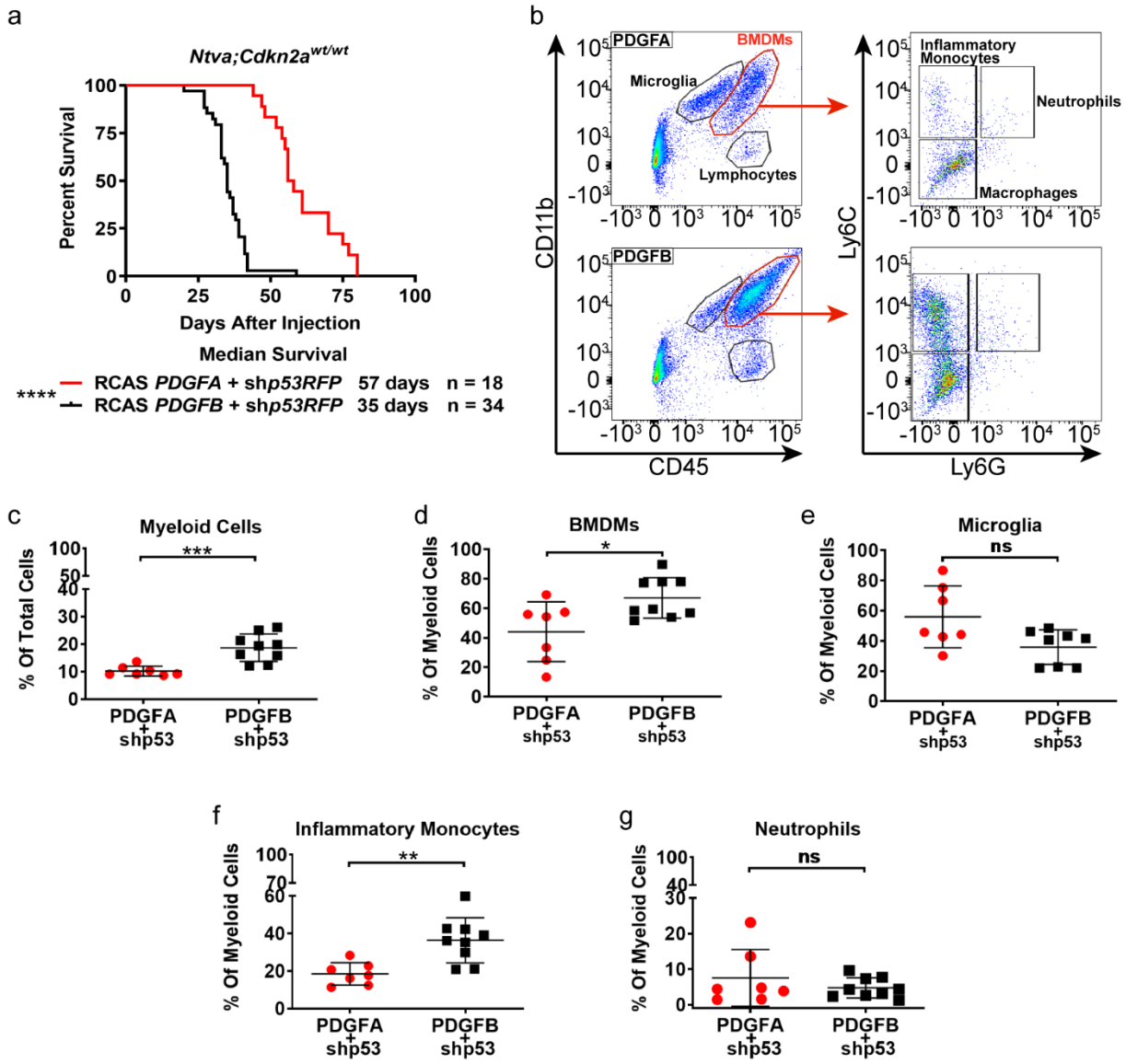

Figure 16: Flow Cytometry of PDGF-Driven Murine HGGs. (a) Survival curves for *Ntva;Cdkn2a*$^{wt/wt}$ mice with tumors induced by RCAS-PDGFA or RCAS-PDGFB with co-administration of RCAS-shP53. Log-rank Mantel-Cox test performed for survival curves. **(b)** Representative flow cytometry dot plots of PDGFA (n=7) and PDGFB-driven (n=9) tumors generated in *Ntva;Cdkn2a*$^{wt/wt}$ mice, gated for CD45, CD11b, Ly6C, and Ly6G. **(c)** %CD45^{+}CD11b^{+} myeloid cells in the total tumor cell population. **(d)** %CD45^{hi}CD11b^{+} BMDMs in the total myeloid cell population. **(e)** %CD45^{lo}CD11b^{+} microglia in the total myeloid cell

population. **(f)** %$CD45^{hi}CD11b^{+}Ly6C^{hi}Ly6G^{lo}$ inflammatory monocytes in the total BMDM population. **(g)** %$CD45^{hi}CD11b^{+}Ly6C^{hi}Ly6G^{hi}$ neutrophils in the total BMDM population. Students *t*-test, *p<0.05, **p<0.01, ***p<0.001, ****p<0.0001.

qPCR Molecular Characterization of PDGF-Driven HGGs

NanoString analysis provided us with a deep understanding of the representative pathways involved in PDGF-driven tumors. It demonstrated PDGFB-driven tumors are more inflammatory, however we wanted to confirm these findings. Therefore, we used a qPCR panel of over 70 genes including chemokines and chemokine receptors, immune markers, macrophage markers, and cancer signaling markers. As found in our NanoString dataset, when clustering these tumors based on their expression profiles, PDGFA-driven tumors distinctly cluster apart from PDGFB-driven tumors (**Figure 17a**). As expected, PDGFB-driven tumors had greater expression of *Aif1* (IBA1) and *Itgam1* (Cd11). Further analysis revealed PDGFB tumors had greater expression of chemokines including *Ccl2, Ccl7,* and *Ccl11*. *Ccr5* and *Csf1r* were also higher in PDGFB samples (**Figure 17b**). Immunosuppressive genes including *Pd1* (PD1), *Pdcd1lg2* (PD-L2), and *Ctla4* were all highly expressed in PDGFB tumors suggesting these tumors have a greater immunosuppressive phenotype compared to PDGFA tumors. There were only a few genes more highly expressed in PDGFA-driven tumors not previously examined in the NanoString analysis. *Marco*, a scavenger receptor, and the chemokine receptor *Ccr1* were highly expressed in PDGFA tumor samples as well (**Figure 17c-d**).

To validate qPCR findings on the protein level, a cytokine array was also run using three pooled samples from each tumor type. As observed on the mRNA level, CCL2, CCL3, and CCL12 were all expressed at higher levels in PDGFB-driven tumors compared to PDGFA-driven tumors (**Figure 17e-f**). For further validation, protein ELISA was run on individual tumor samples for CCL2, CCL3, CCL7, CCL8, and CCL12. Interestingly, the only significant difference in protein expression was for CCL7, which was higher in PDGFB tumor samples (**Figure 17g**). Although other chemokines were not significantly higher, there was still a general

positive trend towards higher expression in PDGFB-driven tumor samples. Increasing the sample sizes might increase the significance of these findings.

The importance of chemokine signaling in glioma progression is increasingly being studied by our lab. We have previously demonstrated in adult murine GBM that increased *Ccl2* expression is associated with increased monocyte infiltration. Further, we have shown that heterozygous *Ccl2* knockout mice have decreased TAM infiltration and increased survival, yet this effect was not observed in homozygous *Ccl2* knockout mice (95). CCL2 binds to the CCR2 receptor with high affinity, and to a lesser extent CCR4 (143). These receptors, and other chemokine receptors, are expressed by myeloid cell and T-cell populations (143). As the production of chemokines in the TME increase, it is expected the population of infiltrating immune cells will also increase. These mRNA and protein data suggest PDGFB promotes an inflammatory microenvironment that produces chemoattractant signals for macrophage recruitment and other signals that may drive the suppression of immune function.

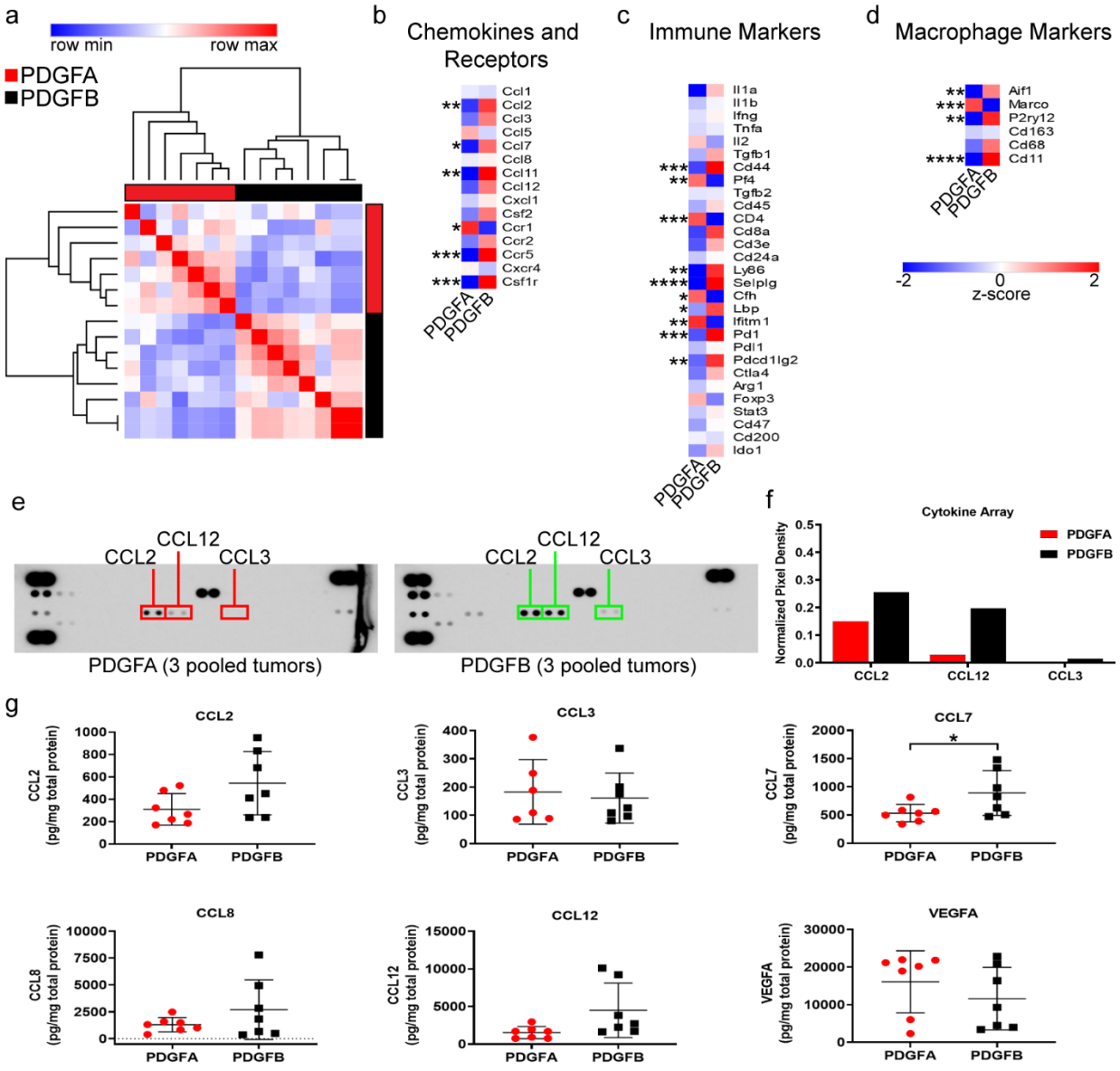

Figure 17: Molecular and Proteomic Characterization of PDGF-Driven Murine HGGs. (a) Similarity matrix of PDGFA (n=7) and PDGFB-driven (n=7) tumors generated in *Cdkn2a*$^{-/-}$ mice. Samples are clustered by their expression of 72 genes detected by qPCR. **(b)** Averaged z-scores for PDGFA and PDGFB-driven tumor samples based on their expression of chemokines and chemokine receptor genes. **(c)** Averaged z-scores for PDGFA and PDGFB-driven tumor samples based on their expression of immune-related genes. **(d)** Averaged z-scores for PDGFA and PDGFB-driven tumor samples based on their expression of macrophage related genes. **(e)**

Cytokine array of 3 pooled PDGFA tumor samples and 3 pooled PDGFB tumor samples. CCL2, CCL3, and CCL12 are all highlighted. **(f)** Quantification of pixel intensity for CCL2, CCL3, and CCL12 from the cytokine array. **(g)** Protein ELISA performed on PDGFA (n=7) and PDGFB (n=7) tumor samples for CCL2, CCL3, CCL7, CCL8, CCL12, and VEGFA**.** Students *t*-test. *p<0.05, **p<0.01, ***p<0.001, and ****p<0.0001.

In vitro Stimulation of BMDMs and Microglia with PDGF Ligands

It is evident PDGFB-driven tumors have shorter median survival and greater macrophage infiltration compared to PDGFA-driven tumors. However, what these macrophages are doing once they are inside the tumor remains unclear. To answer this question, BMDMs were isolated from naïve CL57BL/6 adult mice and cultured in the presence of M-CSF to drive them towards a macrophage phenotype. After 7 days, cells were stimulated with increasing doses of either recombinant PDGFA or PDGFB protein (0-100ng/mL) for 6 hours. After stimulation, RNA was collected for qPCR and supernatant collected for protein ELISA. qPCR for the chemokines *Ccl2, Ccl7, Ccl12,* and *Vegf* demonstrated in response to increasing doses of PDGFB but not PDGFA, BMDMs upregulate their expression of these genes (**Figure 18a-g**). Interestingly, when the same experimental conditions and stimulations were performed using cultured microglia from newborn CL57BL/6 pups these responses were not observed (**Figure 18h-n**). Additionally, in response to PDGFB stimulation, BMDMs also produced higher levels of *Arg1*, an enzyme which suppresses T-cell function in the TME. The only gene stimulated in microglia was in response to PDGFA stimulation, which was *Il1b*. IL1β is a potent inducer of inflammation produced by macrophages and are of key interest to our lab in adult GBM studies.

PDGFB may exert its pro-inflammatory effects through infiltrating BMDMs. These cells are attracted to the tumor site via chemokine mediated fashion where they then respond to tumor-derived signals by producing their own chemoattractant molecules and immunosuppressive factors. The production of these signals then attracts more BMDMs to the TME, thus creating an aggressive feed forward loop. Whether PDGFB itself is attracting the BMDMs to the TME is not yet known, however it has been demonstrated PDGFD, which exclusively activates PDGFRβ, is

a chemoattractant and activator for natural killer cells, indicating PDGFRβ activity may be an important mediator in these processes (144).

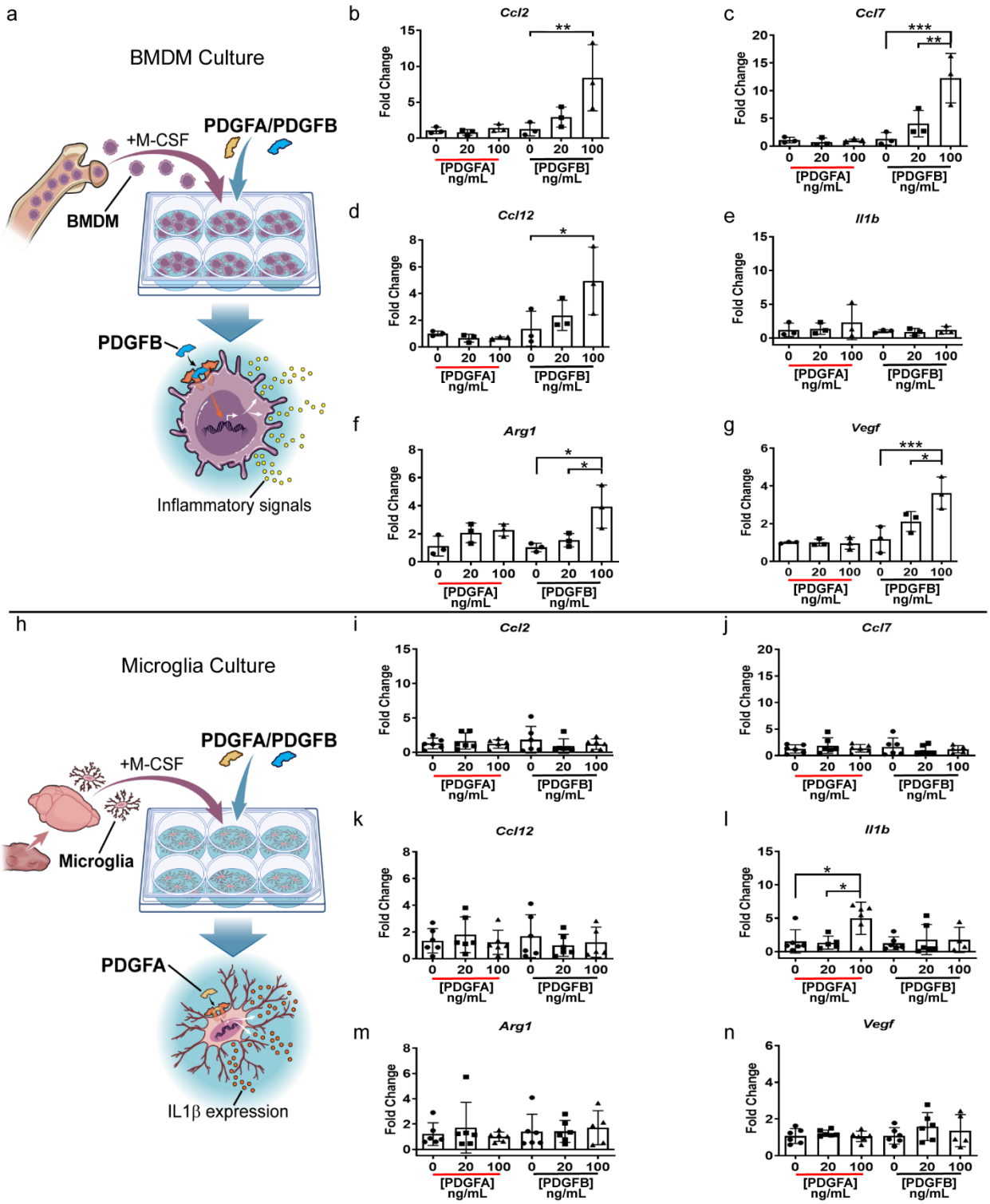
a
BMDM Culture
+M-CSF
PDGFA/PDGFB
BMDM
PDGFB
Inflammatory signals
b
Ccl2
c
Ccl7
d
Ccl12
e
Il1b
f
Arg1
g
Vegf
h
Microglia Culture
+M-CSF
PDGFA/PDGFB
Microglia
PDGFA
IL1β expression
i
Ccl2
j
Ccl7
k
Ccl12
l
Il1b
m
Arg1
n
Vegf
Fold Change
[PDGFA] ng/mL
[PDGFB] ng/mL

Figure 18: *In vitro* Stimulation of BMDMs and Microglia With PDGF Ligands. (a) Schematic depicting the isolation and culture of BMDMs from naïve CL57BL/6 mouse bone marrow. BMDMs were cultured with M-CSF and stimulated with either PDGFA or PDGFB for 6 hours prior to RNA isolation. **(b-g)** qPCR plots on BMDM samples stimulated with either PDGFA or PDGFB for 6 hours at 0ng/mL, 20ng/mL, or 100ng/mL. n=3 replicates per concentration. Genes detected were *Ccl2, Ccl7, Ccl12, IL1b, Arg1, and Vegf.* **(h)** Schematic depicting the isolation and culture of microglia from naïve newborn CL57BL/6 pup brains. Microglia were cultured with M-CSF and stimulated with either PDGFA or PDGFB for 6 hours prior to RNA isolation. **(i-n)** qPCR plots for *Ccl2, Ccl7, Ccl12, IL1b, Arg1, and Vegf.* n=5 replicates per concentration. One-way ANOVA with multiple comparisons. *$p<0.05$, **$p<0.01$, ***$p<0.001$.

Chemokine Knockout Mice Extend Survival in PDGF-Driven HGGs

It appears PDGFB is a driver of inflammation in human and murine pHGGs. In human samples with high IBA1+ staining, they also have high expression of PDGFRβ and PDGFB. We observe a high inflammatory profile in PDGFB-driven murine tumors, accompanied with an increase in TAM infiltration and a significant decrease in median survival. This data begs the question of whether we can inhibit TAM infiltration and whether this inhibition results in an extension of survival. To answer these questions, we used *Ntva* positive chemokine knockout mice and induced tumors with RCAS-shp53 and RCAS-PDGFA or RCAS-PDGFB. The chemokines we focused on were CCL2, CCL3, CCL7, and CCL8/12 as all of these were found to be highly expressed in PDGFB-driven tumors either through qPCR, ELISA, or cytokine array. Additionally, *in vitro* stimulation of BMDMs demonstrated PDGFB induces the expression of these chemokines. These chemokines are known monocyte chemoattractant proteins that are secreted by tumor cells and other cell types within the TME. They also help recruit other immune cell types including myeloid derived suppressor cells and T-reg cells which help promote immune escape and tumor progression (145-148).

Survival data indicate when PDGFB is the oncogenic driver, chemokine knockout of *Ccl2, Ccl7,* and *Ccl8/12* does not produce any survival benefit (**Figure 19a**). In fact, they surprisingly resulted in a decrease of median survival when compared to *Ntva* wild type mice. The only chemokine which produced an increase in survival was CCL3. These mice had a median survival of 49 days compared to 35 days in wild type mice. Unlike in PDGFB-driven tumors, there was an extension in survival in *Ccl8/12* knockout mice as well as in *Ccl3* knockout mice with tumors driven by PDGFA. The mice with the greatest survival benefit was *Ccl8/12* double knockout mice with a median survival of 73 days. Interestingly, homozygous deletion of

Ccl2 did not result in any survival difference from wild-type tumors driven by PDGFA. (**Figure 19b**).

Since CCL3 was the only chemokine to provide a survival benefit upon genetic deletion in PDGFB-driven tumors, flow cytometry was performed to determine if TAM infiltration was also inhibited. CD45 and CD11b staining indicated there was a reduction in the total TAM population (**Figure 19c**). This reduction was due to a decrease in the $CD45^{hi}CD11b^{hi}$ BMDM population (**Figure 19d**). The decrease in BMDMs subsequently caused an increase in the microglial population within the total TAM population (**Figure 19e**). Although there was not a striking reduction in BMDMs, complete or near complete ablation of TAM infiltration in single chemokine knockout mice is likely not feasible as there are many chemokines responsible for these processes.

RNA sequencing data of histone WT human pHGGs for chemokines revealed *CCL3* and *CCL4* cluster together, apart from all other chemokines (**Figure 19f**). Further, *CCL3* expression obtained from NanoString in human pHGG samples positively correlated with IBA1 positivity in matched samples (**Figure 19g**). Interestingly, CCL3 (Macrophage Inflammatory Protein 1-alpha) interacts with CCL4 (Macrophage Inflammatory Protein 1-beta) to bind to their shared receptor CCR5, and neither of these chemokines has been implicated in pHGG biology (149). CCL3 also binds to CCR1 and CCR4 to promote an inflammatory response characterized by neutrophil, monocyte, T-cell, B-cell, and dendritic cell chemoattraction (149-151). High levels of CCL3 and CCL4 have been found in sites where CD4+ T-cells interact with dendritic cells to promote CD8+ T-cell memory, indicating these chemokines play a wide range of roles in inflammatory processes (152). CCL3 has also been implicated in multiple sclerosis, a chronic CNS inflammatory disease characterized by demyelination of neurons and accumulation of plaques

containing microglia, macrophages, and other leukocytes (153, 154). Microglia and macrophages produce high levels of CCL2 and CCL3, and treatment of mice with experimental allergic encephalomyelitis (EAE) using antibodies against CCL3 prevented the infiltration of peripheral monocytes (155). Our results support these findings, and implicate CCL3 as an important driver of TAM recruitment and accumulation in pHGGs.

Eliminating CCL3 extended survival and slightly reduced TAM infiltration in PDGFB-driven tumors. However, the inhibitory effect on BMDM infiltration was not absolute and there was still a large population found in the tumors. These results indicate PDGFB is such a strong oncogenic driver it might be masking the effects of knocking out a single chemokine in these mice. Future studies should utilize PDGFA when trying to delineate single gene knockout differences rather than PDGFB. Additionally, these results suggest in order to greatly reduce or completely inhibit TAM infiltration, multiple strategies must be combined. As TAM infiltration is likely caused by both chemokine signaling and BBB permeability, one method which may be promising is combining anti-VEGF therapy with pharmacologic inhibition of chemokine signaling.

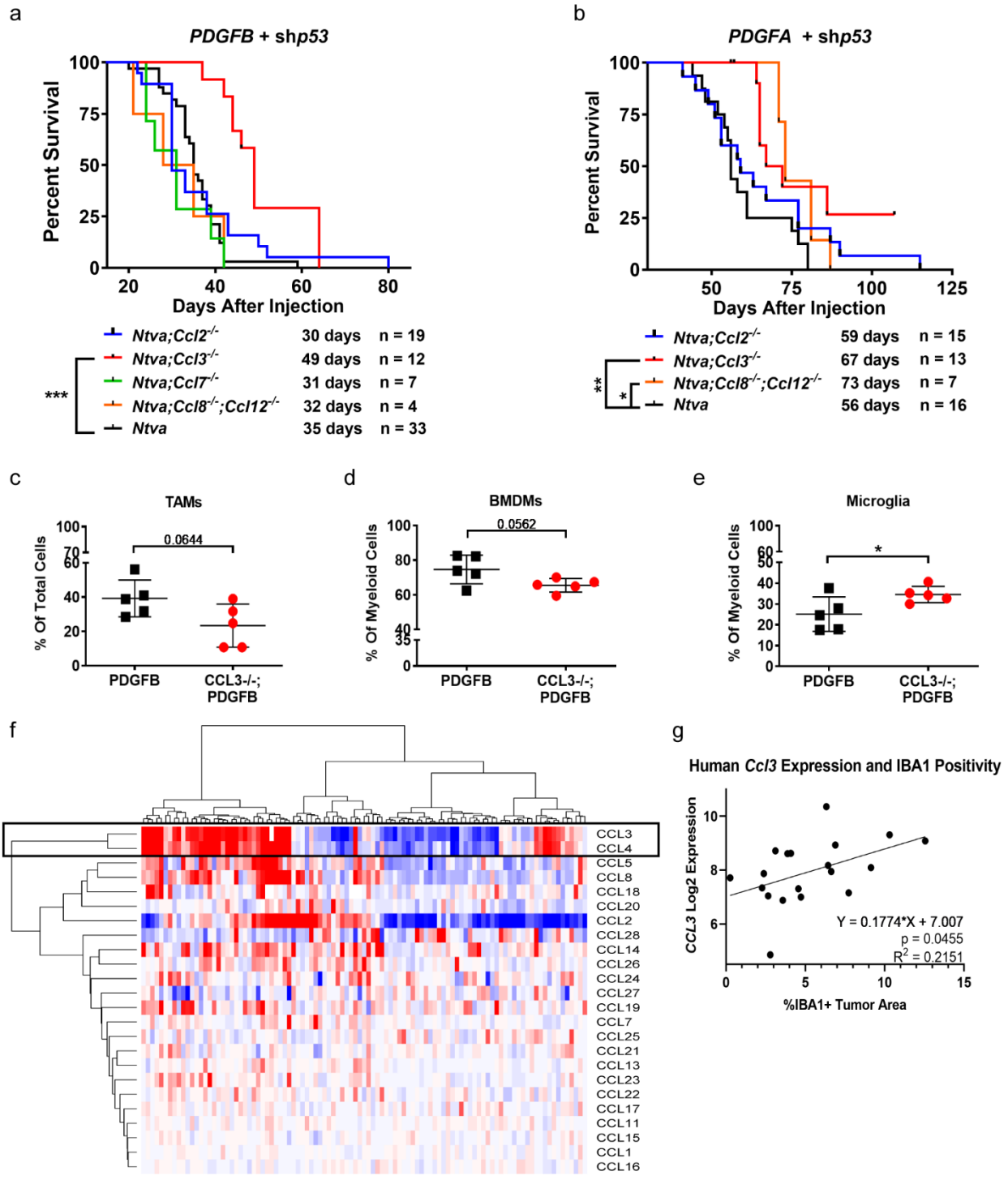
a
PDGFB + shp53
Percent Survival
Days After Injection
Ntva;Ccl2-/- 30 days n = 19
Ntva;Ccl3-/- 49 days n = 12
Ntva;Ccl7-/- 31 days n = 7
Ntva;Ccl8-/-;Ccl12-/- 32 days n = 4
Ntva 35 days n = 33
***
b
PDGFA + shp53
Percent Survival
Days After Injection
Ntva;Ccl2-/- 59 days n = 15
Ntva;Ccl3-/- 67 days n = 13
Ntva;Ccl8-/-;Ccl12-/- 73 days n = 7
Ntva 56 days n = 16
**
*
c
TAMs
% Of Total Cells
0.0644
PDGFB
CCL3-/-; PDGFB
d
BMDMs
% Of Myeloid Cells
0.0562
PDGFB
CCL3-/-; PDGFB
e
Microglia
% Of Myeloid Cells
*
PDGFB
CCL3-/-; PDGFB
f
CCL3
CCL4
CCL5
CCL8
CCL18
CCL20
CCL2
CCL28
CCL14
CCL26
CCL24
CCL27
CCL19
CCL7
CCL25
CCL21
CCL13
CCL23
CCL22
CCL17
CCL11
CCL15
CCL1
CCL16
g
Human Ccl3 Expression and IBA1 Positivity
CCL3 Log2 Expression
Y = 0.1774*X + 7.007
p = 0.0455
R2 = 0.2151
%IBA1+ Tumor Area

Figure 19: Chemokine Knockout Mice Exhibit Prolonged Survival and Decreased TAM Infiltration. (a) Survival curves of RCAS-PDGFB + RCAS-shP53 driven tumors in *Ntva;Ccl2*$^{-/-}$, *Ntva;Ccl3*$^{-/-}$, *Ntva;Ccl7*$^{-/-}$, *Ntva;Ccl8/12*$^{-/-}$, and *Ntva* mice. **(b)** Survival curves of RCAS-PDGFA + RCAS-shP53 driven tumors in *Ntva;Ccl2*$^{-/-}$, *Ntva;Ccl3*$^{-/-}$, *Ntva;Ccl8/12*$^{-/-}$, and *Ntva* mice. Log-rank Mantel-Cox test performed for survival curves. **(c)** %CD45+CD11b+ TAMs in the total tumor cell population in *Ntva* mice (n=5) or *Ntva;Ccl3*$^{-/-}$ mice (n=5) driven by RCAS-PDGFB and RCAS-shP53. **(d)** %CD45^{hi}CD11b+ BMDMs in the total myeloid cell population. **(e)** %CD45^{lo}CD11b+ microglia in the total myeloid cell population. **(f)** Unsupervised hierarchical clustering of chemokines in human pHGG RNA sequencing data. **(g)** *CCL3* expression in human pHGG tumor samples from NanoString correlated with IBA1 positivity in matched samples. *p<0.05, **p<0.01, ***p<0.001, ****p<0.0001.

Methods

Mice

All injections were performed in mice pups aged 0-2 days old among equally distributed sexes for each genotype. *Ntva;Pten*$^{fl/fl}$*;Ink4a-Arf*$^{-/-}$ mice are in a mixed genetic background while *Ntva/Pten*$^{fl/fl}$ mice are in a pure C57BL/6 background. Mice were house in a climate-controlled, pathogen-free facility with access to food and water ad libitum under a 12-hour light/dark cycle. Genotyping of all mice was performed using Transnetyx (Transnetyx Inc., Cordova TN). *Ccl2* (#004434) and *Ccl7* (#017638) knockout mice were obtained from the Jackson Laboratory and crossed to CL57BL/6 *Ntva;Pten*$^{fl/fl}$ mice until homozygous knockout mice were obtained as previously described for the generation of *Ntva;Pten*$^{fl/fl}$*;Ccl2*$^{-/-}$ mice (95, 156). *Ccl3* knockout mice were gifted by Dr. C.K. Qu, *Ccl8/12*$^{-/-}$ mice were gifted by Dr. Sabina Islam, and both were crossed with CL57BL/6 *Ntva;Pten*$^{fl/fl}$ mice until homozygous knockout mice were obtained (156, 157). All experimental procedures were approved by the Institutional Animal Care and Use Committee (IACUC) of Emory University (Protocol #2003253 and #201700633).

Cell Cultures and Injections

DF1 cells (ATCC, CRL-12203) were grown at 39^{o}C, expanded to passage 4 and transfected with RCAS-PDGFB-HA, RCAS-PDGFA-Myc, or RCAS-shp53-RFP using a Fugene 6 Transfection kit (Roche, no. 11814443001). Cells were cultured with DMEM media (Gibco, 11995-065) supplemented with 1% L-glutamine, 1% penicillin/streptomycin, and 10%FBS (ATCC). Transfected DF1 cells were used for injections before reaching passage 25. DF1 cells were injected as equal mixtures of $4x10^4$ cells per µL, 1µL per mouse, in pups aged 0-2 days old using a 30-gauge needle attached to a Hamilton syringe.

Flow Cytometry

Mice were anesthetized with a Ketamine/Xylazine mix and perfused with ice-cold Ringer's solution. Tumors were dissociated using the Miltenyi Neural Tissue Dissociation kit (Miltenyi, 130-092-628) or collagenase D (Sigma 11088866001) following manufacturer's protocol. Single-cell suspensions were strained through a 70µm cell strainer and centrifuged at 450*xg* for 10 minutes at 4°C. Cells were then subjected to a 30% Percoll gradient (GE Healthcare, 17-0891-01) with 10% FBS (Hyclone, SH30396.03) and centrifuged at 800*xg* for 15 minutes at 4°C. Cells were washed with PBS and resuspended in red blood cell lysis buffer (BioLegend, 420301) for 1 minute at 37°C before being blocked for 30 minutes on ice with a solution containing 2% FBS, 5% normal rat serum, 5% normal mouse serum, 5% normal rabbit serum, 10µg/ml anti-FcR (BioLegend, 101319) and 0.2% NaN_3 in DPBS). After blocking, cells were stained for CD45-APC, CD11b-PerCP-Cy5.5, Ly6C-PE-Cy7, Ly6G-V450, and MHC-II-FITC on ice for 30 minutes. 50,000 events were recorded on a BD-LSR II flow cytometer. For single cell sorting, a FACS Aria II was used. Data was compensated and quantified in FlowJo 10.4.1. Total TAM population was considered as $CD45^{+}CD11b^{+}$. Microglia were $CD45^{med/lo}$;$CD11b^{+}$, BMDMs were $CD45^{hi}CD11b^{+}$, lymphocytes were $CD45^{+}$;$CD11b^{-}$, inflammatory monocytes were $CD45^{+}CD11b^{+}Ly6C^{hi}Ly6G^{lo}$, macrophages were $CD45^{+}CD11b^{+}Ly6C^{lo}Ly6G^{lo}$, and neutrophils were $CD45^{+}CD11b^{+}Ly6C^{hi}Ly6G^{hi}$.

Immunohistochemical Staining

Mice were sacrificed as described above, and brains were removed and fixed in 10% neutral buffered formalin for 72 hours. The brains were then embedded in paraffin and sectioned at 5µm per slide and mounted. Hematoxylin and eosin staining was performed for each sample. Antibodies used for specific staining include; IBA1 (Wako 019-19741, 1:250) Phospho-histone 3 (CST 9701S, 1:200), CD31 (Dianova Dia-310, 1:50), α-SMA (Dako M0851, 1:200),

PDGFRα (CST 3174S, 1:500), and PDGFRβ (CST 3169S, 1:100). Staining was performed manually or on the Discovery XT Platform (Ventana Medical Systems, Inc., Tuscon, USA) at the defined dilutions in 2% bovine serum albumin in phosphate-buffered saline.

Image Analysis

Stained samples were processed as described in Chapter 3. For IBA1, SMA, CD31, PDGFRα, and PDGFRβ staining, the percentage of positively stained tumor area was calculated. For phospho-histone 3, the number of positively stained nuclei per mm^2 was quantified. All image analysis was performed using ImageJ Fiji.

Quantitative PCR

After perfusion with ice-cold Ringer's solution, mice brains were extracted and tumor tissue was snap-frozen in liquid nitrogen for storage (-80^{o}C) and later use. RNA extraction was performed using the RNease Lipid Tissue Mini Kit (Qiagen #74804) according to the manufacturer's instructions. A NanoDrop (Thermo Scientific) was used to determine RNA concentrations and an RNA bleach gel was run to confirm RNA integrity. 1µg of RNA was then used to synthesize cDNA using the SuperScript III First-Strand Synthesis System (Invitrogen). cDNA was used for quantitative PCR (qPCR) using the SsoAdvanced SYBR Green Supermix (Bio-Rad) on an Applied Biosystems 7500 Fast Real-Time PCR System (Life Technologies). PrimePCR SYBR Green Assay primers were obtained from Bio-Rad. β-Actin was used as an internal reference gene and an inter-run calibrator was used to normalize comparative CT values for the combination of plates when necessary. Hierarchical clustering was performed on Log2 standardized qPCR data using Morpheus (Broad Institute). See Table 2 on page 99 for a list of all primers used.

Nanostring Analysis

RNA was isolated as described above. RNA integrity was confirmed using a bioanalyzer and samples possessing a DV300% greater than 30 were used. 50ng of RNA was used for NanoString analysis with the mouse pan cancer pathways immune panel (NanoString, XT-CSO-MIP1-12). All data analysis was processed and normalized using nSolver Analysis Software version 4.0 and GraphPad Prism 8 (GraphPad Software, San Diego, CA).

Proliferation Assays

Primary tumor tissue was dissociated and tumor cells were cultured in NeuroCult Basal Medium (Stemcell, 05700) supplemented with NeuroCult Proliferation Supplement (Stemcell, 05701), EGF [20ng/mL], FGF [20ng/mL], and Heparin (0.25%). 75,000 or 100,000 Single cells were plated as a monolayer in 12 well plates coated with vitronectin (Corning Synthemax, 89235-046), accutased at designated time points, and then the Click-iT Plus Edu Kit (Invitrogen, C10636) was used according to manufacturer's protocol. Cells were then run on a BD-LSR II flow cytometer and analyzed in FlowJo.

BMDM and Microglia Cell Cultures

BMDMs from adult CL57BL/6 mice were isolated and cultured as follows. Mice were euthanized and bone marrow was immediately extracted from the tibia and femur of the hind legs using harvest solution containing 1xDPBS, 0.5%BSA in IMDM (Gibco, 12440-046), 0.2% Heparin, 2% DNAse, and 4% Penicillin/Streptomycin. Cells were cultured at 37ºC for 6 days in DMEM high glucose culture medium (Gibco, 10569-010) supplemented with 10% FBS, 1% L-glutamine, 1% Penicillin/Streptomycin, and M-CSF [40ng/mL]. On day 7 post isolation, 2 million cells/well were plated in a 6 well tissue culture treated plate and were incubated overnight. The next morning cells were incubated in FBS deficient media (0.5%) for 3 hours and then stimulated with recombinant human PDGFA ([0-100ng/mL]; R&D Systems) or PDGFB

([0-100ng/mL]; R&D Systems) for 6 hours. Supernatant was collected and stored at -80ºC. RNA was collected using Trizol (ThermoFisher) added directly to the tissue culture plate and then stored at -80ºC.

Microglia were isolated as follows. Using sterile instruments, brains were collected from newborn CL57BL/6 mice 0-2 days old, and the cerebellums were removed. Brains were then digested in 0.25% Trypsin with 5mg/mL DNase I and incubated at 37ºC for 10 minutes. Samples were then triturated with complete DMEM, passed through a 70 µm cell strainer, and centrifuged at 600rpm for 5 minutes at 4ºC. Cells were then washed with DMEM, centrifuged at 600rpm for 5 minutes at 4ºC, and plated on a poly-D-lysine coated [10mg/mL] T75 flask. Fresh media containing M-CSF [40ng/mL] was added every 3 days. After approximately 10 days, microglia were gently rinsed off the flask and centrifuged for 10 minutes at 1100rpm. 1 million cells/well were then plated on a 6-well tissue culture treated plate overnight. Cells were then incubated in FBS deficient media for 3 hours prior to stimulation with PDGFA or PDGFB as described above.

Cytokine Array

Snap frozen tumor tissue was homogenized and lysed in 1x PBS lysis buffer containing 1% Triton, 10µg/mL Aprotinin (Sigma, A6279), 10µg/mL Leupeptin (Sigma, L8511), and 10µg/mL Pepstatin (Sigma, P4265). 500µg of pooled sample protein from three tumors per group was used according to manufacturer's instructions for the Mouse Cytokine Array Panel A (R&D Systems, ARY006). The blot was developed and visualized via HRP. Densitometry quantification was performed in ImageJ Fiji.

Enzyme Linked Immunosorbent Assay

Snap frozen tumor tissue was mechanically homogenized and sonicated in lysis buffer supplemented with protease and phosphatase inhibitors. Cell lysates were subjected to sonication

in supplemented lysis buffer. Protein concentrations were determined using a Bradford protein assay (BioRad, 5000001). ELISA assays were performed for CCL2 (R&D, DY-479), CCL7 (Boster, EKO683), CCL8 (R&D, DY790), CCL12 (R&D, MCC120 and VEGFA (R&D, MMV00) according to the manufacturer's instructions.

Data Analysis

For qPCR data normalization, ddCT values were Log2 transformed before z-score standardization. The reference calibrator sample was a PDGFB-driven tumor generated in a *Ntva;Cdkn2a*$^{-/-}$ mouse. Statistical tests used for each analysis are further explained in figure legends. GraphPad Prism 8 (GraphPad Software, San Diego, CA) was used for all statistical analyses.

Chapter 5

Histone Mutations Confer Unique pHGG Subgroups

Until this point, all experimental data shown in this dissertation has been in histone wild type tumors induced in the cortical hemisphere. However, as mentioned in Chapter 1, almost half of all pHGGs are found in the midline or brainstem. In order to study the mechanisms of TAM infiltration in all subgroups of pHGG we also performed studies on histone mutant tumors as well. As previously performed, tumors were induced in *Ntva;Cdkn2a*$^{-/-}$ mice using RCAS-PDGFA or RCAS-PDGFB, and for *Ntva;Cdkn2a*$^{wt/wt}$ mice the addition of RCAS-shp53 was utilized. An additional RCAS construct introducing either H3.3K27M or H3.3G34R/V was also administered with the respective oncogenic drivers to recapitulate histone mutant tumors. H3.3K27M tumors were induced in the brainstem and H3.3G34R/V tumors were induced cortically.

Up to 90% of DIPGs contain mutations in *H3F3A* or in *HIST1H3B* resulting in H3K27M mutations (17). Tumors possessing H3K27M mutations are thought to arise during CNS development in neural precursor cells (158). Tumors with these mutations are mutually exclusive with H3G34R mutations and commonly possess *TP53* loss of function mutations and amplifications of *PDGFRA* (19, 20, 159-161). Histones H3.1 and H3.3 are synthesized during different stages of the cell cycle. H3.1 is produced during the S-phase and is utilized to package newly synthesized DNA. H3.3 is synthesized during interphase and is deposited on actively transcribed genes by ATRX/DAXX (17, 23, 162). H3.3K27M mutant tumors are more common and clinically aggressive than H3.1K27M mutant tumors (9, 160). Although the mutated histone proteins only make up 3-17% of the total H3 pool in DIPG samples, they lead to almost complete loss of H3K27me3 throughout all affected cells (23, 163, 164). These global hypomethylation

effects are due to inhibition of the enzymatic activity of EZH2, a subunit of the Polycomb Repressive Complex 2 (PRC2), by the mutated histone (163, 164). PRC2 is responsible for maintaining di and tri-methyl marks on H3.3K27, and PRC2 target genes are involved in developmental processes important for stem cell regulation, cellular proliferation, and differentiation (17, 165-167). Other groups have demonstrated through single cell sequencing of human and murine DIPG K27M mutant tumors that few genes are down-regulated in comparison to other tumors, and many PRC2 target genes are upregulated (168, 169). Further, they found the majority of cells in these tumors were self-renewing oligodendrocyte progenitor cell-like (OPC), indicating the K27M mutation likely hinders OPC differentiation into oligodendrocytes (168).

Much is known regarding K27M mutations in DIPGs and midline gliomas. Less is known regarding H3G34R/V mutations, which arise exclusively in the hemispheres of the brain. These mutations are found in up to 36% of pHGGs in the cortical hemispheres and frequently have co-occurring mutations with *TP53* (100%) and *ATRX/DAXX* (50%) (18, 20, 170, 171). Similar to K27M tumors which have global hypomethylation, the G34R mutation causes a diminishment of K36me3 but unlike the K27M, the reduction in methylation occurs only on the affected mutant alleles (23, 163). This loss in methylation is due to the close proximity of the H3G34 position to the K36 location, which is an important transcriptional regulator (172). Interestingly, G34R tumors were found to have a greater mutational burden than other subgroups and possess multiple numbers of subclones. These effects are likely due to the deficiency in DNA repair caused by *ATRX/DAXX* mutations which promote telomere destabilization (173, 174). The effects histone mutations have on the inflammatory microenvironment in pHGG remains unknown and highly understudied. The aims of the following studies were to characterize TAM

infiltration in these tumors and uncover the relationship between molecular driver mutations, tumor location, and the resulting inflammatory microenvironments.

NanoString Analysis of Histone Mutant Murine HGGs

Because histone mutations arise in specific anatomic locations, this begs the question of whether the molecular identity of the tumor or location of the tumor itself is the most important factor controlling the inflammatory TME and immune infiltrate. To answer this question, using *Ntva;Cdkn2a*$^{-/-}$ mice and RCAS-PDGFB, H3.3WT hemisphere, H3.3WT brainstem, H3.1K27M brainstem, and H3.3K27M brainstem tumors were generated (**Figure 20a**). Tumors were validated by IHC for the presence or absence of H3K27me3 (**Figure 20b**). Freshly dissected tumor tissue was then collected and RNA isolated for NanoString analysis. First, to determine whether the tumor location dictates the immune microenvironment, H3.3WT hemispheric tumors were compared to H3.3WT brainstem tumors. Interestingly, these tumor samples clustered almost completely apart from one another (**Figure 21a**). Pathway analysis revealed brainstem tumors have higher expression of genes involved in inflammatory processes including chemokines and cytokines, leukocyte functions, macrophage functions, pathogen response, complement pathway, and more. Conversely, hemispheric tumors had higher expression of genes involved in cancer progression, cell cycle, apoptosis, and adhesion compared to the brainstem tumors. A total of 37 genes were DE at a corrected p-value of <0.05, and the majority of them were more highly expressed in hemispheric samples (**Figure 21b**). Some of the DE genes found higher in hemispheric tumors include *Il16, Hsd11b1, Itgb4, Itgax, Nefl, Cd36, Rorc,* and *Rora.* Antigen presentation molecules including *H2-Aa, H2-Eb1, H2-Ab1,* and *H2-DMb2,* as well as immunosuppressive markers *Pdcd1* (PDL1) and *Cd274* (PD1) were also highly expressed in hemispheric tumors. *Vim* was the most DE gene found highly expressed in brainstem samples.

Genes involved in dampening the immune response including *Adora2a* (Adenosine Receptor A2A) and *Arg1* (Arginase) were also high in brainstem tumors. Interestingly, *Cxcl1*, which was found to be the most significantly DE gene in human DIPG samples, was highly expressed in brainstem tumors indicating this may be an important gene involved in brainstem tumor biology.

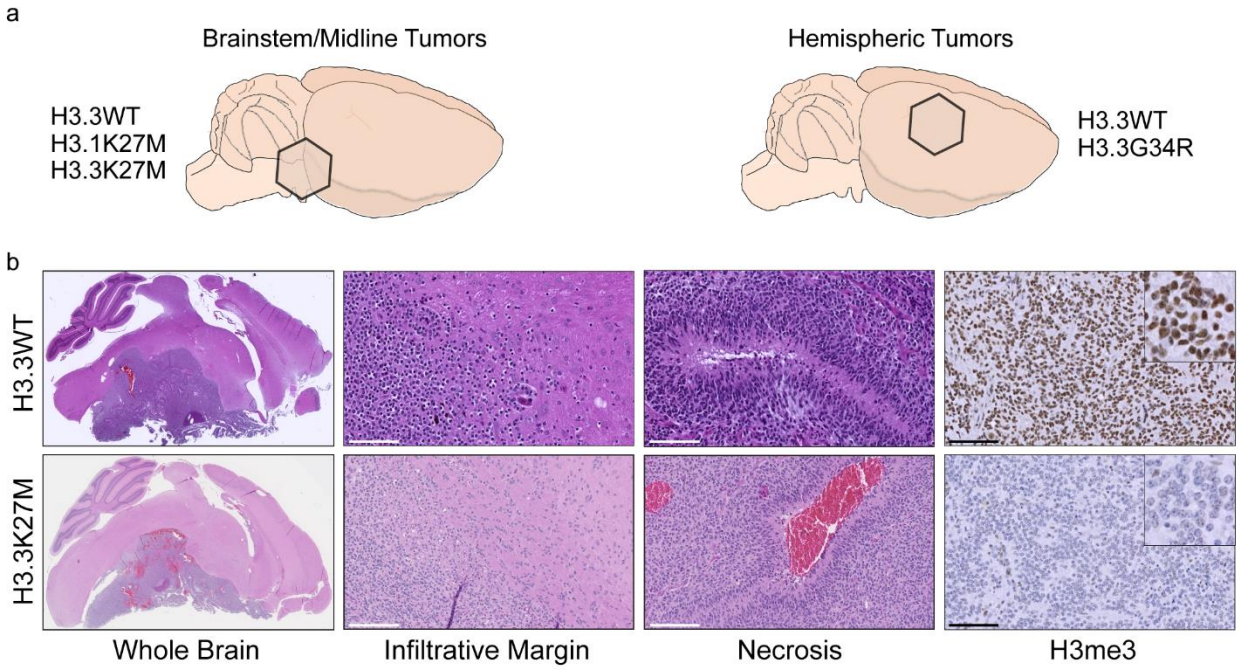

Figure 20: Modeling of Histone Mutant HGGs. (a) Tumors were generated in *Ntva;Cdkn2a*$^{-/-}$ mice, driven by RCAS-H3.3WT, RCAS-H3.1K27M, or RCAS-H3.3K27M along with RCAS-PDGFB in the brainstem. Tumors generated in the hemispheres were driven by RCAS-H3.3WT or RCAS-H3.3G34R along with RCAS-PDGFB. **(b)** H&E images of H3.3WT or H3.3K27M tumors displaying the classic histological features of a high-grade glioma along with reduced H3me3 staining in H3.3K27M tumors. 40x and 80x magnified images, scale bars=100μm.

Next to determine whether the molecular identity of tumors found in the same location dictate inflammatory expression profiles, a comparison between H3.3WT and H3.3K27M brainstem tumors was made. There were no significantly DE genes between the two tumor subgroups so a comparison between H3.1K27M and H3.3K27M tumors was then made. This analysis revealed major differences between the two subtypes of brainstem tumors as they clustered distinctly apart from each other (**Figure 21c**). The H3.3K27M tumors, which have historically had worst patient prognosis and shorter median survival, were found to have a greater inflammatory profile compared to H3.1 mutant tumors. Again, major inflammatory processes such as chemokines and cytokines, inflammation, interleukins, leukocyte functions, macrophage functions, innate and adaptive immune responses were highly represented in H3.3K27M tumors. There were 77 DE genes including *Nefl, Itgb4, CD274, H2-Eb1, Thy1, Cxcl1, Cxcl13, Cxcl11, Il1b,* and *Cd83* which were more highly expressed in 3.3K27M samples (**Figure 21d**). *Smad4, Mcam, Tgfb2, Adora2a, Spp1* (Ostepontin), *Vegfa,* and others were more highly expressed in H3.1K27M samples.

Finally, an analysis with all tumor types and locations was performed. Unsupervised hierarchical clustering of samples based on their pathway scores revealed H3.1K27M brainstem tumors clustered with H3.3WT hemispheric tumors and H3.3K27M brainstem tumors clustered with H3.3WT brainstem tumors (**Figure 21e**). Together, this data indicates tumor location is the most important factor in creating differential inflammatory expression patterns and when tumors are in the same location, only then does the molecular identity confer observable differences. These findings raise the question of what microenvironmental differences in the brainstem versus the hemispheres drive these gene expression discrepancies? Only one other group has sought out to determine location-based differences in pHGGs and they found through MRI that the BBB in

the brainstem is less permeable and therefore these tumors are less contrast enhancing compared to their hemispheric counterparts (175). This raises another important question of how does BBB permeability affect macrophage and immune cell infiltration and whether their infiltration relies more on chemokine signaling events or a compromised BBB. Future studies should be aimed at answering these questions as they likely hold the key to identifying important therapeutically exploitable mechanisms.

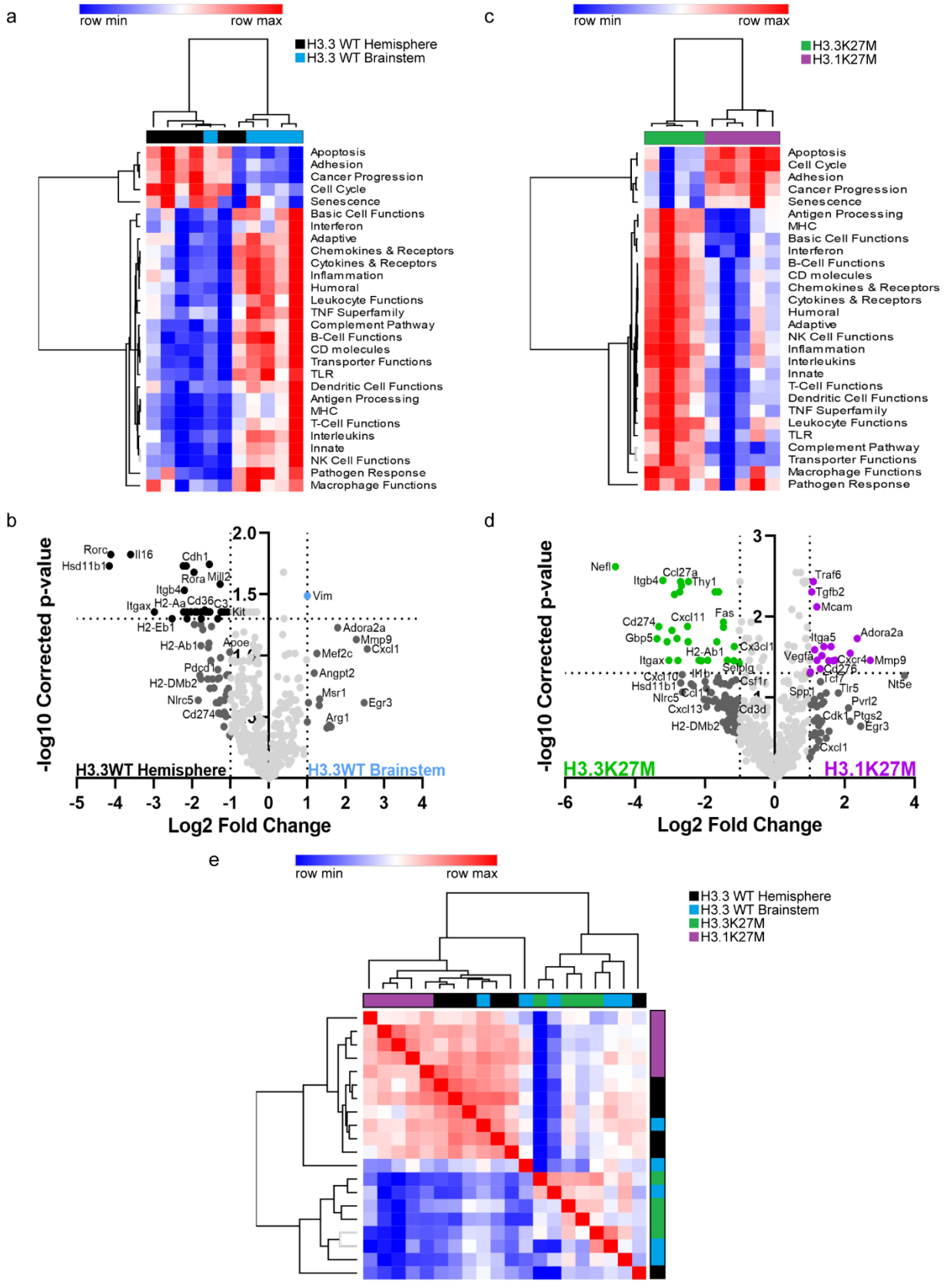
a
row min
row max
H3.3 WT Hemisphere
H3.3 WT Brainstem
Apoptosis
Adhesion
Cancer Progression
Cell Cycle
Senescence
Basic Cell Functions
Interferon
Adaptive
Chemokines & Receptors
Cytokines & Receptors
Inflammation
Humoral
Leukocyte Functions
TNF Superfamily
Complement Pathway
B-Cell Functions
CD molecules
Transporter Functions
TLR
Dendritic Cell Functions
Antigen Processing
MHC
T-Cell Functions
Interleukins
Innate
NK Cell Functions
Pathogen Response
Macrophage Functions
c
row min
row max
H3.3K27M
H3.1K27M
Apoptosis
Cell Cycle
Adhesion
Cancer Progression
Senescence
Antigen Processing
MHC
Basic Cell Functions
Interferon
B-Cell Functions
CD molecules
Chemokines & Receptors
Cytokines & Receptors
Humoral
Adaptive
NK Cell Functions
Inflammation
Interleukins
Innate
T-Cell Functions
Dendritic Cell Functions
TNF Superfamily
Leukocyte Functions
TLR
Complement Pathway
Transporter Functions
Macrophage Functions
Pathogen Response
b
-log10 Corrected p-value
Log2 Fold Change
H3.3WT Hemisphere
H3.3WT Brainstem
Rorc
Il16
Hsd11b1
Cdh1
Rora
Mill2
Itgb4
Itgax
H2-Aa
Cd36
C3
Kit
H2-Eb1
H2-Ab1
Apoe
Pdcd1
H2-DMb2
Nlrc5
Cd274
Vim
Adora2a
Mmp9
Cxcl1
Mef2c
Angpt2
Msr1
Egr3
Arg1
d
-log10 Corrected p-value
Log2 Fold Change
H3.3K27M
H3.1K27M
Nefl
Itgb4
Ccl27a
Thy1
Cd274
Cxcl11
Fas
Gbp5
H2-Ab1
Cx3cl1
Itgax
Selplg
Csf1r
Hsd11b1
Nlrc5
Ccl11
Cxcl13
Cd3d
H2-DMb2
Traf6
Tgfb2
Mcam
Itga5
Adora2a
Vegfa
Cxcr4
Mmp9
Cd276
Tcf7
Tlr5
Nt5e
Spp1
Pvrl2
Cdk1
Ptgs2
Egr3
Cxcl1
e
row min
row max
H3.3 WT Hemisphere
H3.3 WT Brainstem
H3.3K27M
H3.1K27M

Figure 21: NanoString Analysis of Histone Mutant Murine HGGs. (a) Unsupervised hierarchical clustering of H3.3WT hemispheric (n=6) and H3.3WT brainstem (n=5) tumors generated in *Ntva;Cdkn2a*$^{-/-}$ mice driven by RCAS-PDGFB. Clustering is based on pathway scores obtained from NanoString analysis. **(b)** Volcano plot of differentially expressed genes in H3.3WT hemispheric and H3.3WT brainstem tumor samples as detected by NanoString. **(c)** Unsupervised hierarchical clustering of H3.1K27M (n=5) and H3.3K27M (n=4) tumors generated in *Ntva;Cdkn2a*$^{-/-}$ mice driven by RCAS-PDGFB. Clustering is based on pathway scores obtained from NanoString analysis. **(d)** Volcano plot of differentially expressed genes in H3.1K27M and H3.3K27M tumor samples as detected by NanoString. **(e)** Similarity matrix of H3.3WT hemisphere, H3.3WT brainstem, H3.1K27M, and H3.3K27M tumors based on their expression of 484 genes detected in NanoString.

Survival Analysis of Histone Mutant Murine HGGs

Survival analysis of each histone mutant tumor type revealed PDGFB-driven tumors consistently had a decreased median survival compared to PDGFA-driven tumors, further supporting the notion PDGFB is a strong oncogenic driver. In *Ntva;Cdkn2a*$^{wt/wt}$ mice, both PDGFA and PDGFB-driven tumors combined with H3.3K27M and shp53 resulted in decreased median survival compared to H3.3WT tumors (**Figure 22a**). In *Ntva;Cdkn2a*$^{-/-}$ mice, PDGFA+H3.3K27M tumors had a significantly decreased median survival compared to H3.3WT tumors while in PDGFB-driven tumors there were no survival differences between H3.3WT, H3.1K27M, and H3.3K27M (**Figure 22b**). This was also observed between H3.3WT and H3.3G34R/V tumors as well (**Figure 22c-d**). These results suggest the loss of *Cdkn2a* and use of PDGFB as an oncogenic driver masks the survival differences observed between histone wild type and histone mutant tumors. All of these survival results were also observed by Cordero et al., confirming the validity of our models (169).

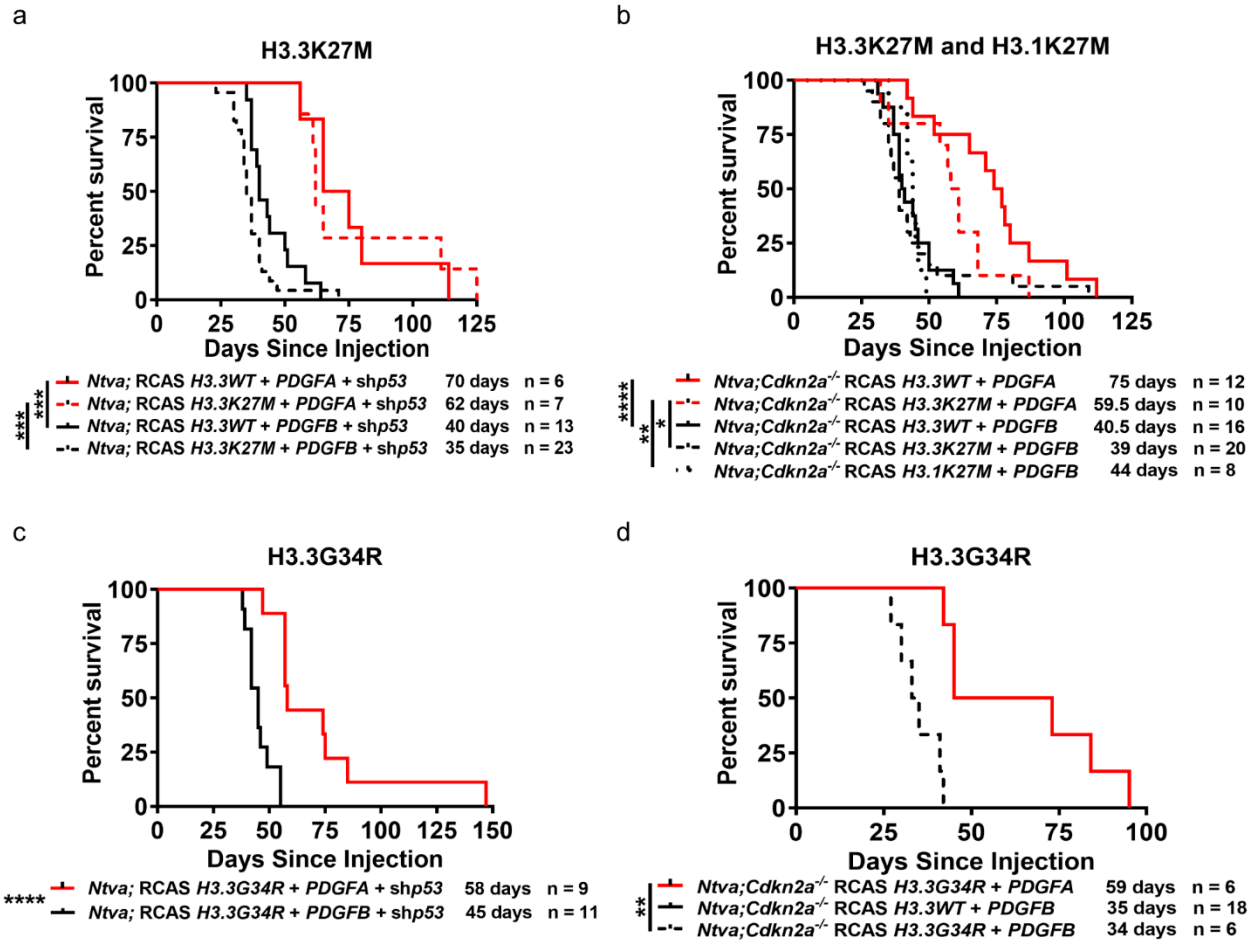

Figure 22: Survival Analysis of Histone Mutant Murine HGGs. Survival curves of: **(a)** *Ntva* mice with tumors generated by RCAS-H3.3WT or RCAS-H3.3K27M along with RCAS-PDGFA or RCAS-PDGFB and RCAS-shP53. **(b)** *Ntva;Cdkn2a*$^{-/-}$ mice with tumors generated by RCAS-H3.3WT or RCAS-H3.3K27M along with RCAS-PDGFA or RCAS-PDGFB. **(c)** *Ntva* mice with tumors generated by RCAS-H3.3G34R along with RCAS-PDGFA or RCAS-PDGFB and RCAS-shP53. **(d)** *Ntva;Cdkn2a*$^{-/-}$ mice with tumors generated by RCAS-H3.3WT or RCAS-H3.3G34R along with RCAS-PDGFA or RCAS-PDGFB. *p<0.05, **p<0.01, ***p<0.001, ****p<0.0001.

Methods

Mice

All injections were performed in mice pups aged 0-2 days old as previously described in Chapter 4.

Cell Cultures and Injections

DF1 cells (ATCC) were grown at 39^{o}C as previously described in Chapter 4. DF1 cell lines used included RCAS-H3.3WT, RCAS-H3.31K27M, RCAS-H3.3K27M, and RCAS-H3.3G34R-HA.

Immunohistochemical Staining

Mice were sacrificed and processed as described above. Hematoxylin and eosin as well as H3me3 (Cell Signaling 9733S, 1:200) staining was performed. Staining was performed manually at the defined dilutions in 2% bovine serum albumin in phosphate-buffered saline.

NanoString Analysis

All tumor samples were processed for RNA isolation and NanoString analysis was run as described in Chapter 4 using the pan cancer immune profiling kit for mouse (XT-CSO-MIP1-12).

Chapter 6

Future Proposed Experimental Studies

Tumor Location Versus Tumor Molecular Identity

All of the results presented have led to several main conclusions. First, human pHGGs classified as DIPG, which are found in the brainstem, have a greater inflammatory gene expression profile compared to pHGGs classified as GBM, or those found in the cortical hemispheres. These results suggest the tumor location and/or the molecular identity of the tumor itself impacts the inflammatory microenvironment. To begin addressing this postulate, we performed NanoString on mouse pHGGs induced in different brain locations along with different genetic drivers which represent the human disease. Our initial results indicate the location in which the tumor is induced is the most important determining factor affecting the inflammatory profile. When comparing two tumors in the same location but with different genetic drivers, only then are there significant expression differences. The next experimental steps would be to perform IBA1 staining in each of the mouse tumor samples induced in different locations and genetic backgrounds to determine if the infiltration of TAMs is also influenced by any or all of these factors. Flow cytometry should also be performed to determine the identity of the infiltrating immune cells. Other infiltrating immune cells including cytotoxic T-cells, T-helper cells, exhausted T-cells, and dendritic cells should also be analyzed. Another pertinent question worth exploring is what microenvironmental factors in the brain's distinct regions are driving the expression differences observed in our NanoString datasets? To answer this question, naïve brain tissue from the hemispheres and brainstem should be collected and used for molecular sequencing and metabolic profiling. These results should then be compared to tumor samples to determine what factors are driving location-based inflammatory differences. These analyses will

allow us to dissect and understand the differences observed in different pHGGs including DIPG and GBMs.

These studies also demonstrate human pHGGs have a relatively low abundance of infiltrating T-cells, yet they have a high number of infiltrating TAMs. Although we do not know the identity of these TAMs, it is hypothesized they are of monocytic origin as our mouse modeling demonstrated. There was minimal PDGFA staining in human pHGGs. However, correlative studies showed human pHGGs with high expression of CD31, PDGFRβ, and PDGFB have high TAM infiltration, suggesting PDGFB/Rβ activity promotes the infiltration of TAMs. Future experiments would benefit greatly from high throughput techniques such as CyTOF or RNA sequencing on fresh human tumor samples. Studies like these would allow us to perform stronger correlative analyses and facilitate the discovery of potential druggable targets or cell types that are otherwise undetectable in small histological studies.

Cell Sorting of Murine HGGs

Several experiments demonstrated murine tumors driven by PDGFB overexpression have a stronger inflammatory TME compared to PDGFA-driven tumors. qPCR and NanoString results indicated PDGFB-driven tumors have high expression of chemokines such as *Ccl2, Ccl7, Ccl11, Ccl12,* and *Cxcl13.* They also had high expression of inflammatory adhesion molecules such as *Cd11b, Cd74,* and *Selplg.* Although an *in vitro* attempt was made to determine which cell type is most responsible for the production of these inflammatory signals, these studies were limited to just BMDMs and microglial cultures. We found in response to PDGFB stimulation but not PDGFA stimulation, BMDMs upregulate their expression of chemokines. Microglia were unresponsive to stimulation. This suggests BMDMs are more responsible for the production of inflammatory markers in the pHGG TME, however, expression of these genes was not

investigated in tumor cells. Therefore, in order to gain a more comprehensive understanding of the exact cell types responsible for these inflammatory signals, tumors should be FACS sorted for tumor cells, BMDMs, and microglia. Either qPCR for specific genes or RNA sequencing should be performed on the sorted cell populations to determine each cell type's expression. In these studies, all tumors generated in *Ntva;Cdkn2a*$^{wt/wt}$ mice were done so using RCAS-shp53RFP. All tumor cells should therefore be RFP positive and easily detected by a flow cytometer. All RFP negative cells are TME cells including BMDMs and microglia, among others. Sorting the RFP negative cells by their expression of CD45 and CD11b would then allow for the detection and collection of individual TAM populations (**Figure 23**). Four tumors have so far been sorted and their cells collected for RNA isolation. Because tumor cells are the most abundant cell type in these tumors, upwards of 850,000 tumor cells were collected per tumor. However, because BMDMs and microglia are less abundant, as little as 4,100 cells per tumor were collected per TAM population. Due to the low cell numbers, sorted cells from multiple tumors must be pooled together before performing any experimental analyses.

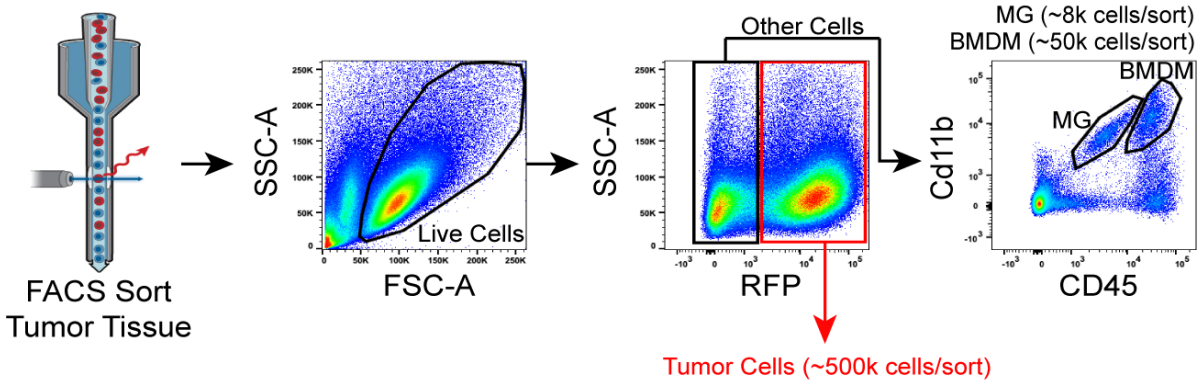

Figure 23. Cell Sorting of Murine pHGGs For Single Cell Expression Analysis. Flow cytometry cell sorting scheme depicting the separation and collection of RFP+ tumor cells and RFP- TAMs. TAMs are further gated on CD45 and CD11b positivity to separate BMDMs from microglia. On average per tumor, ~500,000 tumor cells, ~50,000 BMDMs, and ~8,000 microglia are obtained from tumors generated in *Ntva* mice driven by RCAS-PDGFB with RCAS-shP53RFP.

Pharmacologic Inhibition of PDGF Pathway

Survival differences were not observed in *Ccl2, Ccl7,* or *Ccl8/12*$^{-/-}$ mice in tumors driven by PDGFB. However, *Ccl3* and *Ccl8/12*$^{-/-}$ mice all survived longer when driven by PDGFA. It is evident PDGFB is a strong oncogenic driver that masks the effects of single gene knockouts. One reason for this is because PDGFB is an inducer of the monocyte chemoattractant family of proteins (MCP) and therefore compensatory mechanisms may be taking place when one family member is knocked out (176-179). One experimental approach to determining whether MCP family members are important for the chemoattraction of TAMs in PDGF-driven tumors would be to delete all MCP genes in a single mouse. Because this would require generating a quadruple knockout mouse this approach would be time very intensive. However, using alternative methods such as Crispr-Cas9 deletion of multiple chromosomal segments may make this more realistic.

Because PDGFB tumors have greater TAM infiltration, it begs the question of whether PDGFB itself is a chemoattractant for BMDMs and other immune cells. To test this hypothesis, multiple approaches could be taken. Tumors generated by PDGFB overexpression in *Ntva;Cdkn2a*$^{-/-}$mice should be treated with either a PDGFB neutralizing antibody or a PDGFRβ inhibitor. Because these mice have a median survival of 28 days, an initial treatment schedule should start ~15 days after injecting the RCAS producing DF1 cells. If this produces no survival benefit, a different treatment schedule should be adopted. Another more sophisticated approach would be to induce cell-type specific deletion of PDGFRβ. *Ntva;PDGFRβ* floxed mice would be crossed with cell-type specific Cre mice to generate mice deficient of PDGFRβ in cells such as BMDMs, SMA positive cells, or endothelial cells. Tumors would then be induced using the RCAS-Tva system and survival analysis would be performed. Additionally, for all approaches, flow cytometry should be performed to determine if PDGF inhibition results in a reduction of

infiltrating immune cells. In addition to *in vivo* experiments, supplemental *in vitro* experiments should be performed. Using an *in vitro* migration assay with cultured BMDMs stimulated with or without PDGFB would determine if PDGFB acts as a chemoattractant. Then, adding a PDGFB neutralizing antibody or PDGFRβ inhibitor to the culture medium would allow for the direct observation of PDGF inhibition on BMDM migration.

T-Cell Profiling of Murine pHGGs

Flow cytometry analysis indicated PDGFB-driven tumors have a significantly greater number of lymphocytes compared to PDGFA-driven tumors. However, the identity of these lymphocytes is unknown as both T and B-cell populations are identified using our antibody panel of CD45 and CD11b. Using additional antibodies for CD3, CD4, CD8, and FOXP3 would allow us to distinguish what types of T-cells are being attracted to these tumors. Since PDGFB-driven tumors have a lower median survival and greater TAM infiltration, it can be hypothesized the number of exhausted or dysfunctional T-cells (FOXP3+) may be greater in these tumors or there is a lack of T-cell presence altogether. To functionally confirm flow cytometry findings, TAM co-culture experiments with T-cells should also be performed. PDGFB-driven tumors should be dissociated, FACS sorted for BMDMs, microglia, and tumor cells, and then each cell population should be co-cultured with isolated T-cells from $Rag2^{-/-}$ mice. A T-cell proliferation assay would inform us of whether TAMs or tumor cells from PDGFB tumors suppress T-cell proliferation.

***In vivo* Time Course Experiments For TAM Infiltration**

All of the data presented in this dissertation come from mice at terminal stage when the tumor has grown to maximum capacity. There are plenty of differences observed in TAM infiltration and mRNA expression profiles between PDGFA and PDGFB-driven tumors at this timepoint. However, because PDGFB tumor bearing mice have a significantly decreased median

survival the question becomes whether the differences observed between the two tumor types can be observed at earlier timepoints? Further, when do peripheral circulating BMDMs infiltrate into the tumor? Do they arrive at early stages of tumor development and aid tumor progression or do they arrive once the tumor has grown as a result of tumor progression? I hypothesize BMDMs infiltrate into the tumor at early stages and respond to tumor derived signals by producing their own chemoattractant molecule, recruiting more BMDMs in the process. qPCR data also suggests BMDMs can promote angiogenesis as shown by an increase in *Vegf* expression upon PDGFB stimulation. This hypothesis assumes there is a chemoattractant released by tumor cells which recruit BMDMs in the early stages of tumor development. To approach answering this hypothesis, RCAS-shp53 and RCAS-PDGFA or RCAS-PDGFB would be administered to *Ntva;Cx3cr1*$^{GFP/WT}$*Ccr2*$^{RFP/WT}$ mice, similarly to what was done in a previous paper from our lab in 2017 for adult GBM (95). For PDGFB tumors, mice would be sacrificed and perfused with paraformaldehyde every 3-5 days starting at day 10 post injection. For PDGFA tumors, they would be sacrificed and perfused every 3-5 days starting at day 15 post injection. Using these mice, infiltrating BMDMs would be RFP positive and brain-resident microglia would be GFP positive upon immunofluorescent staining. Tissue sections would be imaged and quantified for the presence or absence of TAM populations at each stage of tumor development.

Concluding Remarks

As previously mentioned, little is known concerning the infiltrating immune cell populations in pHGG or what role these cells play in promoting tumor progression and immune suppression. This is an unexplored frontier of pHGG research and promises to be fruitful to those studying it. For a disease with a median survival of 12-15 months, where no chemotherapeutics provide substantial extension of life, where tumor resection results in tumor recurrence, we *must*

develop alternative therapeutic strategies to treat them. Immunotherapy is a promising route due to the ability to harness a child's own immune system rather than using exogenous chemotherapies that have many off target side effects. In order to develop effective immunotherapies we must first develop a foundational understanding of what these tumors look like from a molecular level all the way to a systems level. Establishing which immune cell types are present, how they are getting there, and what they are doing in the tumor will allow us to identify targetable mechanisms for therapeutic exploit. Although knowledge of these processes is high for aHGGs, they behave differently and have different genetic profiles compared to pHGGs. It is therefore inappropriate to extrapolate therapeutic strategies for the pediatric population. The studies in this dissertation are the first of their kind. They establish the basic knowledge pHGGs possess infiltrating macrophages whose infiltration is encouraged by PDGFB signaling. Further, they demonstrate how different genetic driver mutations and tumor locations affect the TME and immune infiltrate. More studies are needed before we can develop effective targeted therapies, however, a foundation has been formed and it must be utilized in all studies moving forward.

Sample ID	Diagnosis	Tumor Location	Age at Diagnosis (Months)	Survival (Weeks since diagnosis)	Sex	Treatment	Molecular Characteristics	NanoString?
PGBM 1	DIPG	Pons	69.87	47.00	F	-	-	Y
PGBM 2	DIPG	Pons	40.83	94.29	F	-	-	Y
PGBM 3	AA	Temporal, left	112.77	43.14	M	-	PIK3CA:p.H1047R mut. Loss of CDKN2A	Y
PGBM 4	AA	Pons, lateral	114.80	65.86	M	-	EGFR amp, CDK6 amp	Y
PGBM 5	GBM	Basal ganglia, right	6.50	29.57	F	-	-	Y
PGBM 6	GBM	Frontal, right	145.33	40.43	M	-	PIK3CA:p.H1047R mut. Loss of CDKN2A	Y
PGBM 7	DIPG	Pons	76.00	34.57	F	-	-	N
PGBM 8	DIPG	Pons	119.27	59.14	F	-	-	N
PGBM 9	GBM	Pons	41.60	48.86	F	-	-	N
PGBM 10	DIPG	Pons	55.53	85.43	F	-	-	Y
PGBM 11	GBM	Frontal, right	203.30	20.29	M	-	MET-PTPRZ1 gene fusion	Y
PGBM 12	GBM	Pons	88.03	76.86	M	-	-	Y
PGBM 13	GBM	Temporal, left	141.67	67.71	M	Radiation	-	Y
PGBM 14	GBM-K27M	-	0.00	0.00	-	-	K27M	N
PGBM 15	AA-G34R	Temporal, Left	206.27	alive	F	-	H3-G34R & TP53 mutations	Y
PGBM 16	Thalamic K27M	Thalamus/frontal, right	187.50	15.14	M	-	K27M	Y
PGBM 17	DIPG-K27M	Pons	48.93	155.86	M	-	K27M	N
PGBM 18	DIPG-K27M	Pons	149.20	249.43	F	-	K27M	N
PGBM 19	GBM	Parietal, right	194.87	31.29	M	Radiation	-	Y
PGBM 20	GBM	Parietal, right	164.93	45.86	F	Radiation	-	Y
PGBM 21	GBM-K27M	Thalamus, left	67.13	41.00	M	-	K27M	Y
PGBM 22	GBM	Frontal, right	183.33	alive	M	Radiation,	-	Y
PGBM 23	GBM	Temporal, left	204.60	283.43	M	Radiation, complex	-	Y
PGBM 24	GBM	Temporal, left	173.73	84.43	M	-	EGFR amp, PTEN loss	Y
PGBM 25	GBM-K27M	Thalamus, left	179.23	75.14	M	-	K27M	Y
PGBM 26	GBM-G34R	Temporal, left	157.37	126.29	M	-	H3 G34R	Y
PGBM 27	GBM	Right	60.00	9.00	M	-	Amp. MYCN, ampMDM4, ampMIR205	N
PGBM 28	GBM	Right frontoparietal	60.00	17.00	M	-	EGFR amp, CDK6 amp	N
PGBM 29	Anaplastic Ependymoma III	Right hemisphere	180.00	24.00	F	-	-	N
PGBM 30	AA III/IV-G34R/V	Temporal, right	120.00	25.00	M	-	H3 G34V, P53 mut, EGFR gain, CDK6 gain, MET gain, MYCN gain, CDKN2A gain, PTCH1 gain	N
PGBM 31	GBM	Left frontal lobe	60	7	F	-	-	N
PGBM 32	GBM	Left frontal lobe	144	16	M	-	EGFR, TERT, PIK3CA mutations, CDKN2A loss	N
PGBM 33	GBM	Left CP angle near pons	96	11	F	-	-	N
PGBM 34	DIPG	Pons	47.00	152.08	-	-	K27M	N
PGBM 35	DIPG	Pons	39.00	91.25	-	-	K27M	N
PGBM 36	DIPG	Pons	68.00	43.45	-	-	K27M unknown	N
PGBM 37	DIPG	Pons	54.00	82.55	-	-	K27M unknown	N
PGBM 38	DIPG	Pons	146.00	247.67	-	-	K27M	N
PGBM 39	GBM-K27M	Right	-	-	M	-	-	N
PGBM 40	GBM-G34R	Temporo-parietal, right	254.40	alive	M	-	G34R	Y
PGBM 41	AA	Pons	161.90	45.29	M	-	-	N
PGBM 42	AA	Right hemisphere, thalami	213.23	alive	M	-	-	N
PGBM 43	GBM-K27M	Thalamus, right	140.40	79.14	F	-	K27M	N
PGBM 44	DIPG-K27M	Pons	157.20	alive	M	-	K27M	N
PGBM 45	DIPG/GBM	Pons	143.77	453.29	M	-	Not K27M	Y
PGBM 46	AA-K27M	Thalami	201.37	59	F	-	K27M	N
PGBM 48	GBM-K27M						K27M	Y

Table 1. Patient Characteristics. Each human pHGG tissue sample used in the study is described with their diagnosis, tumor location, age at diagnosis, survival weeks, sex, treatment history, molecular characteristics, and whether they were used for NanoString.

Primer	Bio-Rad Catalog Number	Primer	Bio-Rad Catalog Number
Actb	qMmuCED0027505	Pd1	qMmuCID0011570
Cdc20	qMmuCED0005008	Ccr5	qMmuCID0020341
Dll3	qMmuCID0023659	Cd44	qMmuCID0025677
Tgfb2	qMmuCID0024408	Met	qMmuCID0017026
Yap1	qMmuCID0005990	Ccl7	qMmuCED0049027
Mgmt	qMmuCID0009593	Il2	qMmuCED0060978
Ccr8	qMmuCID0006837	Pdl1	qMmuCID0011907
Ctla4	qMmuCID0008808	Pdgfa	qHsaCID0005879
Sox2	qMmuCED0051857	Ccl8	qMmuCED0003781
Oct4	qMmuCED0046525	Ccl5	qMmuCID0021047
Musashi	qMmuCID0040186	Vegfa	qMmuCED0040260
Nanog	qMmuCID0005399	Nestin	qMmuCID0023067
Stat3	qMmuCID0021132	Spp1	qMmuCED0061675
Ccnd2	qMmuCID0023538	Cxcr4	qMmuCED0026325
Cxcr4	qMmuCED0026325	Cxcl12	qMmuCID0019961
Kdr	qMmuCID0005890	Cd8a	qMmuCID0016523
Ncam1	qMmuCID0005870	Foxp3	qMmuCID0022414
Ccl3	qMmuCED0003870	Lbp	qMmuCED0045303
Chi3l1	qMmuCID0015758	Cfh	qMmuCED0045575
Serpine1	qMmuCID0027303	Lrrn3	qMmuCID0019276
Pdgfb	qHsaCID0016004	Csf1r	qMmuCID0016567
Il1a	qMmuCID0005637	Ccl11	qMmuCED0044849
Pf4	qMmuCED0003895	Selplg	qMmuCED0050109
Tgfb1	qMmuCID0017320	Ly86	qMmuCED0045007
Marco	qMmuCID0023893	Itgam	qMmuCID0005971
Csf2	qMmuCED0025728	Pdcd1lg2	qMmuCID0011922
P2ry12	qMmuCID0015382	Ido1	qMmuCED0047121
Vgf	qMmuCED0049363	Cd200	qMmuCED0045566
Gfap	qMmuCID0020163	Tnfa	qMmuCED0004141
Aif1	qMmuCED0046745	Ifng	qMmuCID0006268
Il1b	qMmuCID0005641	Cd47	qMmuCED0049651
Ccr1	qMmuCID0006862	Arg1	qMmuCID0022400
Ccl2	qMmuCED0048300	Cd3e	qMmuCED0047615
Ccl1	qMmuCED0038249	Cd8a	qMmuCID0016523
Olig2	qMmuCED0003760	Cd4	qMmuCID0022320
Cebpb	qMmuCED0050360	Cd68	qMmuCED0003822
Ccr1	qMmuCID0006862	Cd45 (Ptprc)	qMmuCID0039693
Ccl12	qMmuCED0061017	Cd163	qMmuCID0012017

Table 2. qPCR Primers Used in Study. The Bio-Rad qPCR primers used in the study are listed with their catalog numbers.

References

1. Q. T. Ostrom *et al.*, Alex's Lemonade Stand Foundation Infant and Childhood Primary Brain and Central Nervous System Tumors Diagnosed in the United States in 2007-2011. *Neuro Oncol* **16 Suppl 10**, x1-x36 (2015).
2. Q. T. Ostrom, J. S. Barnholtz-Sloan, Current state of our knowledge on brain tumor epidemiology. *Curr Neurol Neurosci Rep* **11**, 329-335 (2011).
3. T. P. Diwanji, A. Engelman, J. W. Snider, P. Mohindra, Epidemiology, diagnosis, and optimal management of glioma in adolescents and young adults. *Adolesc Health Med Ther* **8**, 99-113 (2017).
4. Q. T. Ostrom *et al.*, American Brain Tumor Association Adolescent and Young Adult Primary Brain and Central Nervous System Tumors Diagnosed in the United States in 2008-2012. *Neuro Oncol* **18 Suppl 1**, i1-i50 (2016).
5. J. A. Schwartzbaum, J. L. Fisher, K. D. Aldape, M. Wrensch, Epidemiology and molecular pathology of glioma. *Nat Clin Pract Neurol* **2**, 494-503; quiz 491 p following 516 (2006).
6. S. Braunstein, D. Raleigh, R. Bindra, S. Mueller, D. Haas-Kogan, Pediatric high-grade glioma: current molecular landscape and therapeutic approaches. *J Neurooncol* **134**, 541-549 (2017).
7. A. P. Kyritsis, M. L. Bondy, J. S. Rao, C. Sioka, Inherited predisposition to glioma. *Neuro Oncol* **12**, 104-113 (2010).
8. J. L. Ross *et al.*, 5-Aminolevulinic Acid Guided Sampling of Glioblastoma Microenvironments Identifies Pro-Survival Signaling at Infiltrative Margins. *Sci Rep* **7**, 15593 (2017).
9. A. Mackay *et al.*, Molecular, Pathological, Radiological, and Immune Profiling of Non-brainstem Pediatric High-Grade Glioma from the HERBY Phase II Randomized Trial. *Cancer Cell* **33**, 829-842 e825 (2018).
10. A. Mackay *et al.*, Integrated Molecular Meta-Analysis of 1,000 Pediatric High-Grade and Diffuse Intrinsic Pontine Glioma. *Cancer Cell* **32**, 520-537 e525 (2017).
11. C. Koschmann *et al.*, Characterizing and targeting PDGFRA alterations in pediatric high-grade glioma. *Oncotarget* **7**, 65696-65706 (2016).
12. B. S. Paugh *et al.*, Integrated molecular genetic profiling of pediatric high-grade gliomas reveals key differences with the adult disease. *J Clin Oncol* **28**, 3061-3068 (2010).
13. R. G. Verhaak *et al.*, Integrated genomic analysis identifies clinically relevant subtypes of glioblastoma characterized by abnormalities in PDGFRA, IDH1, EGFR, and NF1. *Cancer Cell* **17**, 98-110 (2010).
14. C. W. Brennan *et al.*, The somatic genomic landscape of glioblastoma. *Cell* **155**, 462-477 (2013).
15. N. Cancer Genome Atlas Research, Comprehensive genomic characterization defines human glioblastoma genes and core pathways. *Nature* **455**, 1061-1068 (2008).
16. M. Nakamura *et al.*, Molecular pathogenesis of pediatric astrocytic tumors. *Neuro Oncol* **9**, 113-123 (2007).
17. G. Wu *et al.*, The genomic landscape of diffuse intrinsic pontine glioma and pediatric non-brainstem high-grade glioma. *Nat Genet* **46**, 444-450 (2014).
18. D. Sturm, S. M. Pfister, D. T. W. Jones, Pediatric Gliomas: Current Concepts on Diagnosis, Biology, and Clinical Management. *J Clin Oncol* **35**, 2370-2377 (2017).

19. G. Wu *et al.*, Somatic histone H3 alterations in pediatric diffuse intrinsic pontine gliomas and non-brainstem glioblastomas. *Nat Genet* **44**, 251-253 (2012).
20. J. Schwartzentruber *et al.*, Driver mutations in histone H3.3 and chromatin remodelling genes in paediatric glioblastoma. *Nature* **482**, 226-231 (2012).
21. D. A. Solomon *et al.*, Diffuse Midline Gliomas with Histone H3-K27M Mutation: A Series of 47 Cases Assessing the Spectrum of Morphologic Variation and Associated Genetic Alterations. *Brain Pathol* **26**, 569-580 (2016).
22. D. N. Louis *et al.*, The 2016 World Health Organization Classification of Tumors of the Central Nervous System: a summary. *Acta Neuropathol* **131**, 803-820 (2016).
23. C. Jones, S. J. Baker, Unique genetic and epigenetic mechanisms driving paediatric diffuse high-grade glioma. *Nat Rev Cancer* **14** (2014).
24. A. K. Diaz, S. J. Baker, The genetic signatures of pediatric high-grade glioma: no longer a one-act play. *Semin Radiat Oncol* **24**, 240-247 (2014).
25. I. F. Pollack *et al.*, Expression of p53 and prognosis in children with malignant gliomas. *N Engl J Med* **346**, 420-427 (2002).
26. K. J. Cohen *et al.*, Temozolomide in the treatment of high-grade gliomas in children: a report from the Children's Oncology Group. *Neuro Oncol* **13**, 317-323 (2011).
27. H. S. Nicholson *et al.*, Phase 2 study of temozolomide in children and adolescents with recurrent central nervous system tumors: a report from the Children's Oncology Group. *Cancer* **110**, 1542-1550 (2007).
28. J. Fangusaro, Pediatric high grade glioma: a review and update on tumor clinical characteristics and biology. *Front Oncol* **2**, 105 (2012).
29. K. E. Warren, Diffuse intrinsic pontine glioma: poised for progress. *Front Oncol* **2**, 205 (2012).
30. P. Guerra-Garcia *et al.*, Challenging the indiscriminate use of temozolomide in pediatric high-grade gliomas: A review of past, current, and emerging therapies. *Pediatr Blood Cancer* 10.1002/pbc.28011, e28011 (2019).
31. T. Yang *et al.*, Gross total resection correlates with long-term survival in pediatric patients with glioblastoma. *World Neurosurg* **79**, 537-544 (2013).
32. C. M. Kramm *et al.*, Improved survival after gross total resection of malignant gliomas in pediatric patients from the HIT-GBM studies. *Anticancer Res* **26**, 3773-3779 (2006).
33. L. S. Lashford *et al.*, Temozolomide in malignant gliomas of childhood: a United Kingdom Children's Cancer Study Group and French Society for Pediatric Oncology Intergroup Study. *J Clin Oncol* **20**, 4684-4691 (2002).
34. J. Grill *et al.*, Phase II, Open-Label, Randomized, Multicenter Trial (HERBY) of Bevacizumab in Pediatric Patients With Newly Diagnosed High-Grade Glioma. *J Clin Oncol* **36**, 951-958 (2018).
35. N. Gaspar *et al.*, MGMT-independent temozolomide resistance in pediatric glioblastoma cells associated with a PI3-kinase-mediated HOX/stem cell gene signature. *Cancer Res* **70**, 9243-9252 (2010).
36. A. S. Chi *et al.*, Pediatric and adult H3 K27M-mutant diffuse midline glioma treated with the selective DRD2 antagonist ONC201. *J Neurooncol* **145**, 97-105 (2019).
37. M. D. Hall *et al.*, First clinical experience with DRD2/3 antagonist ONC201 in H3 K27M-mutant pediatric diffuse intrinsic pontine glioma: a case report. *J Neurosurg Pediatr* 10.3171/2019.2.PEDS18480, 1-7 (2019).

38. E. Bouffet *et al.*, Immune Checkpoint Inhibition for Hypermutant Glioblastoma Multiforme Resulting From Germline Biallelic Mismatch Repair Deficiency. *J Clin Oncol* **34**, 2206-2211 (2016).
39. S. Tejada *et al.*, Phase I Trial of DNX-2401 for Diffuse Intrinsic Pontine Glioma Newly Diagnosed in Pediatric Patients. *Neurosurgery* **83**, 1050-1056 (2018).
40. J. L. Lasky, 3rd *et al.*, Autologous tumor lysate-pulsed dendritic cell immunotherapy for pediatric patients with newly diagnosed or recurrent high-grade gliomas. *Anticancer Res* **33**, 2047-2056 (2013).
41. M. M. Souweidane *et al.*, Convection-enhanced delivery for diffuse intrinsic pontine glioma: a single-centre, dose-escalation, phase 1 trial. *Lancet Oncol* **19**, 1040-1050 (2018).
42. P. M. Foreman, G. K. Friedman, K. A. Cassady, J. M. Markert, Oncolytic Virotherapy for the Treatment of Malignant Glioma. *Neurotherapeutics* **14**, 333-344 (2017).
43. C. H. Heldin, J. Lennartsson, B. Westermark, Involvement of platelet-derived growth factor ligands and receptors in tumorigenesis. *J Intern Med* **283**, 16-44 (2018).
44. P. H. Chen, V. Unger, X. He, Structure of Full-Length Human PDGFRbeta Bound to Its Activating Ligand PDGF-B as Determined by Negative-Stain Electron Microscopy. *J Mol Biol* **427**, 3921-3934 (2015).
45. A. H. Shim *et al.*, Structures of a platelet-derived growth factor/propeptide complex and a platelet-derived growth factor/receptor complex. *Proc Natl Acad Sci U S A* **107**, 11307-11312 (2010).
46. Y. Wang, S. D. Pennock, X. Chen, A. Kazlauskas, Z. Wang, Platelet-derived growth factor receptor-mediated signal transduction from endosomes. *J Biol Chem* **279**, 8038-8046 (2004).
47. W. J. Fantl *et al.*, Distinct phosphotyrosines on a growth factor receptor bind to specific molecules that mediate different signaling pathways. *Cell* **69**, 413-423 (1992).
48. A. Jurek, C. H. Heldin, J. Lennartsson, Platelet-derived growth factor-induced signaling pathways interconnect to regulate the temporal pattern of Erk1/2 phosphorylation. *Cell Signal* **23**, 280-287 (2011).
49. B. Westermark, C. H. Heldin, M. Nister, Platelet-derived growth factor in human glioma. *Glia* **15**, 257-263 (1995).
50. E. Wu *et al.*, Comprehensive dissection of PDGF-PDGFR signaling pathways in PDGFR genetically defined cells. *PLoS One* **3**, e3794 (2008).
51. K. W. Liu, B. Hu, S. Y. Cheng, Platelet-derived growth factor receptor alpha in glioma: a bad seed. *Chin J Cancer* **30**, 590-602 (2011).
52. C. H. Heldin, B. Westermark, Mechanism of action and in vivo role of platelet-derived growth factor. *Physiol Rev* **79**, 1283-1316 (1999).
53. W. D. Richardson, N. Pringle, M. J. Mosley, B. Westermark, M. Dubois-Dalcq, A role for platelet-derived growth factor in normal gliogenesis in the central nervous system. *Cell* **53**, 309-319 (1988).
54. N. P. Pringle, H. S. Mudhar, E. J. Collarini, W. D. Richardson, PDGF receptors in the rat CNS: during late neurogenesis, PDGF alpha-receptor expression appears to be restricted to glial cells of the oligodendrocyte lineage. *Development* **115**, 535-551 (1992).
55. P. Soriano, The PDGF alpha receptor is required for neural crest cell development and for normal patterning of the somites. *Development* **124**, 2691-2700 (1997).

56. K. Morrison-Graham, G. C. Schatteman, T. Bork, D. F. Bowen-Pope, J. A. Weston, A PDGF receptor mutation in the mouse (Patch) perturbs the development of a non-neuronal subset of neural crest-derived cells. *Development* **115**, 133-142 (1992).
57. M. Fruttiger, A. R. Calver, W. D. Richardson, Platelet-derived growth factor is constitutively secreted from neuronal cell bodies but not from axons. *Curr Biol* **10**, 1283-1286 (2000).
58. M. Noble, K. Murray, P. Stroobant, M. D. Waterfield, P. Riddle, Platelet-derived growth factor promotes division and motility and inhibits premature differentiation of the oligodendrocyte/type-2 astrocyte progenitor cell. *Nature* **333**, 560-562 (1988).
59. H. J. Yeh *et al.*, PDGF A-chain gene is expressed by mammalian neurons during development and in maturity. *Cell* **64**, 209-216 (1991).
60. W. Baron, S. J. Shattil, C. ffrench-Constant, The oligodendrocyte precursor mitogen PDGF stimulates proliferation by activation of alpha(v)beta3 integrins. *EMBO J* **21**, 1957-1966 (2002).
61. M. Fruttiger *et al.*, Defective oligodendrocyte development and severe hypomyelination in PDGF-A knockout mice. *Development* **126**, 457-467 (1999).
62. A. R. Calver *et al.*, Oligodendrocyte population dynamics and the role of PDGF in vivo. *Neuron* **20**, 869-882 (1998).
63. L. E. Olson, P. Soriano, Increased PDGFRalpha activation disrupts connective tissue development and drives systemic fibrosis. *Dev Cell* **16**, 303-313 (2009).
64. M. Puputti *et al.*, Amplification of KIT, PDGFRA, VEGFR2, and EGFR in gliomas. *Mol Cancer Res* **4**, 927-934 (2006).
65. A. H. Shih *et al.*, Dose-dependent effects of platelet-derived growth factor-B on glial tumorigenesis. *Cancer Res* **64**, 4783-4789 (2004).
66. K. Hosaka *et al.*, Pericyte-fibroblast transition promotes tumor growth and metastasis. *Proc Natl Acad Sci U S A* **113**, E5618-5627 (2016).
67. E. I. Fomchenko, E. C. Holland, Platelet-derived growth factor-mediated gliomagenesis and brain tumor recruitment. *Neurosurg Clin N Am* **18**, 39-58, viii (2007).
68. M. Hellstrom, M. Kalen, P. Lindahl, A. Abramsson, C. Betsholtz, Role of PDGF-B and PDGFR-beta in recruitment of vascular smooth muscle cells and pericytes during embryonic blood vessel formation in the mouse. *Development* **126**, 3047-3055 (1999).
69. C. H. Heldin, J. Lennartsson, Structural and functional properties of platelet-derived growth factor and stem cell factor receptors. *Cold Spring Harb Perspect Biol* **5**, a009100 (2013).
70. H. Gerhardt *et al.*, VEGF guides angiogenic sprouting utilizing endothelial tip cell filopodia. *J Cell Biol* **161**, 1163-1177 (2003).
71. P. Leveen *et al.*, Mice deficient for PDGF B show renal, cardiovascular, and hematological abnormalities. *Genes Dev* **8**, 1875-1887 (1994).
72. P. Soriano, Abnormal kidney development and hematological disorders in PDGF beta-receptor mutant mice. *Genes Dev* **8**, 1888-1896 (1994).
73. P. Lindahl, B. R. Johansson, P. Leveen, C. Betsholtz, Pericyte loss and microaneurysm formation in PDGF-B-deficient mice. *Science* **277**, 242-245 (1997).
74. J. Andrae, R. Gallini, C. Betsholtz, Role of platelet-derived growth factors in physiology and medicine. *Genes Dev* **22**, 1276-1312 (2008).
75. N. Papadopoulos, J. Lennartsson, The PDGF/PDGFR pathway as a drug target. *Mol Aspects Med* **62**, 75-88 (2018).

76. W. E. Kaminski *et al.*, Basis of hematopoietic defects in platelet-derived growth factor (PDGF)-B and PDGF beta-receptor null mice. *Blood* **97**, 1990-1998 (2001).
77. F. Calzolari, P. Malatesta, Recent insights into PDGF-induced gliomagenesis. *Brain Pathol* **20**, 527-538 (2010).
78. I. Appolloni *et al.*, PDGF-B induces a homogeneous class of oligodendrogliomas from embryonic neural progenitors. *Int J Cancer* **124**, 2251-2259 (2009).
79. T. Mapstone, M. McMichael, D. Goldthwait, Expression of platelet-derived growth factors, transforming growth factors, and the ros gene in a variety of primary human brain tumors. *Neurosurgery* **28**, 216-222 (1991).
80. T. Inaba *et al.*, Expression of platelet-derived growth factor beta receptor on human monocyte-derived macrophages and effects of platelet-derived growth factor BB dimer on the cellular function. *J Biol Chem* **268**, 24353-24360 (1993).
81. P. Yang *et al.*, Role of PDGF-D and PDGFR-beta in neuroinflammation in experimental ICH mice model. *Exp Neurol* **283**, 157-164 (2016).
82. B. Fuhrman *et al.*, Urokinase activates macrophage PON2 gene transcription via the PI3K/ROS/MEK/SREBP-2 signalling cascade mediated by the PDGFR-beta. *Cardiovasc Res* **84**, 145-154 (2009).
83. C. He *et al.*, PDGFRbeta signalling regulates local inflammation and synergizes with hypercholesterolaemia to promote atherosclerosis. *Nat Commun* **6**, 7770 (2015).
84. T. Birnbaum *et al.*, Malignant gliomas actively recruit bone marrow stromal cells by secreting angiogenic cytokines. *J Neurooncol* **83**, 241-247 (2007).
85. Y. Hu, P. Cheng, J. C. Ma, Y. X. Xue, Y. H. Liu, Platelet-derived growth factor BB mediates the glioma-induced migration of bone marrow-derived mesenchymal stem cells by promoting the expression of vascular cell adhesion molecule-1 through the PI3K, P38 MAPK and NF-kappaB pathways. *Oncol Rep* **30**, 2755-2764 (2013).
86. J. B. Demoulin, A. Essaghir, PDGF receptor signaling networks in normal and cancer cells. *Cytokine Growth Factor Rev* **25**, 273-283 (2014).
87. Y. Cao, Direct role of PDGF-BB in lymphangiogenesis and lymphatic metastasis. *Cell Cycle* **4**, 228-230 (2005).
88. D. Singh *et al.*, Gene expression correlates of clinical prostate cancer behavior. *Cancer Cell* **1**, 203-209 (2002).
89. Y. Nordby *et al.*, High expression of PDGFR-beta in prostate cancer stroma is independently associated with clinical and biochemical prostate cancer recurrence. *Sci Rep* **7**, 43378 (2017).
90. B. Bhardwaj *et al.*, Localization of platelet-derived growth factor beta receptor expression in the periepithelial stroma of human breast carcinoma. *Clin Cancer Res* **2**, 773-782 (1996).
91. A. S. Tsao *et al.*, Immunohistochemical overexpression of platelet-derived growth factor receptor-beta (PDGFR-beta) is associated with PDGFRB gene copy number gain in sarcomatoid non-small-cell lung cancer. *Clin Lung Cancer* **12**, 369-374 (2011).
92. C. Criscitiello, G. Viale, A. Esposito, G. Curigliano, Dinaciclib for the treatment of breast cancer. *Expert Opin Investig Drugs* **23**, 1305-1312 (2014).
93. J. Paulsson *et al.*, High expression of stromal PDGFRbeta is associated with reduced benefit of tamoxifen in breast cancer. *J Pathol Clin Res* **3**, 38-43 (2017).

94. Y. Jiang, M. Boije, B. Westermark, L. Uhrbom, PDGF-B Can sustain self-renewal and tumorigenicity of experimental glioma-derived cancer-initiating cells by preventing oligodendrocyte differentiation. *Neoplasia* **13**, 492-503 (2011).
95. Z. Chen *et al.*, Cellular and Molecular Identity of Tumor-Associated Macrophages in Glioblastoma. *Cancer Res* **77**, 2266-2278 (2017).
96. Z. Chen, D. Hambardzumyan, Immune Microenvironment in Glioblastoma Subtypes. *Front Immunol* **9**, 1004 (2018).
97. D. Hambardzumyan, D. H. Gutmann, H. Kettenmann, The role of microglia and macrophages in glioma maintenance and progression. *Nat Neurosci* **19**, 20-27 (2016).
98. X. Z. Ye *et al.*, Tumor-associated microglia/macrophages enhance the invasion of glioma stem-like cells via TGF-beta1 signaling pathway. *J Immunol* **189**, 444-453 (2012).
99. D. Hambardzumyan, G. Bergers, Glioblastoma: Defining Tumor Niches. *Trends Cancer* **1**, 252-265 (2015).
100. S. Muller *et al.*, Single-cell profiling of human gliomas reveals macrophage ontogeny as a basis for regional differences in macrophage activation in the tumor microenvironment. *Genome Biol* **18**, 234 (2017).
101. M. Massara *et al.*, Neutrophils in Gliomas. *Front Immunol* **8**, 1349 (2017).
102. D. F. Quail, J. A. Joyce, The Microenvironmental Landscape of Brain Tumors. *Cancer Cell* **31**, 326-341 (2017).
103. D. I. Gabrilovich, S. Ostrand-Rosenberg, V. Bronte, Coordinated regulation of myeloid cells by tumours. *Nat Rev Immunol* **12**, 253-268 (2012).
104. F. Ginhoux *et al.*, Fate mapping analysis reveals that adult microglia derive from primitive macrophages. *Science* **330**, 841-845 (2010).
105. B. Ajami, J. L. Bennett, C. Krieger, W. Tetzlaff, F. M. Rossi, Local self-renewal can sustain CNS microglia maintenance and function throughout adult life. *Nat Neurosci* **10**, 1538-1543 (2007).
106. H. Kettenmann, U. K. Hanisch, M. Noda, A. Verkhratsky, Physiology of microglia. *Physiol Rev* **91**, 461-553 (2011).
107. C. K. Donat, G. Scott, S. M. Gentleman, M. Sastre, Microglial Activation in Traumatic Brain Injury. *Front Aging Neurosci* **9**, 208 (2017).
108. K. Gabrusiewicz *et al.*, Glioblastoma-infiltrated innate immune cells resemble M0 macrophage phenotype. *JCI Insight* **1** (2016).
109. C. Ricard *et al.*, Phenotypic dynamics of microglial and monocyte-derived cells in glioblastoma-bearing mice. *Sci Rep* **6**, 26381 (2016).
110. C. Ricard, F. C. Debarbieux, Six-color intravital two-photon imaging of brain tumors and their dynamic microenvironment. *Front Cell Neurosci* **8**, 57 (2014).
111. C. Ricard *et al.*, Dynamic quantitative intravital imaging of glioblastoma progression reveals a lack of correlation between tumor growth and blood vessel density. *PLoS One* **8**, e72655 (2013).
112. M. Osswald *et al.*, Brain tumour cells interconnect to a functional and resistant network. *Nature* **528**, 93-98 (2015).
113. A. Nimmerjahn, F. Kirchhoff, F. Helmchen, Resting microglial cells are highly dynamic surveillants of brain parenchyma in vivo. *Science* **308**, 1314-1318 (2005).
114. M. E. Tremblay, C. Lecours, L. Samson, V. Sanchez-Zafra, A. Sierra, From the Cajal alumni Achucarro and Rio-Hortega to the rediscovery of never-resting microglia. *Front Neuroanat* **9**, 45 (2015).

115. J. Meller *et al.*, Integrin-Kindlin3 requirements for microglial motility in vivo are distinct from those for macrophages. *JCI Insight* **2** (2017).
116. B. A. Castro *et al.*, Macrophage migration inhibitory factor downregulation: a novel mechanism of resistance to anti-angiogenic therapy. *Oncogene* **36**, 3749-3759 (2017).
117. Y. Piao *et al.*, Glioblastoma resistance to anti-VEGF therapy is associated with myeloid cell infiltration, stem cell accumulation, and a mesenchymal phenotype. *Neuro Oncol* **14**, 1379-1392 (2012).
118. J. Kloepper *et al.*, Ang-2/VEGF bispecific antibody reprograms macrophages and resident microglia to anti-tumor phenotype and prolongs glioblastoma survival. *Proc Natl Acad Sci U S A* **113**, 4476-4481 (2016).
119. A. Scholz *et al.*, Endothelial cell-derived angiopoietin-2 is a therapeutic target in treatment-naive and bevacizumab-resistant glioblastoma. *EMBO Mol Med* **8**, 39-57 (2016).
120. K. L. Pitter *et al.*, Corticosteroids compromise survival in glioblastoma. *Brain* **139**, 1458-1471 (2016).
121. R. Du *et al.*, HIF1alpha induces the recruitment of bone marrow-derived vascular modulatory cells to regulate tumor angiogenesis and invasion. *Cancer Cell* **13**, 206-220 (2008).
122. F. Shojaei *et al.*, G-CSF-initiated myeloid cell mobilization and angiogenesis mediate tumor refractoriness to anti-VEGF therapy in mouse models. *Proc Natl Acad Sci U S A* **106**, 6742-6747 (2009).
123. S. C. Wang, J. H. Hong, C. Hsueh, C. S. Chiang, Tumor-secreted SDF-1 promotes glioma invasiveness and TAM tropism toward hypoxia in a murine astrocytoma model. *Lab Invest* **92**, 151-162 (2012).
124. S. Brandenburg *et al.*, Resident microglia rather than peripheral macrophages promote vascularization in brain tumors and are source of alternative pro-angiogenic factors. *Acta Neuropathol* **131**, 365-378 (2016).
125. X. Chen *et al.*, RAGE expression in tumor-associated macrophages promotes angiogenesis in glioma. *Cancer Res* **74**, 7285-7297 (2014).
126. J. Neumann *et al.*, Beware the intruder: Real time observation of infiltrated neutrophils and neutrophil-Microglia interaction during stroke in vivo. *PLoS One* **13**, e0193970 (2018).
127. A. E. Cardona *et al.*, Control of microglial neurotoxicity by the fractalkine receptor. *Nat Neurosci* **9**, 917-924 (2006).
128. K. Bhaskar *et al.*, Regulation of tau pathology by the microglial fractalkine receptor. *Neuron* **68**, 19-31 (2010).
129. K. A. Jones *et al.*, Peripheral immune cells infiltrate into sites of secondary neurodegeneration after ischemic stroke. *Brain Behav Immun* **67**, 299-307 (2018).
130. A. von Werder, B. Seidler, R. M. Schmid, G. Schneider, D. Saur, Production of avian retroviruses and tissue-specific somatic retroviral gene transfer in vivo using the RCAS/TVA system. *Nat Protoc* **7**, 1167-1183 (2012).
131. L. G. Ahronian, B. C. Lewis, Using the RCAS-TVA system to model human cancer in mice. *Cold Spring Harb Protoc* **2014**, 1128-1135 (2014).
132. D. Hambardzumyan, N. M. Amankulor, K. Y. Helmy, O. J. Becher, E. C. Holland, Modeling Adult Gliomas Using RCAS/t-va Technology. *Transl Oncol* **2**, 89-95 (2009).

133. C. J. Herting *et al.*, Genetic driver mutations define the expression signature and microenvironmental composition of high-grade gliomas. *Glia* **65**, 1914-1926 (2017).
134. N. A. P. Lieberman *et al.*, Characterization of the immune microenvironment of diffuse intrinsic pontine glioma: implications for development of immunotherapy. *Neuro Oncol* **21**, 83-94 (2019).
135. A. M. Griesinger, A. M. Donson, N. K. Foreman, Immunotherapeutic implications of the immunophenotype of pediatric brain tumors. *Oncoimmunology* **3**, e27256 (2014).
136. A. S. Plant *et al.*, Immunophenotyping of pediatric brain tumors: correlating immune infiltrate with histology, mutational load, and survival and assessing clonal T cell response. *J Neurooncol* **137**, 269-278 (2018).
137. G. L. Lin *et al.*, Non-inflammatory tumor microenvironment of diffuse intrinsic pontine glioma. *Acta Neuropathol Commun* **6**, 51 (2018).
138. M. S. Rooney, S. A. Shukla, C. J. Wu, G. Getz, N. Hacohen, Molecular and genetic properties of tumors associated with local immune cytolytic activity. *Cell* **160**, 48-61 (2015).
139. C. Schinke *et al.*, IL8-CXCR2 pathway inhibition as a therapeutic strategy against MDS and AML stem cells. *Blood* **125**, 3144-3152 (2015).
140. K. De Filippo *et al.*, Mast cell and macrophage chemokines CXCL1/CXCL2 control the early stage of neutrophil recruitment during tissue inflammation. *Blood* **121**, 4930-4937 (2013).
141. J. Li *et al.*, Tumor Cell-Intrinsic Factors Underlie Heterogeneity of Immune Cell Infiltration and Response to Immunotherapy. *Immunity* **49**, 178-193 e177 (2018).
142. R. Parente, S. J. Clark, A. Inforzato, A. J. Day, Complement factor H in host defense and immune evasion. *Cell Mol Life Sci* **74**, 1605-1624 (2017).
143. A. M. Lesokhin *et al.*, Monocytic CCR2(+) myeloid-derived suppressor cells promote immune escape by limiting activated CD8 T-cell infiltration into the tumor microenvironment. *Cancer Res* **72**, 876-886 (2012).
144. A. D. Barrow *et al.*, Natural Killer Cells Control Tumor Growth by Sensing a Growth Factor. *Cell* **172**, 534-548 e519 (2018).
145. A. L. Chang *et al.*, CCL2 Produced by the Glioma Microenvironment Is Essential for the Recruitment of Regulatory T Cells and Myeloid-Derived Suppressor Cells. *Cancer Res* **76**, 5671-5682 (2016).
146. N. Unver, Macrophage chemoattractants secreted by cancer cells: Sculptors of the tumor microenvironment and another crucial piece of the cancer secretome as a therapeutic target. *Cytokine Growth Factor Rev* 10.1016/j.cytogfr.2019.05.010 (2019).
147. L. Cassetta *et al.*, Human Tumor-Associated Macrophage and Monocyte Transcriptional Landscapes Reveal Cancer-Specific Reprogramming, Biomarkers, and Therapeutic Targets. *Cancer Cell* **35**, 588-602 e510 (2019).
148. H. Shi *et al.*, Recruited monocytic myeloid-derived suppressor cells promote the arrest of tumor cells in the premetastatic niche through an IL-1beta-mediated increase in E-selectin expression. *Int J Cancer* **140**, 1370-1383 (2017).
149. T. H. Schaller, K. A. Batich, C. M. Suryadevara, R. Desai, J. H. Sampson, Chemokines as adjuvants for immunotherapy: implications for immune activation with CCL3. *Expert Rev Clin Immunol* **13**, 1049-1060 (2017).

150. G. Davatelis *et al.*, Cloning and characterization of a cDNA for murine macrophage inflammatory protein (MIP), a novel monokine with inflammatory and chemokinetic properties. *J Exp Med* **167**, 1939-1944 (1988).
151. D. A. Mitchell *et al.*, Tetanus toxoid and CCL3 improve dendritic cell vaccines in mice and glioblastoma patients. *Nature* **519**, 366-369 (2015).
152. F. Castellino *et al.*, Chemokines enhance immunity by guiding naive CD8+ T cells to sites of CD4+ T cell-dendritic cell interaction. *Nature* **440**, 890-895 (2006).
153. D. Y. Vogel *et al.*, Macrophages in inflammatory multiple sclerosis lesions have an intermediate activation status. *J Neuroinflammation* **10**, 35 (2013).
154. J. E. Simpson, J. Newcombe, M. L. Cuzner, M. N. Woodroofe, Expression of monocyte chemoattractant protein-1 and other beta-chemokines by resident glia and inflammatory cells in multiple sclerosis lesions. *J Neuroimmunol* **84**, 238-249 (1998).
155. R. Chui, K. Dorovini-Zis, Regulation of CCL2 and CCL3 expression in human brain endothelial cells by cytokines and lipopolysaccharide. *J Neuroinflammation* **7**, 1 (2010).
156. C. L. Tsou *et al.*, Critical roles for CCR2 and MCP-3 in monocyte mobilization from bone marrow and recruitment to inflammatory sites. *J Clin Invest* **117**, 902-909 (2007).
157. L. Dong, H. Zheng, C. K. Qu, CCL3 is a key mediator for the leukemogenic effect of Ptpn11-activating mutations in the stem-cell microenvironment. *Blood* **130**, 1471-1474 (2017).
158. M. Pathania *et al.*, H3.3(K27M) Cooperates with Trp53 Loss and PDGFRA Gain in Mouse Embryonic Neural Progenitor Cells to Induce Invasive High-Grade Gliomas. *Cancer Cell* **32**, 684-700 e689 (2017).
159. J. D. Larson *et al.*, Histone H3.3 K27M Accelerates Spontaneous Brainstem Glioma and Drives Restricted Changes in Bivalent Gene Expression. *Cancer Cell* **35**, 140-155 e147 (2019).
160. T. Hennika *et al.*, Pre-Clinical Study of Panobinostat in Xenograft and Genetically Engineered Murine Diffuse Intrinsic Pontine Glioma Models. *PLoS One* **12**, e0169485 (2017).
161. D. Castel *et al.*, Histone H3F3A and HIST1H3B K27M mutations define two subgroups of diffuse intrinsic pontine gliomas with different prognosis and phenotypes. *Acta Neuropathol* **130**, 815-827 (2015).
162. A. D. Goldberg *et al.*, Distinct factors control histone variant H3.3 localization at specific genomic regions. *Cell* **140**, 678-691 (2010).
163. P. W. Lewis *et al.*, Inhibition of PRC2 activity by a gain-of-function H3 mutation found in pediatric glioblastoma. *Science* **340**, 857-861 (2013).
164. S. Bender *et al.*, Reduced H3K27me3 and DNA hypomethylation are major drivers of gene expression in K27M mutant pediatric high-grade gliomas. *Cancer Cell* **24**, 660-672 (2013).
165. A. Barski *et al.*, High-resolution profiling of histone methylations in the human genome. *Cell* **129**, 823-837 (2007).
166. R. Margueron, D. Reinberg, The Polycomb complex PRC2 and its mark in life. *Nature* **469**, 343-349 (2011).
167. C. M. Faria, J. T. Rutka, C. Smith, P. Kongkham, Epigenetic mechanisms regulating neural development and pediatric brain tumor formation. *J Neurosurg Pediatr* **8**, 119-132 (2011).

168. M. G. Filbin *et al.*, Developmental and oncogenic programs in H3K27M gliomas dissected by single-cell RNA-seq. *Science* **360**, 331-335 (2018).
169. F. J. Cordero *et al.*, Histone H3.3K27M Represses p16 to Accelerate Gliomagenesis in a Murine Model of DIPG. *Mol Cancer Res* **15**, 1243-1254 (2017).
170. D. Sturm *et al.*, Paediatric and adult glioblastoma: multiform (epi)genomic culprits emerge. *Nat Rev Cancer* **14**, 92-107 (2014).
171. C. M. Heaphy *et al.*, Altered telomeres in tumors with ATRX and DAXX mutations. *Science* **333**, 425 (2011).
172. X. Liu, T. A. McEachron, J. Schwartzentruber, G. Wu, Histone H3 mutations in pediatric brain tumors. *Cold Spring Harb Perspect Biol* **6**, a018689 (2014).
173. M. Vinci *et al.*, Functional diversity and cooperativity between subclonal populations of pediatric glioblastoma and diffuse intrinsic pontine glioma cells. *Nat Med* **24**, 1204-1215 (2018).
174. T. A. Juratli, N. Qin, D. P. Cahill, M. G. Filbin, Molecular pathogenesis and therapeutic implications in pediatric high-grade gliomas. *Pharmacol Ther* **182**, 70-79 (2018).
175. E. Subashi *et al.*, Tumor location, but not H3.3K27M, significantly influences the blood-brain-barrier permeability in a genetic mouse model of pediatric high-grade glioma. *J Neurooncol* **126**, 243-251 (2016).
176. C. Bethel-Brown, H. Yao, G. Hu, S. Buch, Platelet-derived growth factor (PDGF)-BB-mediated induction of monocyte chemoattractant protein 1 in human astrocytes: implications for HIV-associated neuroinflammation. *J Neuroinflammation* **9**, 262 (2012).
177. M. Poon, W. C. Hsu, V. Y. Bogdanov, M. B. Taubman, Secretion of monocyte chemotactic activity by cultured rat aortic smooth muscle cells in response to PDGF is due predominantly to the induction of JE/MCP-1. *Am J Pathol* **149**, 307-317 (1996).
178. P. Au *et al.*, Paradoxical effects of PDGF-BB overexpression in endothelial cells on engineered blood vessels in vivo. *Am J Pathol* **175**, 294-302 (2009).
179. L. van Steensel *et al.*, Platelet-derived growth factor-BB: a stimulus for cytokine production by orbital fibroblasts in Graves' ophthalmopathy. *Invest Ophthalmol Vis Sci* **51**, 1002-1007 (2010).